Investigation of collisional losses and decoherence in a 1-D optical lattice clock with ^{88}Sr

Von der Fakultät für Mathematik und Physik
der Gottfried Wilhelm Leibniz Universität Hannover
zur Erlangung des Grades eines

DOKTORS DER NATURWISSENSCHAFTEN
Dr. rer. nat.-

genehmigte Dissertation

von

M.Sc., Joseph Sundar Raaj Vellore Winfred
geboren am 23.04.1978 Chennai, Indien

2010

Referent: Prof. Dr. Wolfgang Ertmer

Korreferent: Prof. Dr. Fritz Riehle

Tag der Promotion: 11 Mai 2010

Abstract

The effects of inelastic collisions, decoherence and density dependent frequency shift in a 1-D ^{88}Sr optical lattice clock were investigated in this work. To study these effects, the ^{88}Sr atoms were first cooled down to ultra-cold temperatures and were loaded into the optical lattice operated at "magic" wavelength. The forbidden $^1S_0 \rightarrow ^3P_0$ clock transition was enabled by applying a static homogeneous magnetic field that admixes the $^3P_1$ state to the $^3P_0$ state and excited with a narrow linewidth laser. Different laser sources required for this study were setup during this thesis work. By observing the inelastic losses in a pure sample of $^3P_0$ atoms and in a mixture of $^1S_0$ and $^3P_0$ atoms, the loss-rate coefficients and the corresponding inelastic scattering lengths were determined. This study showed that the loss rate due to $^3P_0 + ^3P_0$ collisions is an order of magnitude higher compared to the loss rate due to $^1S_0 + ^3P_0$ collisions. The investigation of collisional broadening and damping of Rabi oscillations showed that a dephasing mechanism in ^{88}Sr proportional to the number of ground state atoms is present. A master equation to describe the excitation dynamics was formulated.

The frequency shift due to collisions was measured using an interleaved stabilization scheme. At low atom number, this density shift was described using mean field approach. The effect of non-linear drifts of the clock laser reference cavity on the performance of the locking to the clock transition was determined. It was shown that this effect does not limit the uncertainty of our measurement at 10^{-16} level. Based on the investigation carried on in this work, an uncertainty budget and a guideline for the design of a 1D- optical lattice clock with bosonic ^{88}Sr, which shows no degradation due to collisions at the level of 10^{-16} was developed.

Keywords: Optical lattice, elastic and inelastic collisions, frequency shift, interleaved stabilization.

Zusammenfassung

Die Auswirkungen inelastischer Stöße, Dekohärenz und dichteabhängiger Frequenzverschiebungen auf die Funktion einer optischen eindimensionalen ^{88}Sr Gitteruhr wurden in dieser Arbeit untersucht. Hierfür wurden die ^{88}Sr Atome zunächst auf ultra-kalte Temperaturen gekühlt und dann in ein optisches Gitter der "magischen" Wellenlänge geladen. Der verbotene $^1S_0 \rightarrow {}^3P_0$ Uhrenübergang wurde ermöglicht, indem ein statisches Magnetfeld zur Beimischung des $^3P_1$ Zusandes zum $^3P_0$ Zustand angelegt wurde, und mit einem schmalbandigen Laser abgefragt. Verschiedene, für diese Studien benötigte Laserquellen wurden im Rahmen dieser Arbeit aufgebaut. Durch die Beobachtung der inelastischen Verluste in einem reinen Ensemble aus Atomen im $^3P_0$ Zustand, sowie einer Mischung aus $^1S_0$ und $^3P_0$ Atomen, wurden die Verlustratenkoeffizienten und die entsprechenden inelastischen Streulängen bestimmt. Diese Messungen zeigen, dass die Verlustrate aufgrund von $^3P_0 + {}^3P_0$ Stößen eine Größenordnung über der Verlustrate aufgrund von $^1S_0 + {}^3P_0$ Stößen liegt. Die Untersuchung der Stoßverbreitung und der Dämpfung von Rabi-Oszillationen zeigte, dass für ^{88}Sr ein Dephasierungs-Mechanismus proportional zur Anzahl der Atome im Grundzustand vorliegt. Es wurde eine Gesamtgleichung aufgestellt um die Anregungsdynamik zu beschreiben.

Die Frequenzänderung durch Stöße wurde in einem verschachtelten Stabilisierungs-Schema gemessen. Die dichteabhängige Verschiebung bei geringer Atomzahl wurde durch einen *mean field*-Ansatz beschrieben. Der Effekt der nichtlinearen Drift des Uhrenlaserreferenzresonators auf die Stabilisierung auf den Uhrenübergang wurde bestimmt und es wurde gezeigt, dass diese Effekte die Genauigkeit der Messung auf einem Niveau von 10^{-16} nicht limitieren. Aufbauend auf den Messungen dieser Arbeit wurde ein Unsicherheitsbudget und ein Leitfaden für das Design einer 1-D Gitteruhr mit bosonischem ^{88}Sr aufgestellt, die keine kollisionsbedingte Herabsetzung der Genauigkeit in der Größenordnung von 10^{-16} zeigt.

Stichworte: Optisches Gitter, elastische und inealastische Stöße, Frequenzverschiebung, verschachtelten Stabilisierung.

List of Publications

T. Legero, Ch. Lisdat, J.S.R. Vellore Winfred, H. Schnatz, G. Grosche, F. Riehle and U. Sterr. Interrogation laser for a strontium lattice clock, *IEEE Transactions on Instrumentation and Measurement*, vol. 58, pages 1252-1257, 2009.

J.S.R. Vellore Winfred, C. Lisdat, T. Legero, F. Riehle and U. Sterr. Decoherence and losses by collisions in a ^{88}Sr lattice clock. Lute Maleki, editor, *Frequency Standards and Metrology, Proceedings of the* 7$^{\text{th}}$ Symposium, pages 223-227. World Scientific, 2009.

Ch. Lisdat, J.S.R. Vellore Winfred, T. Middelmann, F. Riehle, and U. Sterr, Collisional losses, decoherence, and frequency shifts in optical lattice clocks with bosons, *Phys. Rev. Lett.*, vol.103, pages 090801-090804, 2009.

Contents

List of Figures

Chapter 1

Introduction

This chapter gives a brief introduction to time standards and highlights the principle and advantages of a 1-D lattice clock based on optical transitions. The motivation for studying collisions in a ^{88}Sr 1-D lattice clock and the outline of the thesis are presented.

1.1 History of time standards

Timekeeping has played a major role in the development of human civilization. A device which is used for timekeeping is known as the <u>Clock</u>. A constant repetitive process which could characterize the passage of time and the ability to measure this process are the two fundamental requirements for timekeeping. As civilizations progressed, the need for measuring time at shorter intervals became an absolute necessity due to the fact that an activity which occurred at a time scale shorter than the time period of the timekeeping device could not be characterized. A time standard would measure a certain number of cycles and define a unit of time as the time taken to complete the number of cycles. Access to clocks by the public also lead to the need for a precise and accurate <u>Time Standard</u>. In the absence of such a standard, each individual would measure time as shown by his or her timekeeping device. This would lead to confusion and disorder since no two timekeeping devices can be synchronous for a long period of time. The need for measuring time more accurately lead to the invention of pendulum clocks and quartz clocks which is based on the piezoelectric property of quartz crystals. However, these time keeping devices suffered from imperfections. In mechanical clocks, thermal effects, drag due to presence of air and local gravity influenced their performance since the time period of the pendulum clock is proportional to the square root of its length and inversely proportional to the square root of local gravity and in quartz clocks, oscillation frequency depends critically on its size and shape and producing quartz crystals with precise dimensions posed limitation on its reliability because no two crystals can have the exact dimensions, therefore the oscillation frequency would be slightly different.

The idea of using atoms as a frequency standard was first proposed by Lord Kelvin in 1879 [3]. Early 20th century witnessed a rapid development of theory and experi-

mental investigations into the quantum nature of atoms. These investigations revealed the experimental possibility to have time or frequency standard based on the discrete energy levels of atoms. This new approach to define and determine time had an advantage, the difference between two energy levels of an atom is discrete, therefore the atoms get excited only to an incident radiation that corresponds to a particular frequency. The properties of a time standard is largely determined by the quality factor of its reference transition which is given as $Q = \nu_0/\Delta\nu$ where ν_0 is the number of cycles (repetitive process) which is used to define a unit of time known as the "second" and $\Delta\nu$ is the observed width of the reference transition. The quality factor of atom based microwave frequency standard ($\nu \sim$ GHz) is more than the quartz oscillators ($\nu \sim$ MHz) by 3 orders of magnitude and the frequency standard based on atoms are less sensitive to external perturbations compared to previous time standards.

Motivated by these advantages and the development of electronics capable of making microwave measurements lead to the first atomic clock based on an ammonia absorption line at 23870.1 MHz [4]. The demonstration of the first atomic clock and its advancement due to the pioneering works [5, 6] opened up a window of possibilities. Its impact was seen in every field of study where synchronization is important. Precision measurement of time increased the precision of scientific measurements which provided a deeper insight. Improvement in accuracy with which time could be measured lead to the redefinition of the S.I. (Systéme international) unit "meter" which is defined as [7] "The meter is the length of the path traveled by light in vacuum during a time interval of 1/299 792 458 of a second". Since the speed of light is constant, the ultimate accuracy with which length is measured could be only limited by the accuracy of the measurement of time.

Various experiments summarized in reference [8], established the superiority of atomic clocks in accuracy and stability with respect to previous time standards. This development demanded the need for a new definition of the time unit "second". "Second" got its new definition at the 13ᵗʰ General Conference for Weights and Measures (CGPM) in the year 1967. The official S.I. unit of time is defined as [9]

> "The second is the duration of 9 192 631 770 periods of the radiation corresponding to the transition between the two hyperfine levels of the ground state of the cesium 133 atom."

Factors such as natural occurrence of only one stable isotope (^{133}Cs), large hyperfine splitting (9.192 GHz), relative ease to probe and detect made Cesium an attractive element for the frequency standard when compared to other competitors like Hydrogen maser or Rubidium based frequency standards [8].

Performance of an atomic clock is determined by two factors namely the accuracy and stability. The agreement between the measured value of the transition frequency and the unperturbed transition frequency gives us the accuracy of the clock. The stability of the clock denotes the ability to constantly reproduce a frequency value. Accuracy of an experiment can be improved by making sure that the perturbations that would change the real value of the outcome of an experiment are eliminated or minimized. The limitations in the accuracy of cesium clocks, as in any other atomic clocks, comes from the fact that in order to measure the difference between two energy

2

levels of an atom as accurately as possible, the energy levels should be kept free of perturbation. In real world, such an ideal environment is not possible since there is always interaction between the system and its environment. Imperfections such as shifts the clock transition frequency due to cold collisions, quadratic Zeeman effect, black-body radiation, second-order Doppler shift, frequency shift due to imperfect electronics etc, limit the accuracy with which we can measure the atomic transition of the Cesium clock.

Stability (or instability) of a frequency standard is usually expressed in terms of Allan deviation [10]. When white frequency noise is the dominating noise contribution, the Allan deviation is given by the equation [11]:

$$\sigma_y(\tau) = \frac{\Delta\nu}{\nu_0}\frac{\eta}{S/N}\sqrt{\frac{T_c}{\tau}} \tag{1.1}$$

where $\Delta\nu$ is the line-width of the atomic transition with frequency ν_0. S/N is the signal to noise ratio of a single cycle, the cycle time T_c is the time taken to complete one interrogation, τ is the averaging time and η is a numerical factor in the order of unity and it depends on the shape of the resonance line and the method of spectroscopy used to determine the transition. From the equation, we find that the stability of an atomic clock could be improved by having a higher quality factor $\nu_0/\Delta\nu$ and improving S/N.

1.2 Atomic clocks based on optical transitions

The limitations posed by the cesium clocks motivated other ways to improve a frequency standard. Timekeeping improved over time by increasing the quality factor, so the next logical step would be to look for ways to increase the quality factor which means to look for a frequency standard with higher frequency ν_0 and lower line-width $\Delta\nu$. Optical transitions which are of hundreds of terahertz were the answer. Aided by the new technology of femtosecond-laser frequency combs [12] to count the optical frequencies, atomic clocks based on optical transitions, also known as optical clocks, will offer a quality factor which is 4 orders of magnitude more than that of a Cesium clock [13, 14].

Frequency standards based on single ions [15] attracted attention based on many advantages. First, several ions have narrow transitions in the optical frequency regime [16]. Single ions are only influenced by background collisions [17]. Since the ions are trapped, one can have long interaction time. An ion confined, such that its motion is smaller than the wavelength of the laser used to probe the clock transition (Lamb-Dicke regime [18]), is free of first-order Doppler effect. Impressive performance of ion clocks [19, 20, 21, 22, 23] has made them viable candidates for an optical frequency standard.

In spite of ion clocks showing promise due to high Q factor and increased accuracy, the stability of such clocks is limited due to the signal-to-noise ratio since only one ion is probed. The idea of improving signal-to-noise ratio by probing an ensemble of
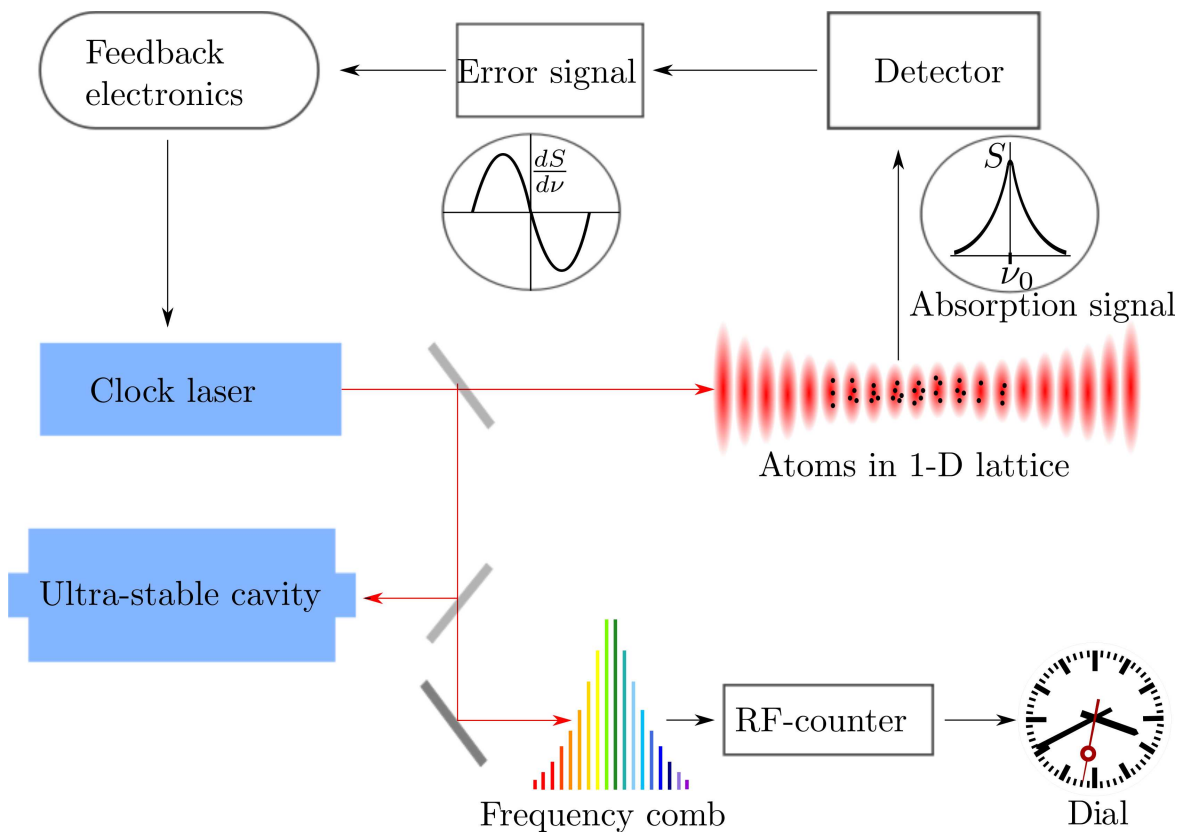
Figure 1.1: Principle of an optical lattice clock.

neutral atoms [24, 25] lead to initial demonstrations of optical clocks based on laser-cooled alkaline-earth atoms [26]. Using laser-cooled neutral atoms had two major disadvantages, the clock transition was subjected to Doppler effect and the interaction time was limited since the atoms were not confined, therefore limiting the accuracy of the clock transition measurement. Confining the atoms in the Lamb-Dicke regime, by using an optical lattice [27] at a specific "magic" wavelength where the ac Stark shift of the clock transition states are same, one can measure the clock transition free of perturbation due to trapping laser [28, 29]. This light-shift cancellation technique opened doors to explore optical lattice clocks because it offers Doppler and ac Stark shift free spectroscopy in addition to large ensemble of atoms (good S/N).

The schematic of a 1-D optical lattice clock as it was setup during this thesis work is shown in fig. 1.1. The clock-laser which is used to probe the clock transition is pre-stabilized to an ultra-stable optical cavity. The atoms trapped in the optical lattice are probed by this laser and the absorption signal is detected by the detector. The absorption signal is used to generate an error signal and this error signal is used by the feedback electronics to stabilize the laser to the clock transition. The femtosecond frequency comb is stabilized to the clock-laser, this would enable all the comb components to have the same stability and accuracy as that of the laser enabling production of stable clock signal in the microwave-frequency domain thus making it possible to measure time.

Optical clocks will find applications in areas where their improved accuracy and stability can be used to measure other physical quantities. First obvious application would be redefinition of "second". Improved definition of other fundamental units such as "meter" would be possible with the help of optical clocks. By using optical clocks, fundamental physical theories and the constancy of fundamental constants can be put to a more rigorous test [30, 31]. For example, the dependence on the fine structure constant α varies from one transition to another [32]. By comparing different clock transitions over time, one can investigate the temporal variation of α [33, 34]. Assuming a constant value for the speed of light, the accuracy with which the distance between two sites can be determined will be increased with the help of optical clocks leading to application of such clocks in GPS (Global positioning system), Lunar Ranging and space exploration resulting in improved navigation accuracy.

1.3 Motivation and outline of the thesis

The first demonstration of an optical lattice clock [35] was done on the $5s^2\ ^1S_0 \rightarrow 5s5p$ $^3P_0$ transition of ^{87}Sr with a natural linewidth of 1 mHz. Since then, various systematic experimental [36, 37, 38, 39] investigation and theoretical [40, 29, 41, 42] work has provided strong argument for optical lattice clocks. The current uncertainty of 1-D ^{87}Sr lattice clock is at the level of 1×10^{-16} [14]. Fermionic isotope based lattice clocks in principle, would be free of collisions. This is the primary motivation for exploring fermionic optical lattice clocks. In the fermionic ^{87}Sr the presence of nuclear spin ($I = 9/2$) is responsible for hyperfine interaction allowing the $^1S_0 \rightarrow ^3P_0$ transition, however, external magnetic field and lattice light polarization effects perturbs $^1S_0 \rightarrow ^3P_0$ clock transition. The hyperfine interaction also complicates the laser cooling process by requirement of additional laser [43]. Due to these reasons bosonic isotopes which have zero nuclear spin were explored.

In bosonic isotopes, the $^1S_0 \rightarrow ^3P_0$ transition can either be probed by three-photon resonances [44] or by applying a static homogeneous magnetic field [45]. Bosonic ^{88}Sr isotope have higher natural abundance, therefore one can have higher signal to noise ratio but the presence of s-wave collisions in ^{88}Sr leads to clock frequency shifts. These collisions among bosonic atoms can be suppressed if a 3-D lattice is used with one atom per site occupancy [46] but it would mean increased complexity in the experimental setup. Therefore, by understanding the collisional effects in a 1-D lattice, one can determine how it affects the accuracy of the clock transition of ^{88}Sr. A 1-D lattice clock based on ^{88}Sr can potentially offer higher stability and less complicated experimental setup compared to a 1-D ^{87}Sr clock, thus finding applications as transportable setups which could be operated in space [47]. At the time of starting this work, 1-D lattice clocks based on ^{88}Sr were not explored in depth. Shift coefficients for quadratic Zeeman effect, ac Stark shift of the probe laser and blackbody radiation were theoretically estimated for ^{88}Sr clock transition [45, 48] but experiments were not carried out to observe and measure the collisional shift. In order to compare a 1-D lattice clock based on ^{88}Sr with the best lattice clock to this date [14], collisional shift should be measured at an uncertainty level of 10^{-16}.

Studying the prospects of using bosonic ^{88}Sr atoms in a 1-D optical lattice clock for an optical frequency standard, with the focus on investigating collisions, is the aim of this thesis. The work presented in this thesis investigates collision induced effects: (a) broadening of the clock transition due to collisions, (b) losses due to inelastic collisions between, both ground-excited ($^1S_0+^3P_0$) and excited-excited ($^3P_0+^3P_0$) state atoms of the clock transition, and (c) frequency shift of the clock transition due to collisions.

The following chapter will cover the level structure relevant to the laser cooling of ^{88}Sr and explain the magnetic field induced clock transition. The advantages of a "magic" wavelength 1-D lattice confinement in the Lamb-Dicke regime and how one can extract different parameters like trap radius, atom temperature by doing spectroscopy on the clock transition will be explained.

In order to study the collisional effects, the ^{88}Sr atoms are first cooled down to ultra-cold temperatures and are loaded into the optical lattice operating at "magic" wavelength. Lasers required for two-stage cooling, repumping and optical trapping were setup during this thesis work. In chapter 3, the vacuum chamber, different light sources (461 nm, 689 nm, 679 nm, 707 nm, 813 nm) that were used for cooling, repumping and trapping will be explained. The atoms are first cooled down to few mK using $^1S_0{\rightarrow}^1P_1$ strong transition. Further cooling is made possible using the intercombination $^1S_0{\rightarrow}^3P_1$ transition. Optimization of atom number and temperature during the cooling stages and simultaneous loading into the optical lattice will be described in this chapter. The 698 nm laser used for $^1S_0{\rightarrow}^3P_0$ spectroscopy is explained and the clock transition detection scheme and our observation of sideband spectra in the Lamb-Dicke regime will be discussed in detail.

Chapters 4 and 5 will describe the investigation of collisional losses and density-dependent frequency shifts in a 1-D lattice clock based on ^{88}Sr. The inelastic losses due to collisions between atoms were investigated by observing temporal variation of atom number in the lattice for different initial atom numbers and the loss rates were determined. By varying the atoms in the lattice and observing the clock transition and Rabi oscillations, the decoherence effects and broadening of the clock transition were studied and in the process an additional dephasing due to elastic collisions was identified. Finally, by using the technique of interleaved stabilization, the clock frequency shift due to collisions was determined. The method of alternating stabilization that was used to find the density-dependent frequency shift is explained and possible sources of errors that may affect the measurements using alternating stabilization has been studied in detail. Having quantified the collision effects, operational parameters under which a 1-D optical lattice clock with ^{88}Sr can be operated without degradation due to collisions at a fractional uncertainty level of 10^{-16} and a preliminary uncertainty budget will be presented.

Chapter 6 will conclude the thesis by summarizing the findings of this work and its impact.

Chapter 2

Trapping and probing of ^{88}Sr atoms

In this chapter, the transitions available for cooling ^{88}Sr atoms down to ultra-cold temperatures is described. The advantages of spectroscopy in the Lamb-Dicke regime are explained in section 2.2. Sections 2.3 and 2.4 discusses the trapping of atoms in an optical lattice and the necessity for using "magic" wavelength. The chapter concludes by explaining in detail magnetic field induced spectroscopy which is used in this work to induce the forbidden $^1S_0 \rightarrow ^3P_0$ clock transition.

2.1   Level structure of Strontium

Strontium is an element of Group 2 of the periodic table. It has two valence electrons which couple in two ways, anti-parallel to result in spin singlet state ($S = 0$) and parallel to result in spin triplet state ($S = 1$). The ground state is $^1S_0$ with $J = 0$. The strontium level structure is shown in fig. 2.1. The transition to the first excited singlet P state ($^1P_1$) is dipole allowed transition with an excited state lifetime of 5 ns. The $^1S_0 \rightarrow ^1P_1$ strong transition allows to laser cool the atoms down to a few mK. Since the ground state is non-degenerate, sub-Doppler cooling is not possible for ^{88}Sr. Atoms in the $^1P_1$ state can decay to the lower $^1D_2$ state and could be lost from the trap by ending up in the metastable $^3P_2$ state and atoms decaying into the $^3P_1$ state would decay back to the ground state. The decay to the $^1D_2$ state is small ($3.85(1.47) \times 10^3$) [49], so a considerable number of photons can be scattered to cool the atoms using the $^1S_0 \rightarrow ^1P_1$ transition. Atoms decaying to the $^3P_2$ could be brought back to ground state by using 679 nm and 707 nm repumping lasers (see fig. 2.1) to excite the atoms in the $^3P_2$ and $^3P_0$ states to $^3S_1$ state which would then decay back to ground state via $^3P_1$.

Selection rules tell that the electric dipole operator (E1) does not allow $\Delta S = \pm 1$ transitions, therefore no dipole transition is possible between spin singlet and spin triplet states. This rule is true for atoms with low mass where the Russell-Saunders LS-coupling is valid [50]. But for heavier atoms like strontium, spin-orbit interaction results in the LS-coupling breaking down in which case a small amount of $^1P_1$ state mixes with the $^3P_1$ thus allowing the $\Delta S = \pm 1$ transition. Such weak dipole transitions are called intercombination lines and they are much weaker than the strong $\Delta S = 0$
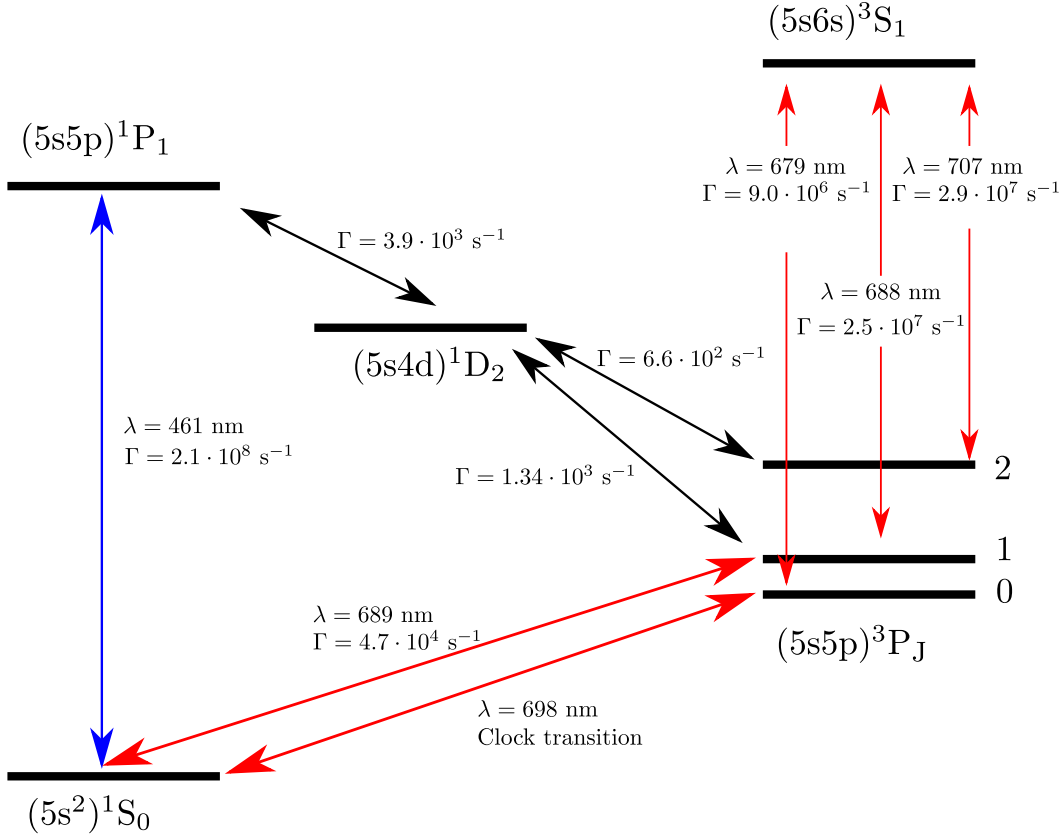
Figure 2.1: Partial strontium energy level scheme. Γ denotes the spontaneous decay rate.

transitions. The intercombination lines, due to their narrow linewidths can be used to further cool the atoms already cooled by the $^1S_0 \rightarrow {}^1P_1$ transition. In this work, the $^1S_0 \rightarrow {}^3P_1$ intercombination transition at 689 nm was used to cool the atoms down to a few μK. This second stage cooling is here called as the "red MOT".

Strontium occurs in four stable isotopes in nature, they are ^{88}Sr, ^{87}Sr, ^{86}Sr and ^{84}Sr. Their natural abundance [51] is given in Table 2.1. Table 2.1 shows among bosons, highest natural abundance is for ^{88}Sr and only one fermionic isotope is present with 7.02% natural abundance. Due to presence of only one fermionic isotope and high natural abundance for the bosonic ^{88}Sr isotope, most of the lattice clock experiments based on strontium focus on these two isotopes. The ^{88}Sr isotope has a nuclear spin $I = 0$. The ^{87}Sr isotope has a nuclear spin $I = 9/2$. The presence of the nuclear spin in ^{87}Sr results in hyperfine interaction. This hyperfine interaction mixes the $^3P_0$ state with $^3P_1$ state resulting in $^3P_0$ acquiring a weak dipole coupling with the ground state $^1S_0$. This dipole coupling would allow the $^1S_0 \rightarrow {}^3P_0$ transition in ^{87}Sr and the line-width of the transition is ~ 1 mHz making it suitable for an optical frequency standard. Table 2.2 lists the characteristic data of the atomic transitions relevant to laser cooling of strontium.

Atomic mass number	I	Natural abundance(%)
84	0	0.56
86	0	9.89
87	9/2	7.02
88	0	82.56

Table 2.1: Isotopes of Strontium.

Characteristic data	$^1S_0 \rightarrow {}^1P_1$	$^1S_0 \rightarrow {}^3P_1$
Wavelength: λ (nm)	461	689
Lifetime of upper state: τ (ns)	5.00	21322
Linewidth: $\gamma = \frac{\Gamma}{2\pi}$ (MHz)	31.83	0.00746
Saturation intensity: $I_s = \frac{\pi h c}{\lambda^3 \tau} \cdot \frac{2J_i+1}{2J_u+1}$ (mW/cm^2)	42.50	0.00298
Doppler temperature: $T_D = \frac{h}{4\pi k_B \tau}$ (μK)	764.17	0.18

Table 2.2: Characteristic data for cooling transitions used in this thesis.

2.2 Spectroscopy in Lamb-Dicke regime

Interrogation of ultra-cold atoms in free space is subjected to Doppler shift ω_D and recoil shift ω_r. The angular frequency ω_{abs} of the light absorbed by a moving atom with velocity $\mathbf{v}$ is given as [52]

$$\omega_{abs} = \omega_0 + \omega_D + \omega_r \tag{2.1}$$

where $\omega_D = \mathbf{k} \cdot \mathbf{v}$ is the first-order Doppler frequency shift with $\mathbf{k}$ being the wave vector of the incident radiation, ω_0 is the transition frequency of the atom at rest and $\omega_r = \frac{\hbar k^2}{2M}$ is the recoil frequency. While the recoil shift is constant for a given transition, Doppler shifts depend on the velocity distribution of the atoms. These shifts limit the experimental accuracy of the transition we want to probe. The way to overcome this problem is to restrict the motion of the atoms. If the atoms are confined in a harmonic potential, they would execute periodic sinusoidal motion at an oscillation frequency ω_z, the displacement of the atoms is given as $z(t) = z_{\max} \sin(\omega_z t)$ where $z_{\max}$ is the maximum displacement. When a laser tuned to the clock transition frequency ν_0 probes an atom confined in such a harmonic potential, the transition frequency as seen by the atom will be modulated by the first-order Doppler shift at trap frequency ω_z [53]. By using the classical picture of a moving atom, the radiation field experienced by the atom can be written as [54]

$$E = E_0 e^{i(\omega_0 t - k z_{\max} \sin(\omega_z t))} = E_0 e^{i\omega_0 t} \left[\sum_{m=-\infty}^{+\infty} (-1)^m J_m(k z_{\max}) e^{-i m \omega_z t} \right]. \tag{2.2}$$

9

In eq. 2.2, the amplitude of the spectral component named m is given by the Bessel function J_m and $\omega_0 = 2\pi\nu_0$. The Doppler-free component of the spectrum ($m = 0$) has an amplitude which is proportional to $J_0(2\pi z_{\max}/\lambda)^2$. The spectrum absorbed by the moving atom is discrete and it is given as

$$\nu_{\pm m} = \nu_0 \pm m\frac{\omega_z}{2\pi} = \nu_0 \left(1 \pm m\frac{v}{\eta c}\right) \tag{2.3}$$

where v is the peak velocity of the atom inside the trap and $\eta = 2\pi z_{\max}/\lambda$. In eq. 2.3 we see that if η is small, the side spectral components ($m \neq 0$) also known as sidebands, will be separated from ν_0. This would mean that the absorbed radiation of the atom confined in the harmonic potential would be same as in the case when the atom is at rest provided the atom interacts only with the central peak [53]. The parameter η is known as the Lamb-Dicke parameter.

The above classical picture gives us an intuitive understanding of absorption spectra in the Lamb-Dicke regime, however, it does not take into account photon recoil effects. In order to have a complete understanding, the atom-laser interaction and the motion of the atoms in the harmonic trap is treated quantum mechanically [52]. The population of the vibrational levels in a 1-D harmonic trap is characterized by the probability distribution $P(n)$ where n characterizes the energy levels of the harmonic oscillator with $E_n = \hbar\omega_z(n+\frac{1}{2})$. When a laser of frequency ω traveling along the z axis given by a plane wave e^{ikz} probes the atomic transition of frequency ω_0 and linewidth Γ, the strength of the absorption signal for the atoms in a 1D harmonic potential depends on the probability distribution $P(n)$ and the overlap of the wavefunction of the atoms in the initial and final motional states (Franck-Condon factor). The signal is given as [55, 56, 52]

$$S(\omega) \propto \sum_{n_f, n_i} P(n_i) \frac{|\langle n_f|e^{ikz}|n_i\rangle|^2}{1 + \frac{4}{\Gamma^2}(\omega_0 - \omega + (E_{n_f} - E_{n_i})/\hbar)^2} \tag{2.4}$$

where $|n_i\rangle$, $|n_f\rangle$ are the initial and final motional states of the atom in the harmonic potential. If $\langle kz \rangle < 1$ we can expand the matrix element of eq. 2.4 to first order as

$$\langle n_f|e^{ikz}|n_i\rangle \approx \langle n_f|1|n_i\rangle + \langle n_f|ikz|n_i\rangle = \delta_{n_f n_i} + i\frac{2\pi z_0}{\lambda}(\sqrt{n_i + 1}\delta_{n_i+1,n_f} + \sqrt{n_i}\delta_{n_i-1,n_f}) \tag{2.5}$$

where the position operator is given as $z = z_0(a^\dagger + a)$, $a^\dagger$ and a being the raising and lowering operators. $z_0 = \sqrt{\hbar/M\omega_z}$ is the characteristic oscillator length. Squaring the matrix element, we get

$$A_{n_f n_i} \equiv |\langle n_f|e^{ikz}|n_i\rangle|^2 \approx \delta_{n_f n_i} + \eta^2((n_i + 1)\delta_{n_i+1,n_f} + n_i\delta_{n_i-1,n_f}) \tag{2.6}$$

where $\eta = 2\pi z_0/\lambda$ is the Lamb-Dicke parameter. The Lamb-Dicke parameter can also be given in terms of recoil-frequency and oscillation frequency as

$$\eta = \sqrt{\frac{\omega_r}{\omega_z}}. \tag{2.7}$$

10

Eqs. 2.4 and 2.6 gives us insight into the absorption spectrum of an atom trapped in a harmonic potential in the Lamb-Dicke regime ($\eta < 1$). Consider the case of an atom with internal clock states $|g\rangle$ and $|e\rangle$ separated by frequency ω_0. The atom will absorb the incident radiation if the radiation frequency (ω) is equal to the sum of the frequency difference between the internal states (ω_0) and the frequency difference between the motional states $(E_{n_f} - E_{n_i})/\hbar$. This resonance condition ($\omega = \omega_0 + (E_{n_f} - E_{n_i})/\hbar$) is given in the denominator of eq. 2.4. The three cases in which absorption will occur are given in eq. 2.6. The cases are discussed below

- The first term will be non-zero and the last two terms will be zero when the change in motional quantum number is zero ($n_i = n_f$). When the atom is trapped in the "magic" wavelength, the vibrational frequencies of ground and excited states are same. In this case, the atom will change its state to $|n_i\rangle$ from $|n_f\rangle$ when $\omega = \omega_0$. The transition frequency ω_0 in this case is also known as the carrier frequency.

- δ_{n_i+1,n_f} is non-zero when $n_f - n_i = 1$, in this case, the atoms will absorb radiation when $\omega = \omega_0 + \omega_z$. Since this sideband frequency is higher than the carrier frequency, it is called the blue-sideband.

- δ_{n_i-1,n_f} is non-zero when the motional quantum number changes by -1. The atoms will absorb radiation when $\omega = \omega_0 - \omega_z$. This sideband frequency is lower than the carrier frequency and therefore is called the red-sideband. The red-sideband feature will be absent if all the atoms are in the motional ground state $n_i = 0$.

The matrix element in eq. 2.4 for general values of k and z_0 is [52]

$$\langle n_f | e^{ikz} | n_i \rangle = e^{-\frac{1}{2}(kz_0)^2} \sqrt{\frac{n_<!}{(n_< + \Delta n)!}} (ikz_0)^{\Delta n} L_{n_<}^{\Delta n}[(kz_0)^2] \qquad (2.8)$$

where $n_<$ is the lower value of the initial and final motional quantum number, $\Delta n = |n_f - n_i|$ (difference between the motional quantum numbers) and $L_{n_<}^{\Delta n}[(kz_0)^2]$ is the generalized Laguerre polynomial. From eq. 2.6 we see that in the Lamb-Dicke regime, the absorption signal of the carrier transition is not affected by the initial and final motional states but the sideband signals depend on the initial motional state. Also the position of the sidebands and the carrier does not depend on the initial motional state. However, if the trapping potential experienced by the ground and excited states is not same then the motional energy levels of the ground and excited states for the same motional quantum number will not be equal ($E_{n_f} - E_{n_i} \neq 0$ for $n_f = n_i$), the carrier transition in this case will depend on the motional states. Therefore, it is important to trap the atoms at a wavelength in which the ground and the excited states experience the same potential so that the carrier transition is not affected by the trap. Section 2.4 explains how to calculate the this "magic"wavelength. Since the recoil frequency ω_r for a given transition is constant, eq. 2.7 shows that the Lamb-Dicke criterion ($\eta < 1$) improves if the atom is more more tightly bound to the lattice

potential. Therefore, when the atom is in the Lamb-Dicke regime ($\eta \ll 1$), the photon recoil momentum is taken by the system consisting of atom and confining potential [52, 18].

So far, we assumed that the atom is trapped in a harmonic potential which depends on position z as z^2. However, the trap potential which is used to confine the atoms depends on position as $\cos^2(kz)$, this difference results in trap anharmonicity. Trap anharmonicity leads to modification of the energy of the motional states of the trap [57, 58, 55] and its effect becomes noticeable for higher motional states, but as long as atoms are trapped at magic wavelength, the change in the ground and excited trapping potentials will be same and the net effect of the trap anharmonicity on the carrier transition will be zero. Since the energy difference between the motional trap states depends on the depth of the potential due to anharmonicity, the sideband frequency will therefore depend on the motional state of the atom.

To see the effect of radial motion, we note that due to the Gaussian profile of the trapping beam, the atoms are less confined in the radial direction. As the atoms move along the radial direction, the intensity and therefore the axial trap frequency change depending on the position of the atom along the radial direction. The change in axial trap frequency does not influence the carrier transition when the atoms are trapped in the magic wavelength but the sideband frequency position depends on the variation of intensity along the radial direction. This leads to asymmetric broadening of the sidebands. Since the radial temperature determines the extent to which atoms can move in the harmonic potential, the sideband signal and the degree of asymmetry depend on the radial temperature of the atoms and trap parameters (intensity, waist radius and wavelength) [55].

In addition to axial sideband frequencies present due to axial motion, radial motion results in radial sidebands. These radial sidebands which can be calculated from eq. 2.16 are present in our case at 390 Hz from the carrier transition which is much closer than the axial sideband frequencies. However, they can be suppressed when the probe beam is aligned orthogonal to the radial motion of the atoms. Detailed investigation of the effects of atom temperature, trap parameters, axial and radial motion on the Rabi frequency for the carrier transition is given in reference [55]. The study suggests that in order to have a uniform Rabi oscillation, the confinement of the atoms along the radial direction must be strong and all the atoms must occupy the lowest axial motional state.

The situations considered till now treated each potential well separately, this assumption is strictly true for deep potential wells where one can neglect tunneling of atoms from one well to another. Before ending this session we note that the finite periodic $\cos^2(kz)$ potential, as in the case of optical lattice will have a band structure with finite energy bandwidths for the quantum states since each potential well cannot be treated separately. The band structure and the finite bandwidth causes shift in the clock transition frequency and line broadening. These effects can be viewed as residual Doppler and recoil effects due to quantum tunneling and they do not affect the clock frequency at a fractional inaccuracy level of 10^{-17} if the potential depth is more than $U_{\max} = 70E_r$ where E_r is the recoil energy due to lattice photon [59]. For an optical lattice aligned vertically, gravity causes adjacent sites to be shifted in energy. This re-

sults in lifting the degeneracy between adjacent sites, therefore suppressing site-to-site tunneling. For vertically aligned lattices, a potential depth of $U_{\max} = 5E_r$ can be used for the same fractional inaccuracy level [59].

2.3 Confinement of atoms in 1-D optical lattice

The confinement of neutral atoms can be achieved by using optical dipole traps [60]. The basic equations for the dipole potential are derived by considering the atom as a simple oscillator which is subjected to a classical radiation field. A laser beam with electric field $\mathbf{E}(t)$ and angular frequency ω interacting with an atom would induce a dipole moment $\mathbf{d}$ in the atom. The oscillation frequency of dipole moment is same as that of the electric field and the relation between the induced dipole moment and the electric field is given as

$$\mathbf{d} = \alpha(\omega)\mathbf{E} \tag{2.9}$$

where $\alpha(\omega)$ is known as the complex polarizability. It describes how easily the electric field induces the dipole moment as a function of the frequency. The potential energy of the induced dipole is [60]

$$U_{\mathrm{dip}} = -\frac{1}{2\epsilon_0 c}\mathrm{Re}(\alpha)I \tag{2.10}$$

where $I = \epsilon_0 c |E_0|^2$ is the intensity for a given field amplitude E_0. The corresponding force $\mathbf{F}_{\mathrm{dip}}$ is given by the potential gradient $-\nabla U_{\mathrm{dip}}(\mathbf{r}) \propto \nabla I(\mathbf{r})$. Thus the dipole force is proportional to the gradient of the intensity. The imaginary part of the complex polarizability $\mathrm{Im}(\alpha)$ characterizes the power absorbed by the atom P_{abs}, this power is re-emitted as dipole radiation. The scattering rate of the photons re-emitted as dipole radiation is

$$\Gamma_{\mathrm{sc}}(\mathbf{r}) = \frac{P_{\mathrm{abs}}}{\hbar\omega} = \frac{1}{\hbar\epsilon_0 c}\mathrm{Im}(\alpha)I(\mathbf{r}). \tag{2.11}$$

In a semiclassical approach where the atom is treated as a two level system, the dipole potential and the scattering rate are given as [60]

$$U_{\mathrm{dip}} = -\frac{3\pi c^2}{2\omega_0^3}\left(\frac{\Gamma}{\omega_0 - \omega} + \frac{\Gamma}{\omega_0 + \omega}\right)I(\mathbf{r}) \tag{2.12}$$

$$\Gamma_{\mathrm{sc}} = \frac{3\pi c^2}{2\hbar\omega_0^3}\left(\frac{\omega}{\omega_0}\right)^3\left(\frac{\Gamma}{\omega_0 - \omega} + \frac{\Gamma}{\omega_0 + \omega}\right)^2 I(\mathbf{r}) \tag{2.13}$$

where Γ is the dipole-transition natural linewidth and ω_0 is the dipole-transition angular frequency. Eqs. 2.12 and 2.13 give us insight into the forces that an atom experiences in a dipole potential. When $\Delta = \omega - \omega_0 < 0$ (red-detuning), the dipole potential is negative, therefore the potential minima are found at positions with maximum intensity and when $\Delta = \omega - \omega_0 > 0$ (blue-detuning), the potential minima are found at positions with minimum intensity. Depending on the sign of Δ, a trap can be labeled either as a red-detuned trap or a blue-detuned trap.

The simplest way to create an optical dipole trap is to use a focused Gaussian beam with frequency tuned away from the atomic resonance frequency to keep the

scattering rate Γ_{sc} low. The intensity profile of a Gaussian laser beam traveling in the z axis is given as

$$I(r, z) = \frac{2P}{\pi w^2(z)} e^{\frac{-2r^2}{w(z)^2}} \tag{2.14}$$

where $w(z)$ is the $1/e^2$ radius of the Gaussian beam and r is the radial distance from the beam center. The axial profile of the Gaussian beam is given as $w(z) = w_0(1 + (z/z_R)^2)^{1/2}$ with $z_R = \pi w_0^2/\lambda$ being the Rayleigh range, λ is the wavelength of the trapping beam and P is the total laser power. The peak intensity of the beam is given as $I_0 = 2P/\pi w_0^2$. The potential depth is increased by a factor of four if the beam is retroreflected, forming an optical lattice with a period $\lambda/2$. The lattice potential is then given by the expression [61]

$$U_{\mathrm{lat}}(r, z) = 4U_{\mathrm{max}} e^{\frac{-2r^2}{w(z)^2}} \cos^2(2\pi z/\lambda) \tag{2.15}$$

where $U_{\mathrm{max}}(z) = P\alpha/(\pi c \epsilon_0 w(z)^2)$. At the center of the intensity distribution ($r \approx 0$) and the point of maximum intensity ($z \approx 0$), the axial (ν_z) and radial (ν_r) frequencies can be obtained by approximating the potential to a harmonic trap. They are

$$
\begin{aligned}
\nu_z &= \frac{1}{2\pi}\sqrt{\frac{1}{M}\left(\frac{\delta^2 U(r,z)}{\delta z^2}\right)_{r,z=0}} = \frac{1}{2\pi w_0 \lambda}\sqrt{\frac{32\pi \alpha P}{c\epsilon_0 M}} \\
\nu_r &= \frac{1}{2\pi}\sqrt{\frac{1}{M}\left(\frac{\delta^2 U(r,z)}{\delta r^2}\right)_{r,z=0}} = \frac{1}{2\pi w_0^2}\sqrt{\frac{16\alpha P}{c\pi\epsilon_0 M}}.
\end{aligned}
\tag{2.16}
$$
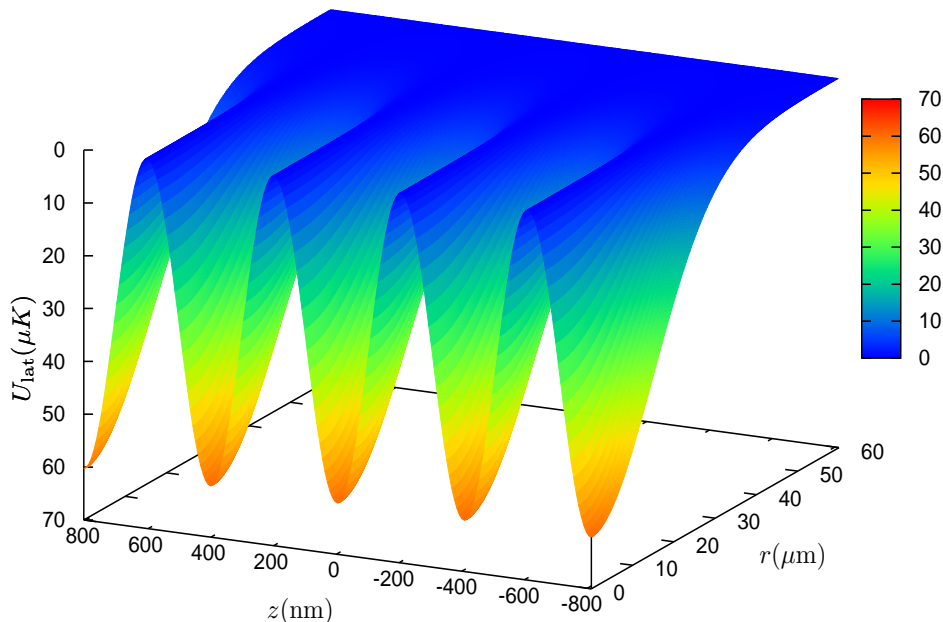
Figure 2.2: An optical lattice simulated by using eq. 2.15. The period of the lattice is $\lambda/2$, where λ is the wavelength of the trapping laser light.

This section is focused on how neutral atoms can be trapped in a 1-D optical lattice. The lattice wavelength used in our experiment is $\lambda = 813$ nm (red-detuned lattice) for reasons explained in the next section. The calculated potential of an optical lattice with a waist radius of 30 μm, 300 mW of power at a wavelength of 813 nm is shown in fig. 2.2. Eqs. 2.15 and 2.16 give the essential parameters needed to characterize an optical lattice. Atoms trapped in the red-detuned lattice will accumulate at the points of highest intensity. In the potential wells near the center of the trap $z \approx r \approx 0$, the region can be treated like a harmonic oscillator potential and therefore in the Lamb-Dicke regime, recoil-free and Doppler-free spectroscopy on the clock transition can be performed. However, the energy states of the atoms trapped in such a lattice in general will be shifted differently by the ac Stark effect. For a potential well with the above parameters, the shifts are in order of few Hz/nm. How this shift would influence the clock transition and the way to circumvent this problem is discussed in the next section.

2.4   The ac Stark shift free optical lattice

When an atom interacts with a laser, each of its atomic energy level i is shifted by the dipole potential. For an atom with unperturbed clock transition frequency ν_0 trapped in an optical lattice with electric field amplitude E_0, the perturbed (shifted) energy is given as [29]

$$h\nu = h\nu_0 - \frac{1}{4}\Delta\alpha(\hat{\mathbf{e}}, \omega)E^2 - \frac{1}{64}\Delta\gamma(\hat{\mathbf{e}}, \omega)E^4 - \dots \qquad (2.17)$$

where $\hat{\mathbf{e}}$ is the unit polarization vector of the electric field, $\Delta\alpha(\hat{\mathbf{e}}, \omega)$ and $\Delta\gamma(\hat{\mathbf{e}}, \omega)$ are the differences between ac polarizabilities and hyperpolarizabilities of the clock states. The second term in eq. 2.17 is proportional to laser intensity I. The dependence of $\Delta\alpha$ on ω offers the possibility to find a frequency of the lattice laser such that the ac polarizability of the clock states are same. These shifts in energy levels for the clock states would be equal and we can do perturbation free spectroscopy. Since the clock transition is using $J = 0$ states ($^1S_0 \to ^3P_0$), there is no dependence on electric field orientation with respect to quantization axis, resulting in a scalar light shift [28]. The effect of the second term in eq. 2.17 leading to hyperpolarizability effect will be discussed later in the thesis.

The ac polarizability of an atomic state i depends on its interaction with excited states. In second-order perturbation, it is given as the sum of the dipole interactions between state i and excited state k [62]

$$\alpha_i(\omega) = \frac{2}{\hbar}\sum_k \frac{\omega_{ik}}{(\omega_{ik}^2 - \omega^2)}|\langle\phi_k|\mathbf{d}|\phi_i\rangle|^2. \qquad (2.18)$$

The dipole matrix elements $d_{ik} = \langle\phi_k|\mathbf{d}|\phi_i\rangle$ for both clock states are required to cal-

15

culate the polarizability. The matrix elements d_{ik} are given as [63]

$$|d_{ik}|^2 = (2J_i + 1)(2L_k + 1)(2J_k + 1) \left\{ \begin{array}{ccc} L_i & J_i & S_i \\ J_k & L_k & 1 \end{array} \right\}^2 \left(\begin{array}{ccc} J_i & 1 & J_k \\ -m_i & p & m_k \end{array} \right)^2 ||d_{L_i L_k}||^2$$

(2.19)

where the curly brackets represent the $6-j$ symbol and Wigner $3-j$ symbol is the term in round brackets. $||d_{L_i L_k}||$ is the reduced dipole moment between the states $|L_i\rangle$ and $|L_k\rangle$. The dipole-transition spontaneous decay rate is related to d_{ik} as

$$\Gamma_{ik} = \frac{\omega_{ik}^3}{3\pi\epsilon_0 \hbar c^3} |d_{ik}|^2.$$

(2.20)

By knowing ω_{ik} the frequency ω at which the ac polarizability is the same for both clock states can be determined. The value at which the two polarizabilities are equal is called the "magic wavelength". The magic wavelength λ_L for the Sr $^1S_0 \rightarrow ^3P_0$ clock transition is ≈ 813 nm [29]. A deviation from the magic wavelength would result in a clock transition frequency shift of 8(2) (Hz/nm)/E_R [55], where E_R is the recoil energy associated with the absorption or emission of a photon from the optical lattice.

2.5 Forbidden $^1S_0 \rightarrow ^3P_0$ clock transition in ^{88}Sr

The $\Delta S = 1$ and $J = 0 \rightarrow 0$ nature of $^1S_0 \rightarrow ^3P_0$ clock transition in bosonic ^{88}Sr makes it doubly forbidden. Ideas using two photon electromagnetically induced transparency (EIT) [64] and three photon EIT [44] were proposed to probe the $^1S_0 \rightarrow ^3P_0$ transition. These techniques however require extra laser sources which add to the complexity of the experimental setup. A simple method to excite the clock transition was proposed by Taichenachev et al. [45]. In this method, a weak static homogeneous magnetic field is used to mix the $^3P_1$ state to the $^3P_0$ state, therefore allowing single-photon excitation of the $^1S_0 \rightarrow ^3P_0$ clock transition. This magnetically induced spectroscopy (MIS) method is simple and could be implemented without any major modification or addition to the existing experimental setup that is used to cool and trap ^{88}Sr. Since we use the static field method to excite the clock transition, in the following this method is described in more detail [1, 45].

2.5.1 Magnetic field induced transition

When an atom is placed in a static homogeneous magnetic field, its total Hamiltonian is $H_{\text{tot}} = H_0 + H_{\text{per}}$ where H_0 is the unperturbed Hamiltonian of the atom and $H_{\text{per}} = \boldsymbol{\mu} \cdot \mathbf{B}$ is the perturbation due to the static magnetic field. The total magnetic moment is $\boldsymbol{\mu} = \mu_B(g_L \mathbf{L} + g_S \mathbf{S})$ where $g_L = 1, g_S \approx 2$ and μ_B is the Bohr magneton. If one chooses the $\mathbf{B}$ field to be in the z direction, then $H_{\text{per}} \approx \mu_B(L_z + 2S_z)|B|$. The first order correction to the $|^3P_0\rangle$ state is

$$|^3P_0'\rangle = |^3P_0\rangle + \sum_\psi \frac{\langle\psi|H_{\text{per}}|^3P_0\rangle}{\hbar\Delta_\psi} |\psi\rangle$$

(2.21)

16
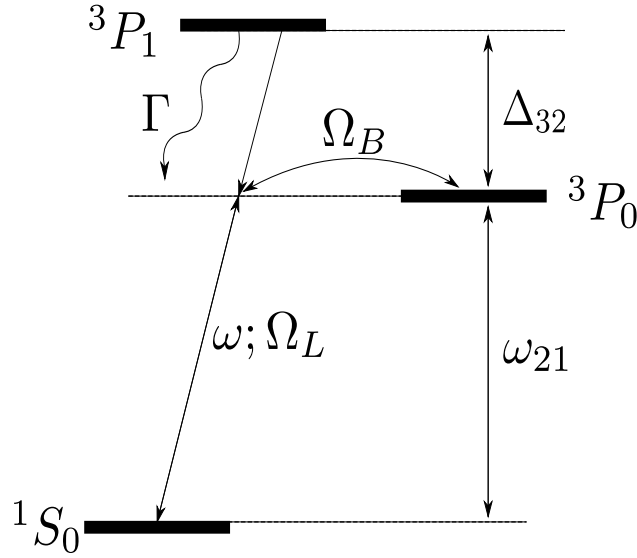
Figure 2.3: Schematic of the magnetic field induced spectroscopy of the $^1S_0 \rightarrow ^3P_0$ clock transition [1].

where the summation is performed all over possible states and Δ_ψ is the frequency difference between states $|\psi\rangle$ and $^3P_0$ state ($\Delta_\psi = \omega_\psi - \omega_{^3P_0}$). The state $|^3P_1, m_j = 0\rangle$ contributes more than 90% to the sum in eq. 2.21. By decomposing the Russell-Saunders states into eigenstates of $|L_z, S_z\rangle$, one gets [1]

$$|^3P_1, m_j = 0\rangle = \sqrt{1/2}|1, -1\rangle - \sqrt{1/2}|-1, 1\rangle \tag{2.22}$$

$$|^3P_0, m_j = 0\rangle = \sqrt{1/3}|1, -1\rangle - \sqrt{1/3}|0, 0\rangle + \sqrt{1/3}|-1, 1\rangle. \tag{2.23}$$

The above equations lead to

$$\langle ^3P_1|\boldsymbol{\mu} \cdot \mathbf{B}|^3P_0\rangle = \hbar\Omega_B \approx \sqrt{\frac{2}{3}}\mu_B|B|. \tag{2.24}$$

Therefore the first order perturbed $|^3P_0\rangle$ state in the presence of a static magnetic field is given as

$$|^3P_0'\rangle = |^3P_0\rangle + \frac{\Omega_B}{\Delta_{32}}|^3P_1, m_j = 0\rangle \tag{2.25}$$

where Δ_{32} is the fine structure splitting between $|^3P_1\rangle$ state and $|^3P_0\rangle$ state as shown in fig. 2.3. If the Rabi frequency of the intercombination transition $^1S_0 \leftrightarrow ^3P_1$ is given by Ω_L, then the Rabi frequency of the $^1S_0 \leftrightarrow ^3P_0'$ transition is

$$\Omega = \frac{\langle ^1S_0|\mathbf{d} \cdot \mathbf{E}|^3P_0'\rangle}{\hbar} = \frac{\Omega_B}{\Delta_{32}}\frac{\langle ^1S_0|\mathbf{d} \cdot \mathbf{E}|^3P_1\rangle}{\hbar} = \frac{\Omega_L\Omega_B}{\Delta_{32}} \tag{2.26}$$

where the dipole matrix operator is given by $\mathbf{d} \cdot \mathbf{E}$. Due to mixture of states $^3P_1$ and $^3P_0$, the perturbed $^3P_0'$ state has a finite natural linewidth given as [45]

$$\gamma' = \gamma\frac{\Omega_B^2}{\Delta_{32}^2} \tag{2.27}$$

17

where γ is the natural linewidth of the $^1S_0 \leftrightarrow ^3P_1$ transition. In the presence of the magnetic field, the excited state experiences a second order Zeeman shift Δ_B which is

$$\Delta_B = \frac{\Omega_B^2}{\Delta_{32}}. \tag{2.28}$$

The interaction of the laser field with the $^1S_0 \leftrightarrow ^3P_0$ clock transition will also result in optical Stark shift, this shift is given as [45]

$$\Delta_L = -\frac{\Omega_L^2}{4\Delta_{32}}. \tag{2.29}$$

Using eq. 2.28 and eq. 2.29, we can express the Rabi frequency of the clock transition as $\Omega = 2\sqrt{|\Delta_L \Delta_B|}$.

In order to express the Rabi frequency of the clock transition in terms of experimentally measurable parameters, eq. 2.26 is written in a different form by considering the vector nature of the applied fields as

$$\Omega = \frac{\langle \|d\| \rangle \langle \|\mu\| \rangle (\mathbf{E} \cdot \mathbf{B})}{\hbar^2 \Delta_{32}} \tag{2.30}$$

where $\langle \|d\| \rangle$ is the reduced matrix element of the electric dipole moment of the $^1S_0 \leftrightarrow ^3P_1$ transition and $\langle \|\mu\| \rangle$ is the reduced matrix element of the magnetic dipole moment of the $^3P_1 \leftrightarrow ^3P_0$ transition. By combining the electric and magnetic dipole matrix elements into one constant α, one can rewrite eq. 2.30 as

$$\Omega = \alpha \sqrt{I} |B| \cos\theta \tag{2.31}$$

where θ is the angle between the $\mathbf{B}$ and $\mathbf{E}$ and I is the light intensity. The second order Zeeman shift and the optical Stark shift can also be written as $\Delta_B = \beta |B|^2$ and $\Delta_L = \kappa I$. This parameterization results in rewriting the Rabi frequency equation as

$$\Omega = \xi \sqrt{|\Delta_B \Delta_L|} \cos\theta \tag{2.32}$$

where $\xi \equiv \alpha/\sqrt{\beta\kappa}$ is a dimensionless quality factor for the clock transition because it relates the Rabi frequency induced by the MIS to the corresponding induced field shifts. Table 2.3 [45] shows the MIS scheme parameters for the ^{88}Sr $^1S_0 \leftrightarrow ^3P_0$ clock transition.

γ [kHz]	Δ_{32} [THz]	α [Hz/(T$\sqrt{\mathrm{mW/cm}^2}$)]	β [MHz/T^2]	κ [mHz/(mW/cm^2)]	ξ
7	5.6	198	-23.3	-18	0.30

Table 2.3: Relevant parameters for the $^1S_0 \leftrightarrow ^3P_0$ MIS scheme of ^{88}Sr

This chapter started by covering energy level structure of strontium relevant to this thesis and listed main characteristics of the transitions used in the experiment.

Confining the atoms in a 1-D optical lattice leading to recoil-free and Doppler-free spectroscopy in the Lamb-Dicke regime and eliminating the ac Stark shift using "magic" wavelength was explained. The chapter has come to a conclusion with the theory of magnetic field induced transition. The next chapter deals with the experimental setup and describes cooling of ^{88}Sr atoms down to ultra-cold temperatures, loading them into an optical lattice and doing spectroscopy in the clock transition.

Chapter 3

Laser cooling and clock spectroscopy of ^{88}Sr

In this chapter, the experimental setup including the different laser sources and the spectroscopy on the clock transition are presented. Section 3.1 describes our vacuum setup and the coils which are used for quadrupole and Helmholtz field configurations. The 461 nm laser setup and the laser cooling of ^{88}Sr atoms down to a few millikelvin are discussed in section 3.2 along with a subsection on repumping lasers setup. Further cooling of the atoms down to few microkelvin temperatures, characterization of atom number and temperature with respect to cooling beam intensities and the 689 nm laser system is described in section 3.3. Sections 3.4 and 3.5 describe our lattice laser setup and trap radius determination using axial sloshing of the atoms. The 689 nm laser which is used for spectroscopy on the clock transition is discussed in section 3.6. The chapter concludes with section 3.7 in which schemes for detecting the clock transition, the observation of clock transition along with the sidebands and initial measurements hinting strong collisional losses and broadening are explained.

3.1   The vacuum chamber

Heart of the experiment, the vacuum chamber, is a spherical chamber made of V2A stainless steel. It has 33 view ports, five viewports with 101.6 mm O.D[1] (DN 90), one view-port with 152.4 mm O.D (DN 100), two viewports with 19.0 mm O.D (DN 10) and the rest of the view ports have 41.3 mm O.D (DN 32). The present experimental setup uses the large viewports for cooling and trapping of the atoms and the smaller ones are used for CCD-camera, fluorescence signal detection, repumping lasers and Zeeman slowing. A 400 l/s ion getter pump maintains a pressure of 5×10^{-10} mbar in the chamber.

Fig. 3.1 shows the schematic diagram of the top view of the chamber, the alignment of blue, red MOT beams and other beams of importance to the experiment. The source for the strontium atoms is an oven filled with strontium granules. The oven is a 35 mm long stainless steel cylinder and has an inner diameter of 4 mm. The oven has few tens

---

[1]O.D = Outer diameter
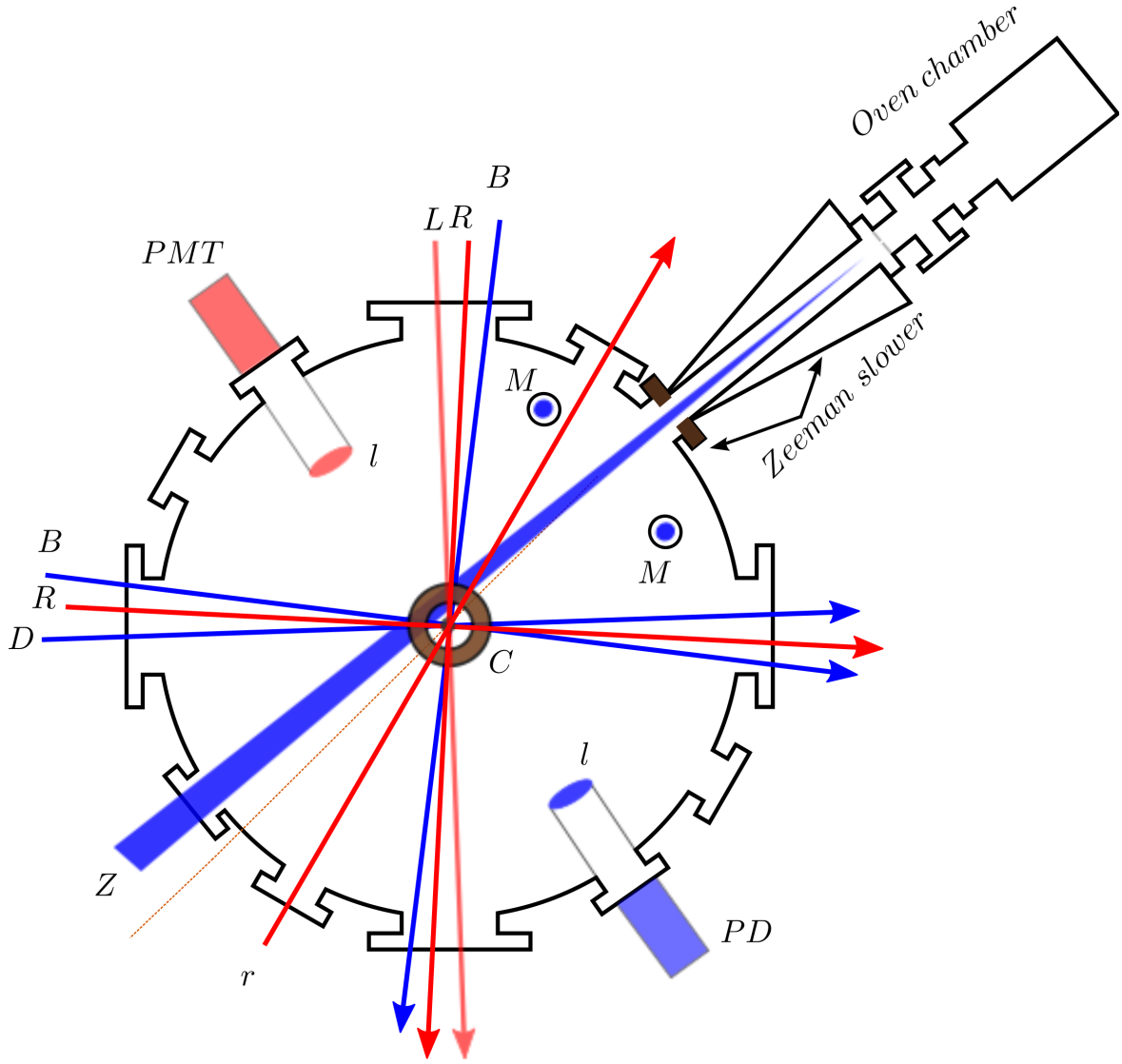
Figure 3.1: Top view of the experiment chamber. The blue MOT beams are collectively labeled as B and the red MOT beams as R. D: Detection beam for absorption imaging, Z: Zeeman slower beam, M: 2-D molasses beams, r: Repump beam, L: Lattice beam, C: Quadrupole/Helmholtz coils, PMT: Photomultiplier tube for 689 nm fluorescence detection, PD: Photodiode with amplifier for 461 nm fluorescence detection and l: Lens ($f = 80$ mm) used to collimate the atomic fluorescence. Dotted line shows the deflection of the atoms coming out of the Zeeman slower to the MOT center.

21

of capillaries (diameter $\sim$ 0.5 mm) to have good atomic flux and highly collimated atomic beam. The oven is placed inside another cylinder made of ceramic. This ceramic cylinder is surrounded by heating wire which heats the oven to a temperature of 480°C during the experiment. The oven is kept in a vacuum chamber at a pressure of $< 10^{-7}$ mbar. The oven chamber separated from the main chamber by a valve and a pinhole acting as a differential pumping stage. This separation prevents breaking of the vacuum in the main chamber every time the oven needs to be refilled. A mechanical lever-like stop is used to manually allow or block the strontium atoms coming out of the oven.

The atoms coming out of the oven are decelerated using a Zeeman slower [65] operated on the $^1S_0 \rightarrow ^1P_1$ transition. The Zeeman slower is 38 cm long. A 4 A current through the Zeeman coil produces a maximum magnetic field B_{max} = 41 mT. An additional coil with 10 A current flowing is used along with the Zeeman slower at the end to reverse the magnetic field and have the field return to zero. Atoms from the oven are decelerated to a velocity of 50 m/s from their initial average velocity of 500 m/s. Both coils of the Zeeman slower are water cooled. Atoms decelerated in the Zeeman slower are collimated and deflected by an angle of 15° by two retro-reflected independent laser beams thus forming 2-D optical molasses [66]. The deflection of the slowed atoms by 15° prevents the cooled atoms from being exposed to atoms that were not slowed in the Zeeman slower and also from black body radiation from the oven.
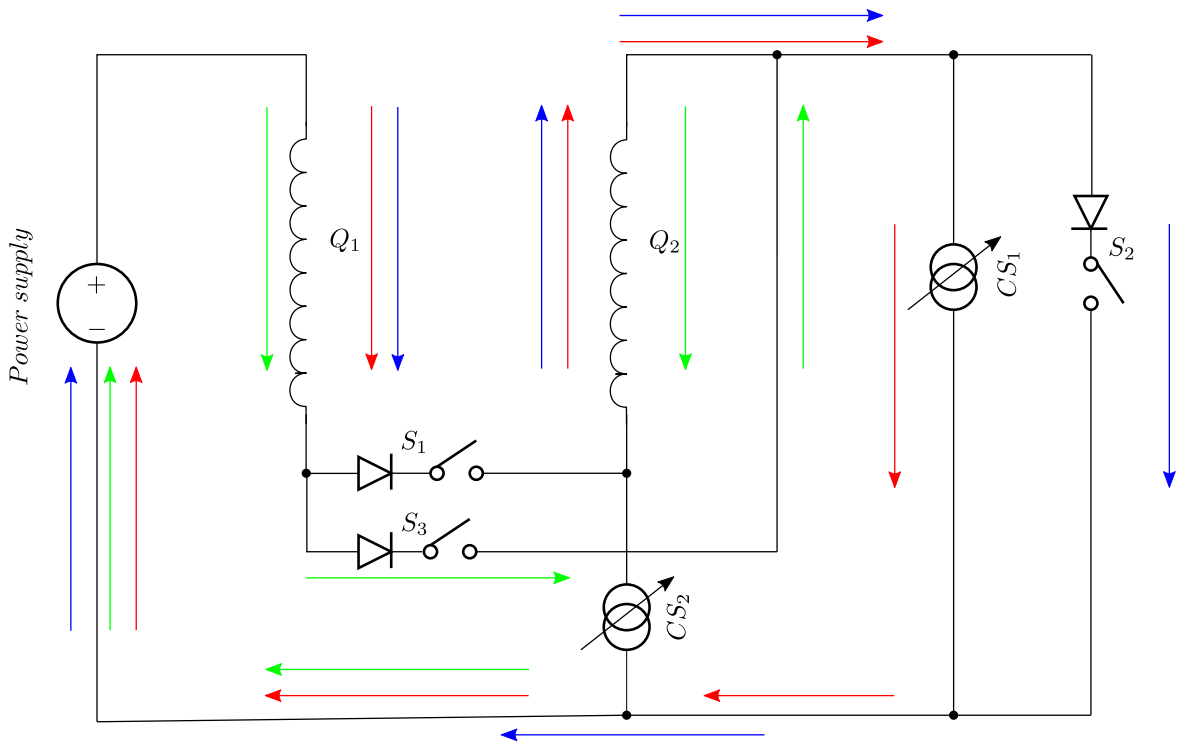
Figure 3.2: Circuit schematic of quadrupole/Helmholtz coils. The blue, red and green arrows show the current flow for the blue MOT quadrupole field, red MOT quadrupole field and Helmholtz field. The switches (S) and switchable current-sinks (CS) are controlled by TTL.

The pair of coils used for a creating magnetic field is located inside the vacuum chamber. The coils consists of 49 windings (7 radial and 7 axial) each, they are water cooled and Kapton coated. The coils are used to create Helmholtz field and quadrupole field for blue and red MOT. The coil configuration is shown in fig. 3.2. In fig. 3.2 the coils are named Q_1 and Q_2. When switches S_1 and S_2 are on, the current flow in both coils is in opposite direction, creating a quadrupole field. When S_1 is on and S_2 is off, the current passes through the current-sink CS_1 which is used to reduce the current flow in the quadrupole coil configuration for the red MOT. The current flow in both coils along the same direction (Helmholtz configuration) is enabled when S_1 and CS_1 are off and S_3 on. The current-sink CS_2 is used to regulate the flow of current in the Helmholtz configuration.

The stray magnetic field is compensated by three independent pairs of coils which are fixed on the outside of the large view port flanges of the chamber, where each pair of coil gives a constant field of ~ 0.6 μT/A. Atom fluorescence from the 461 nm transition is collimated using a $f = 80$ mm lens and is focused by a $f = 150$ mm lens on to a photodiode. A 461 nm interference filter is used to block ambient light and light from other lasers from the photodiode. A similar lens setup is used with a photo-multiplier tube and a 689 nm interference filter to detect the atom's fluorescence from the 689 nm transition.

3.2 Experimental realization of 461 nm blue MOT

The laser source for the 461 nm $^1S_0 \rightarrow {}^1P_1$ transition is shown in fig. 3.3.

Figure 3.3: Schematic of the blue MOT laser setup. *L*: Lens, *PBS*: Polarizing beam splitter, *AOM*: Acousto optic modulator and *BD*: Beam dump.

During the initial stages of the experiment, the source for the 461 nm radiation was from 922 nm Ti-Sapphire laser, frequency doubled with a periodically-poled potassium titanyl phosphate (PPKTP) crystal. Since the power output from the crystal decreased over time due to photorefractive damage resulting from blue absorption [67], the blue light source was later replaced by a commercial Toptica TA SHG 110 MOPA system. An output power of about 115 mW at 461 nm is used for the experiment. The blue MOT beams are formed by three independent beams which are retro-reflected. The beams have a $1/e^2$ diameter of 1 cm and the total beam (6 beams) intensity is 26 mW/cm^2. The 2-D molasses beams consists of two independent beams which are retro-reflected. The diameters of the 2-D molasses beams are same as that of the blue MOT beams and have a total beam power (4 beams) of 9 mW. The power of the Zeeman slower beam is 20 mW. The blue laser source is frequency stabilized to a ^{88}Sr reference atomic beam.
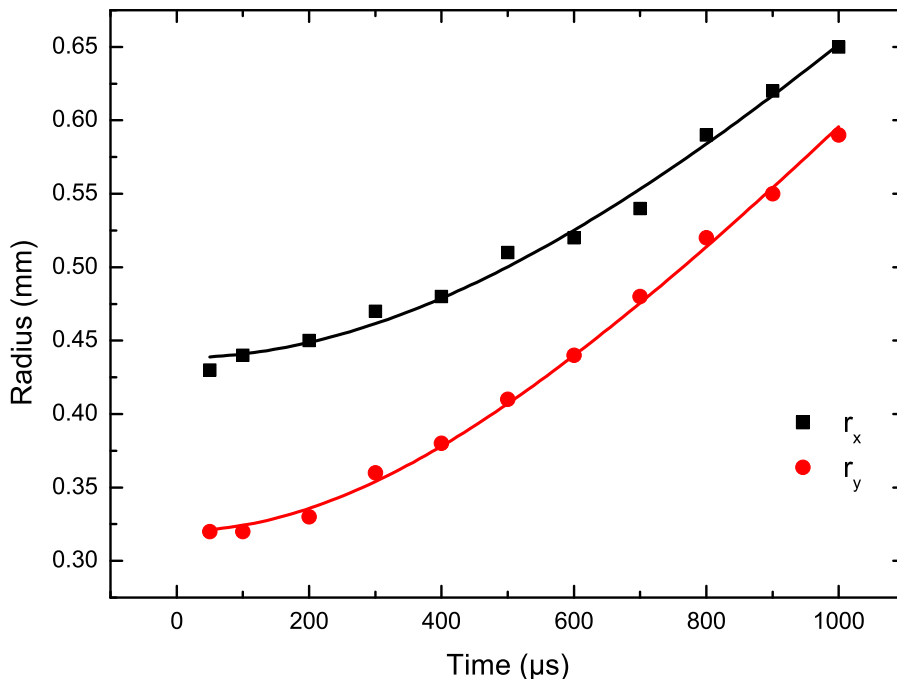
Figure 3.4: Expansion of blue MOT at different time intervals. The solid lines are fitted by the equation $r(t) = r^2(0) + v^2t^2$ where $r(t)$ is the rms-radius of the atomic cloud at time t. The temperature is estimated from the relation $T = mv^2/k_B$ where m is the mass of the atom and k_B is the Boltzmann constant.

In the quadrupole coil configuration, 1 A current gives a magnetic field gradient of 231 μT/cm. A magnetic field gradient of 7.4 mT/cm is used for the blue MOT. The loading time for the blue MOT is about 150 ms. Around 3×10^7 atoms are captured in the blue MOT. The lifetime of the MOT was measured to be 53 ms. In order to not

saturate the transition during detection, a 0.03 mW/cm^2 beam is used for absorption imaging in order to determine the temperature of atoms in the MOT. The absorption imaging system consists of two achromat lenses of focal length $f = 300$ mm back to back each in $f - f$ configuration to provide a magnification of 1.

Fig. 3.4 shows the rms radii r_x, r_y of the expanding cloud of atoms along the directions perpendicular and parallel to gravity at different time intervals. The fit gives the value of the temperature to be $\sim$2.5 mK (see table 2.2 for Doppler limit) which is limited by extra heating mechanisms due to fluctuations in the laser intensity [68]. The difference in cloud dimensions in the x (horizontal) and y (vertical) directions could be attributed to imperfections in the MOT beam alignment.

3.2.1   Repumping lasers set up
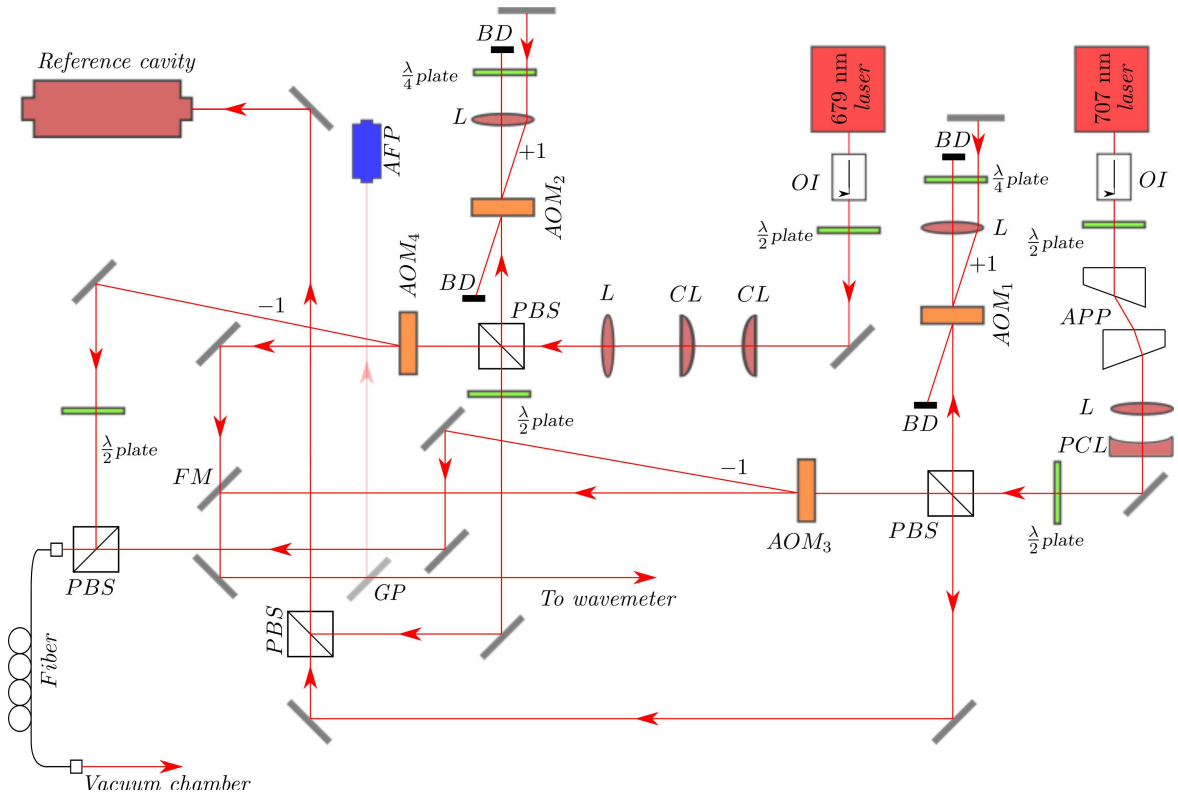
Figure 3.5: Schematic of the repumping laser setup. *L*: Lens, *PBS*: Polarizing beam splitter, *AOM*: Acousto optic modulator, *BD*: Beam dump, *AFP*: Analyzer Fabry Perot, *APP*: Anamorphic prism pairs, *FM*: Flip mirror, *GP*: Glass plate, *OI*: Optical isolator, *CL*: Cylindrical lens and *PCL*: Plano concave lens. The shutter (not shown in the figure) is placed near the entry port (after *PBS*) of the fiber.

The setup of repumping lasers is shown in fig. 3.5. The repumping lasers serve to bring the atoms in the excited clock state back to ground state for detection. They are also used to improve the atom number in the blue MOT by an order of magnitude by repumping the atoms from $^3P_0$ and $^3P_2$ states to $^3P_1$ which then decays back to ground

state (see fig. 2.1). Two commercial lasers, Sacher (TEC 100) for 679 nm and Toptica (DL 100) for 707 nm are used. The two lasers are frequency stabilized to a single reference cavity using orthogonal polarizations. The reference cavity is 103 mm long and has a free spectral range (FSR) of 1.45 GHz. The cavity is temperature stabilized to 23°C and is kept in a vacuum chamber. The offset frequency for the stabilization is given by AOM_1 (80 MHz) and AOM_2 (80 MHz). The detuning and switching of the repump lasers are provided by AOM_3 (200 MHz) and AOM_4 (200 MHz) for 707 nm and 679 nm lasers. An additional mechanical shutter is used to block stray light from the repumper. Both the 679 nm and 707 nm laser light are coupled into a single-mode polarization maintaining fiber. A transfer efficiency of 50% gives an output power of 1.3 mW for 679 nm and 200 μW for 707 nm, the radius of the repumper beams is $\sim$ 5 mm.
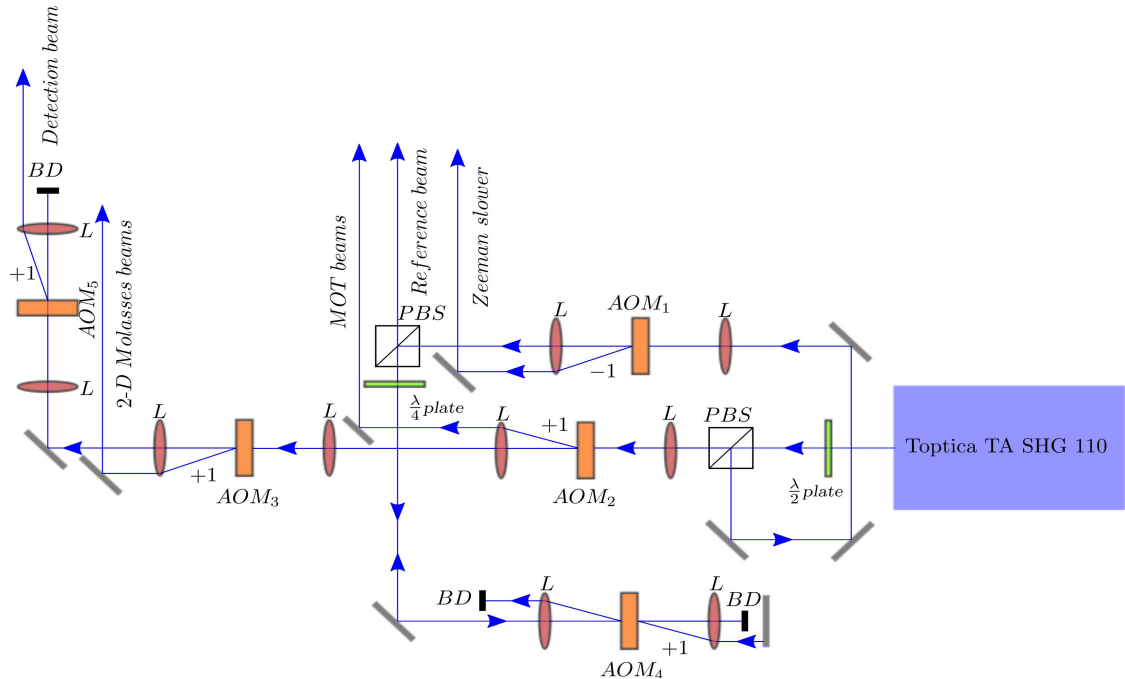
3.3 Experimental realization of 689 nm red MOT
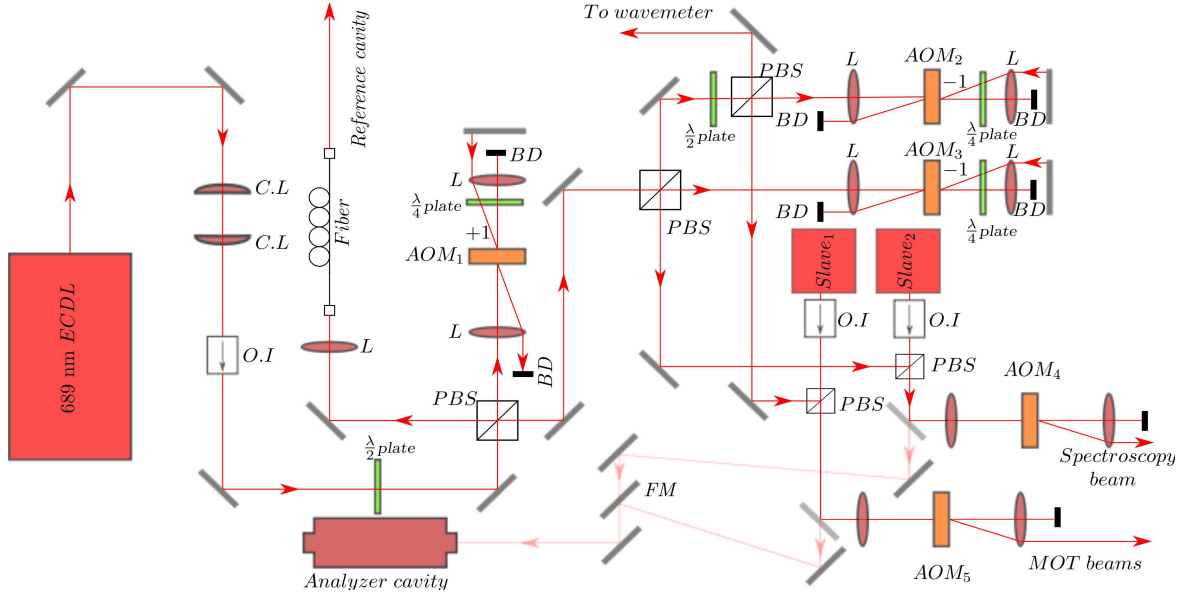
Figure 3.6: Schematic of the 689 nm laser setup. *L*: Lens, *PBS*: Polarizing beam splitter, *AOM*: Acousto-optic modulator, *BD*: Beam dump, *FM*: Flip mirror, *OI*: Optical isolator and *CL*: Cylindrical lens.

To further cool the atoms down to microkelvin temperatures, the intercombination $^1S_0 \rightarrow {}^3P_1$ transition at 689 nm is used. The laser setup for the 689 nm cooling transition is shown in fig. 3.6. The setup consists of one master diode laser and two injection locked slave diode lasers. The master laser is a home built extended cavity diode laser (ECDL) in Littrow configuration [69]. The master diode gives an output power of 11 mW. The master laser is frequency stabilized to a reference cavity using the Pound-Drever-Hall (PDH) technique [70, 71]. The reference cavity has a 3 GHz free spectral range and is kept inside a vacuum chamber with pressure $< 10^{-6}$ mbar, maintained at

a temperature of 25°C. By monitoring the resonance frequency drift over long a long period of time, the cavity drift rate was determined to be 21 kHz per day. The light from the master laser is detuned by two 80 MHz double-pass AOM before being used for injection locking two slave lasers, one slave for cooling the atoms and the other for spectroscopy on the 689 nm transition. The slave laser diodes give an output power of 30 mW. Additional 106 MHz AOM is used for switching and varying the power in the MOT beams during the two sub-stages of cooling. The beams are coupled into single-mode polarization maintaining fibers for mode cleaning with a 40% transfer efficiency. The red MOT beams are formed by three independent beams which are retro-reflected and have a $1/e^2$ diameter of 5.4 mm.

Blue cooling   150 ms $\frac{dB}{dz} = 7.4$ mT/cm
                                                    I_{tot}=25 mW/cm^2

Broadband cooling   30 ms $\frac{dB}{dz} = 0.7$ mT/cm
                                                    I_{tot}=8 mW/cm^2

Single frequency cooling   50 ms $\frac{dB}{dz} = 0.7$ mT/cm
                                                    I_{tot}=445 μW/cm^2

g

Blue MOT   Broadband   Single frequency
            MOT   MOT
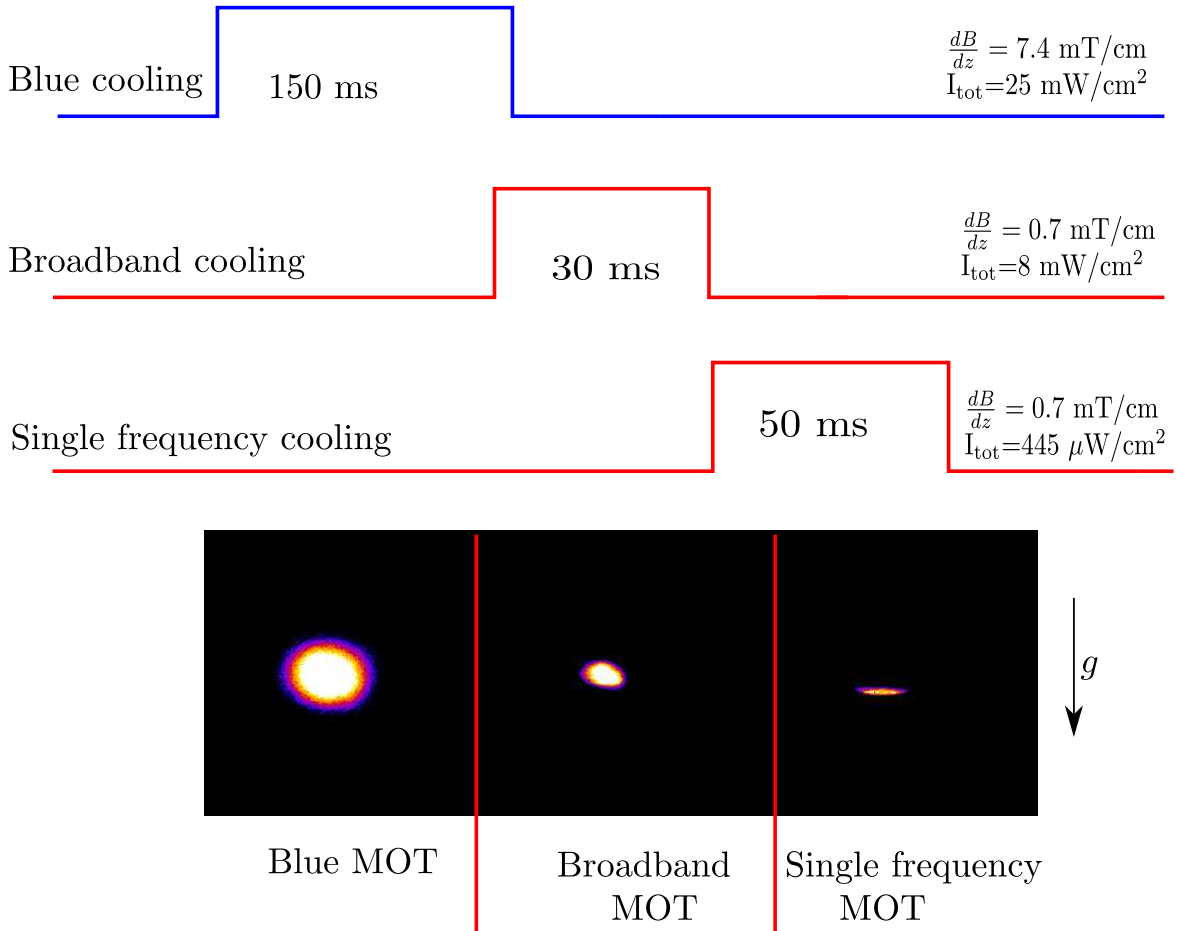
Figure 3.7: Timing diagram to obtain ultra-cold atoms and the corresponding absorption images.

The cooling on the $^1S_0 \rightarrow {}^3P_1$ transition involves two sub-stages to overcome the limitation of capture velocity range imposed by the narrow linewidth (7.6 kHz) of the transition [72]. The two sub-stages are called the broadband stage and single frequency stage. During the broadband stage, the cooling laser frequency is detuned 1.6 MHz below the $^1S_0 \rightarrow {}^3P_1$ transition and a sinusoidal modulation of 50 kHz is applied to the 80 MHz cooling AOM to broaden the laser resulting in a maximum frequency span of

3 MHz. At the high frequency edge of the spectrum, the laser is 100 kHz red detuned from the transition. This broadening of cooling lasers increases the velocity capture range, leading to increased capture of atoms from the blue MOT stage. The total peak intensity (6 beams) for cooling beams during this stage is 8 mW/cm^2 and the magnetic field gradient is 0.7 mT/cm. This broadband cooling stage lasts for 30 ms and at the end of this stage around 1.6×10^7 atoms are captured with a temperature of 15 μK.

After the broadband stage, the modulation is turned off and the laser power is reduced by using AOM_5 (see fig. 3.6) to a total peak intensity is 445 μW/cm^2 while the magnetic field gradient remains the same, the cooling laser is detuned 800 kHz below the $^1S_0 \rightarrow ^3P_1$ transition. This single-frequency stage lasts for another 50 ms. At the end of the single-frequency stage, we get around 9×10^7 atoms with a temperature of ~ 3 μK. During the cooling process, stray light from the 461 nm beams are blocked using mechanical shutters. The transfer of atoms from the blue to the single-frequency red MOT is around 30%. Fig. 3.7 shows the timing diagram used for cooling the atoms down to ultra-cold temperatures.
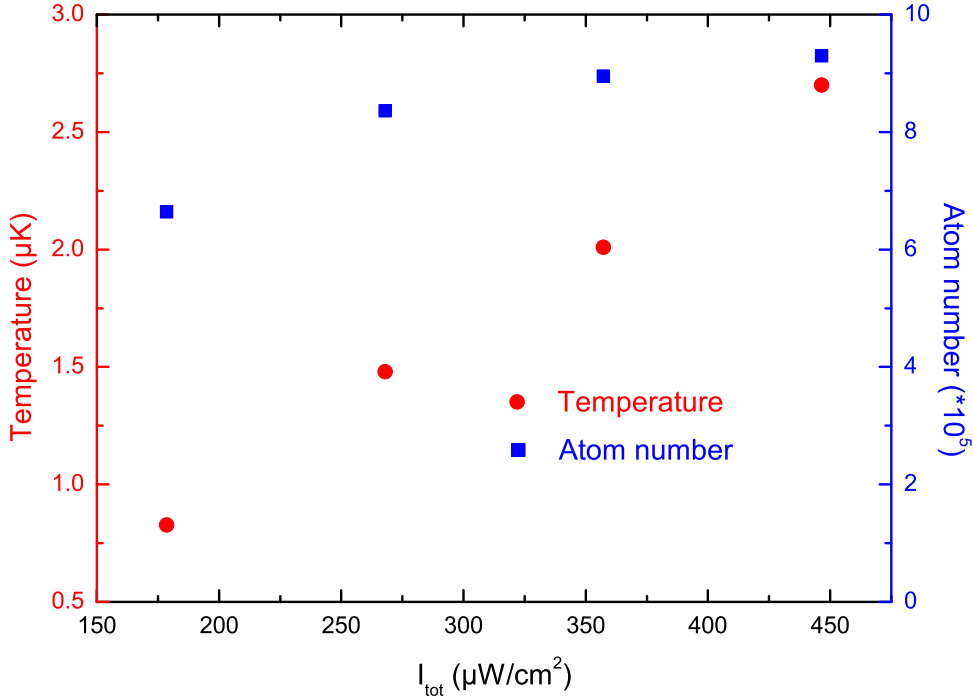
Figure 3.8: Variation of atom number and temperature with respect to total laser intensity I_{tot}.

The variation of the temperature and number of atoms after the single-frequency cooling stage with respect to the total peak intensity of the cooling beams is shown in fig. 3.8. The temperature of the atoms decreased as the intensity of the cooling beams

were reduced. The temperature dependence on such low intensities shown in fig. 3.8 can be explained by noting that at such low intensities, the recoil energy becomes important and cooling becomes fully quantum mechanical [73]. Since the intensities of the cooling beams are higher than the saturation intensity (see tab. 2.2), the transition is power broadened. Hence the decrease in the atom number is due to the decrease of the capture velocity range of the trap [73]. The lifetime of the single-frequency red MOT was measured to be ~ 460 ms. Since the radiation force for single frequency cooling is comparable to the gravitational force, the atoms settle at the bottom of the of the trap where the laser frequency detuning balances the Zeeman shift [74]. This is evident from the absorption image as shown in fig. 3.7 taken after the single frequency cooling stage. The atoms rebound at a point $z_0 \sim \delta/(\beta \frac{dB}{dz})$ from the trap center, where $\delta = 800$ kHz and $\beta = 2.1 \times 10^4$ MHz/T is the Zeeman shift coefficient for the $^1S_0 {\rightarrow} ^3P_1$. Substituting these values, we find that $z_0 \sim 550$ μm.

3.4   Loading of atoms into 813 nm optical lattice

The atoms cooled in the first two stages should be loaded into the optical lattice in order to interrogate the clock transition. The setup for the lattice laser is shown in fig. 3.9.
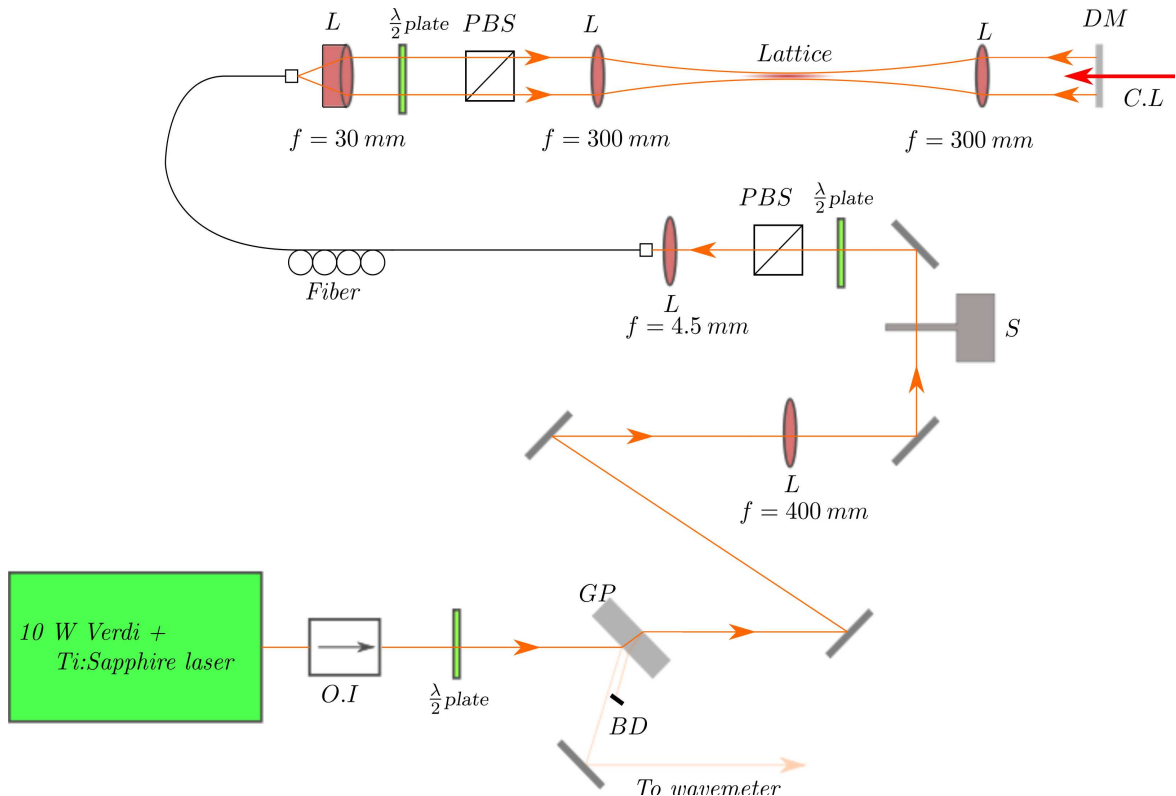
Figure 3.9: Schematic of the lattice laser setup. *L*: Lens, *PBS*: Polarizing beam splitter, *BD*: Beam dump, *OI*: Optical isolator, *DM*: Dichroic mirror, *C.L*: Clock laser and *S*: Shutter.

It consists of a Coherent 10 Watt Verdi at 532 nm pumping a Ti:Sapphire laser resulting in an output power of ~ 1.3 W at 813 nm. The 813 nm laser light passes through polarization optics and $f = 400$ mm, $f = 4.5$ mm mode-matching lenses before being coupled into a single-mode polarization maintaining fiber with a mode-field diameter of ~ 5 μm. The transfer efficiency through the fiber is close to 65%. The light coming out of the fiber is collimated by a $f = 30$ mm lens and passes through a half-wave plate and a polarizing beam cube. The half-wave plate and the polarizing beam cube in the lattice laser set is used for varying the power in the lattice beam. The beam is then focused into the vacuum chamber by a $f = 300$ mm lens and a polarization cube makes the polarization of the lattice beam is perpendicular to the gravity and the axis of the quadrupole/Helmholtz coils. The optical lattice is formed by recollimating the beam and retro-reflecting the beam using a dichroic mirror which reflects light at 813 nm and transmits clock laser light at 698 nm. The outcoupler and mirror of lattice setup is mounted on a five-axis kinematic stages on the opposite sides
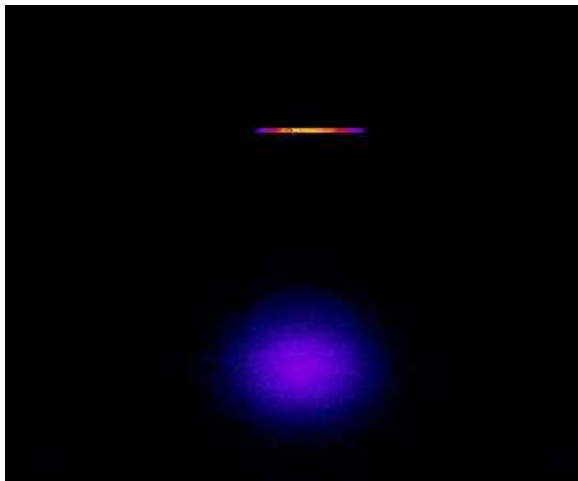
Figure 3.10: Absorption image showing atoms trapped in the optical lattice and the untrapped atoms falling down.

of the vacuum chamber for overlapping the lattice beam with the MOT. The switching of lattice laser is done by using a mechanical shutter. The lattice beam is turned on during the whole cooling process so that loading of the atoms into the lattice takes place simultaneously while they are being laser cooled. Fig. 3.10 shows the atoms trapped in optical lattice.

High atom numbers ($\sim 10^6$) in the optical lattice were determined usually from absorption images. Since the images are noisy at low atom number, we calibrate the fluorescence signal from the $^1S_0 \rightarrow ^1P_1$ transition to the corresponding high atom numbers obtained from the absorption images. In order to obtain fluorescence signal from the atoms trapped in the optical lattice, a short blue MOT phase lasting for 20 ms is used. During this short phase, the blue fluorescence signal proportional to the atom number in the ground state is detected. Getting a good SNR is the reason behind having the small blue MOT phase instead of a single detection beam. A waiting time of 150 ms is used before starting the small blue MOT phase to make sure that the
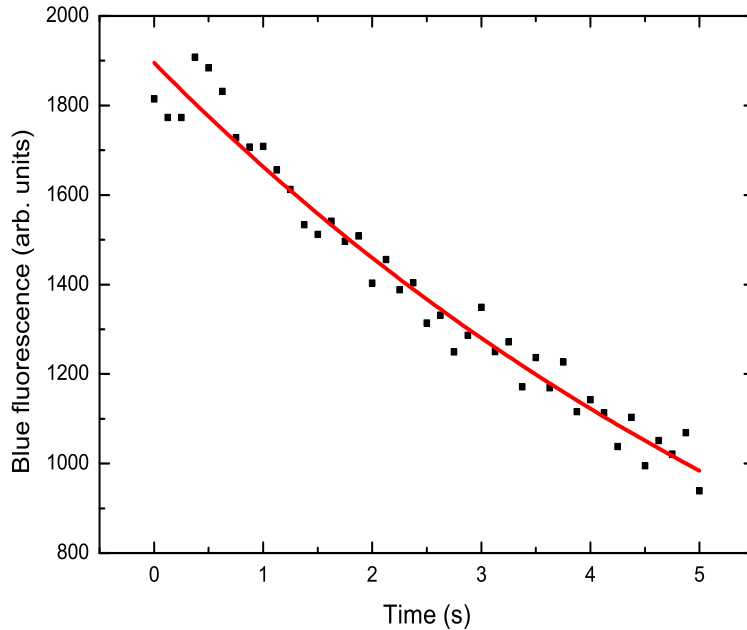
Figure 3.11: Blue fluorescence signal proportional to the atom number versus time. The line is an exponential fit and gives the lifetime of the atoms in the lattice to be 7.5 s.

falling untrapped atoms do not get recaptured. At high atom number, the saturation of images is avoided by turning off the lattice and allowing the atoms to expand for 10 ms before taking the image. We estimate low atom numbers by assuming a linear relation between the fluorescence signal and atom number. The depletion of atom number (given by the blue fluorescence) in the lattice with respect to time is shown in fig. 3.11. An exponential fit gives a lifetime of ~ 7.5 s which is much more than the time taken for an experiment cycle in our case (~ 1 s). The lifetime is limited by background gas collisions.

3.5 Waist radius determination of optical lattice

In order to determine the waist radius of the lattice beam which is important to derive quantities like atomic densities, a dipole trap was formed by blocking the retro-reflected beam. The atoms were initially loaded in a position which is away from the potential minimum of the dipole trap in the axial direction. This is done by applying an offset magnetic field in addition to the quadrupole magnetic field used for the $^1S_0 - ^3P_1$ MOT. The oscillation of the center of mass of the atomic cloud along the axial direction of the dipole trap is determined from absorption images.

The position of the center of mass of the atoms at different times of evolution is

31
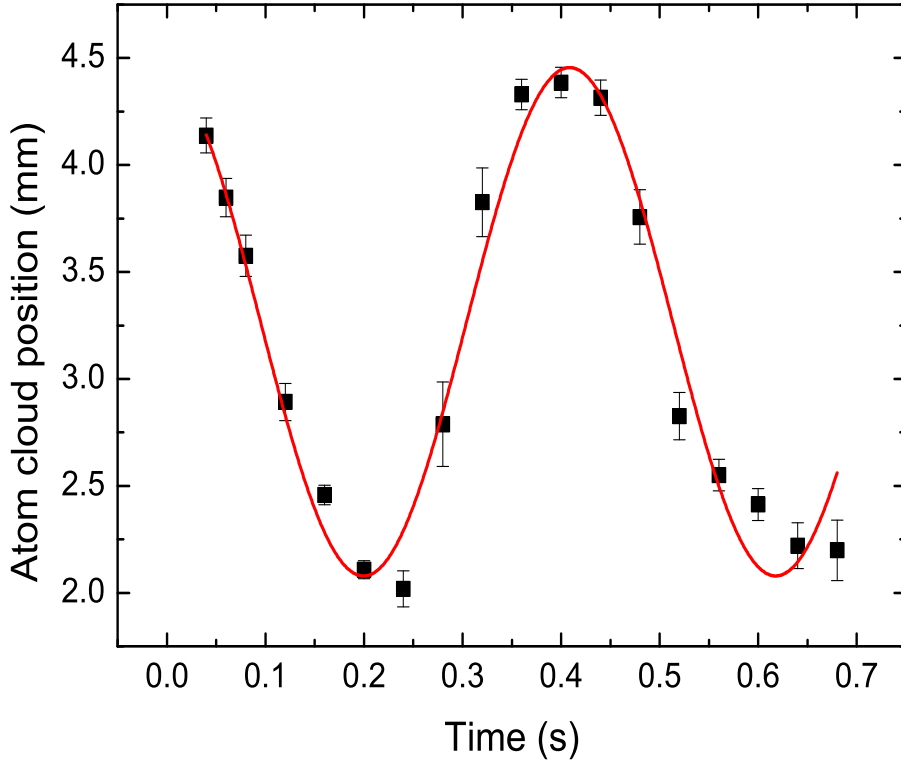
Figure 3.12: Trap oscillations in axial direction excited by loading the atoms at a position away from the potential minimum of the dipole trap. The power of the dipole beam is 600 mW. Squares represent the measured position of the center of mass of the atoms in the dipole trap. The solid line is a sinusoidal fit to the data.

shown in fig 3.12. The sinusoidal fit to the data gives an angular frequency $\omega_z = 15$ rad s^{-1}. The relation between trapping frequency and potential depth is given as [75]

$$\omega_z = \sqrt{\frac{2U}{mz_R^2}} \tag{3.1}$$

where m is the mass and z_R is the Rayleigh range($z_R = \frac{\pi\omega_0^2}{\lambda}$). Using eq. 3.1 the waist radius ω_0 was found to be (32 ± 2) μm. The same method was used to find the waist radius of the retro-reflected beam by loading the atoms in the reflected beam that is purposely not overlapped with the incoming beam. This method was also used to place the axial positions of the foci of the dipole trap beams at the position of the MOT and thus assure that the foci of both beams coincide.

When we did spectroscopy on the clock transition for atoms in the lattice, we found a discrepancy between observed axial sideband frequencies and calculated axial sideband frequencies. The axial sideband frequencies depend on the power of the lattice beam (see eq. 2.16). For a waist radius of 32 μm and a power of 600 mW, the expected sideband frequency is at $\sim$ 172 kHz but the sideband frequency was at $\sim$ 86 kHz. The calculated sideband frequencies agreed with the observed values for lattice laser powers less than 150 mW. Initial doubts about the waist radius of the

lattice beam was resolved by repeated measurements of the waist radius. During the initial stages of the experiment, the lattice laser set up was located in the neighboring lab and due to this reason, a 25 m long fiber was used.
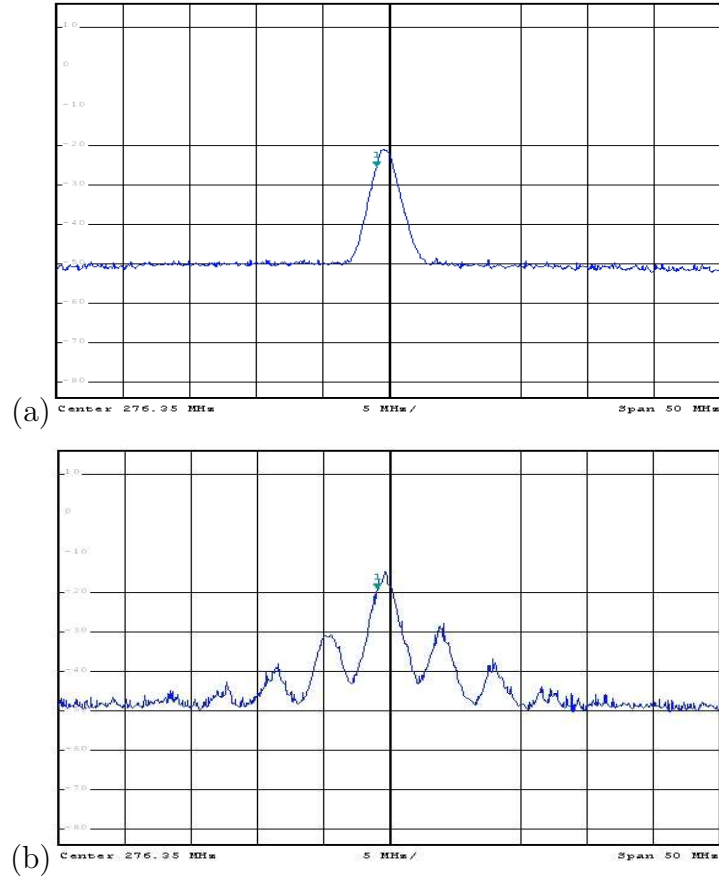
Figure 3.13: Spectrum of laser amplitude fluctuations measured with a fast-photodiode after the fiber. (a) For powers less than 500 mW in the free running beam or for powers less than 150 mW in the lattice beam. (b) Spectrum of fast-photodiode for powers more than 500 mW in the free running beam or for powers more than 150 mW in the lattice beam.

In order to search for a possible hint to nonlinear processes [76, 77] in the fiber (which could result in spectral broadening of the laser), a fast-photodiode was placed on the side of the polarizing beam cube located before the $f = 300$ mm focusing lens (see fig. 3.9) and the reflected light from the polarizing beam cube was focused on the fast photo-diode. The power was gradually increased for the free running beam (no retrorefection). Fig. 3.13(a) shows the spectrum of the fast-photodiode where a peak at 276 MHz was observed for powers less than 500 mW. Multiple peaks as shown in fig. 3.13(b) were observed when the power is increased above 500 mW. In the lattice configuration (with retroreflected beam), when the power was less than 150 mW per beam, the spectrum was identical to fig. 3.13(a) and for powers more 150 mW, the spectrum was same as fig. 3.13(b). We attribute these single and multiple peaks to

interference in the fiber due to cascaded nonlinear process such as Brillouin scattering. Since nonlinear processes depend on the fiber length, the lattice setup was moved close to the experiment and a 3 m fiber with the same mode field diameter as the long fiber was used. With the short 3 m fiber, up to 300 mW (resulting in a potential depth of $\sim 50~\mu K$) of power showed no indications of nonlinear processes and the calculated sideband frequencies matched the observed values for powers up to 300 mW. Further investigations to reveal the nature of the these processes were not carried out since they are beyond the scope of this thesis.

3.6 The 698 nm clock laser
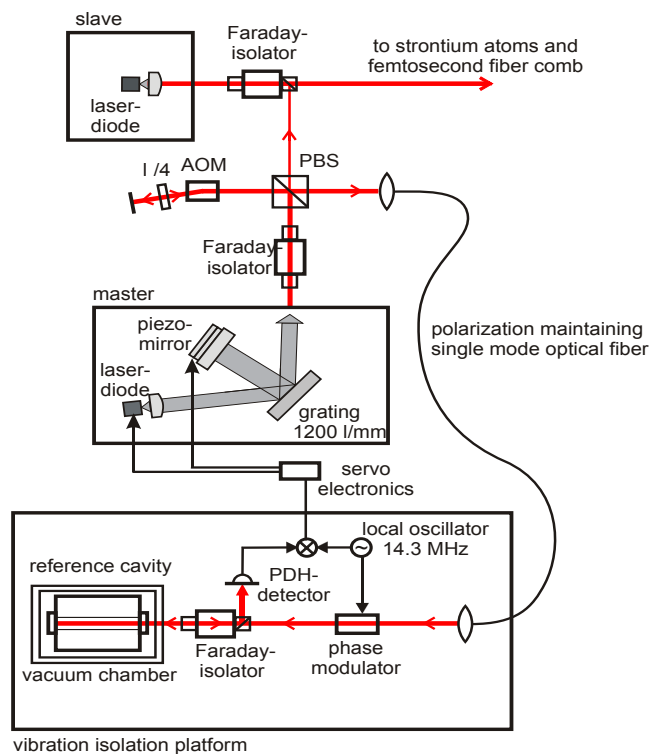
Figure 3.14: Schematic [2] of the 689 nm clock laser setup.

Vibrations, thermal noise and expansion of the reference cavity to which the clock laser is stabilized leads frequency drift and noise in the laser. These effects limit the stability and quality factor of an optical frequency standard. A stable clock laser is also important for our investigation on collisions. For example, narrow linewidth of clock laser is desirable to study collisional broadening of the clock transition over a large dynamic range (atoms in this case).

The schematic of the clock laser system is shown in fig. 3.14. The setup for the 698 nm clock laser [2] consists essentially of a stabilized master laser and an injection locked slave laser. The master laser is an extended cavity diode laser in Littman

configuration [69] and gives an output power of 4 mW. Stabilization of the master laser onto a high-finesse ultra-stable optical cavity is done using the Pound-Drever-Hall (PDH) technique [70, 71]. The frequency offset between the laser and the cavity is bridged by a double pass 200 MHz offset AOM. The optical cavity is 100 mm long and it is made of ULE (ultra-low expansion) glass. Optical axis of the cavity is oriented perpendicular to gravity (horizontally mounted). In order to minimize the sensitivity to vertical vibrations, small drilled invar plates were glued at four points near its horizontal symmetry plane and viton cylinders were used to support the cavity. The cavity is enclosed in a copper cylinder which acts as heat shield. The cavity finesse is 330,000 which corresponds to a linewidth of 4.5 kHz and it is kept in a vacuum chamber ($\sim 10^{-7}$ mbar) which is temperature stabilized to 24°C.

The influence of the mechanical and acoustic vibrations on the cavity is minimized by mounting the cavity on a vibration isolation platform which in turn is placed in an acoustic isolation box. A 1.5 m long polarization-maintaining single-mode fiber is used to couple the light from the master laser to to optical cavity. The linewidth of the laser is close to 30 Hz which is limited by problems in vibration isolation. However, by phase locking our clock laser to another narrow linewidth reference laser at 657 nm (used for calcium experiments), the linewidth can be reduced to few Hz. The slave laser gives an output power of 23 mW which is used for the spectroscopy of the clock transition and also for the femtosecond laser comb. An additional 80 MHz AOM (not shown in figure) is used for switching on and off the clock laser during the experiment to probe the clock transition.

3.7 Spectroscopy on 698 nm the clock transition

The state mixing of the $^3P_1$ and $^3P_0$ states necessary for the excitation on the clock transition is done by applying a magnetic field. The coils in the Helmholtz configuration provide a magnetic field of 0.5 mT/A. The clock beam has a waist radius of 39 μm and its polarization is parallel to the applied magnetic field. It is overlapped with the lattice through a dichroic mirror. A camera is used to check the extent of overlap between the lattice laser beam and the clock laser beam. A pellicle-beamsplitter can be placed in the lattice laser path to deflect a part of the retro-reflected beam and the clock laser beam which allows to observe the deflected beams at two or more points.

To measure the number of atoms that have been excited by the interaction with the clock laser, either the reduction of the number of atoms in the $^1S_0$ ground state can be measured or the increase in the number of atoms in the excited $^3P_0$ state. The two methods are shown in fig. 3.15. The first method is by detecting the fluorescence of the remaining ground state $^1S_0$ atoms by the 20 ms 461 nm MOT phase. Ground state atom detection would result in longer cycle time because atoms which are not trapped in the lattice takes finite time (~ 150 ms) to fall down to a distance such that they cannot be detected. The second method involves pushing away the remaining ground state $^1S_0$ atoms by using a resonant 461 nm beam immediately after the excitation to $^3P_0$ state. The excited state atoms are then brought back to the ground state by
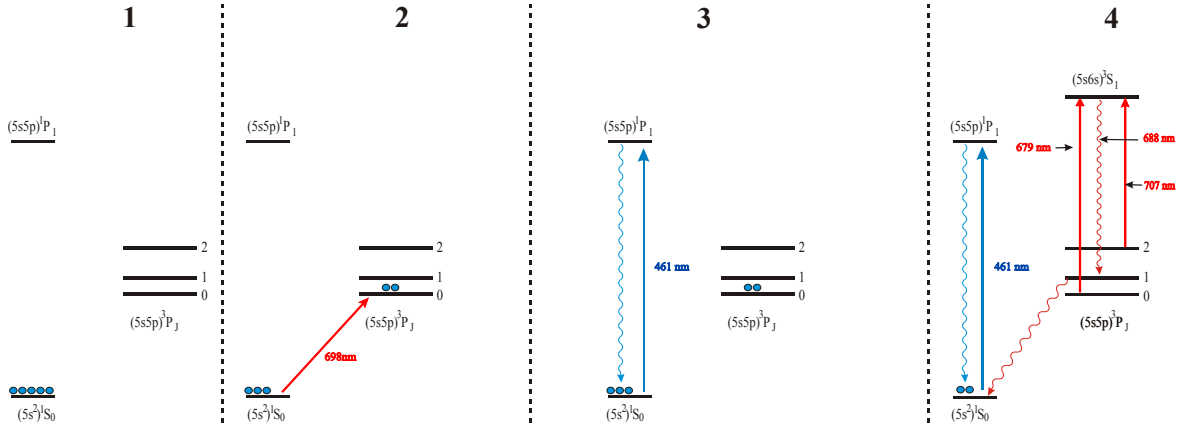
Figure 3.15: Schematic of the detection of clock transition. 1: Atoms are initially at the ground state. 2: Clock transition drives a fraction of the ground state atoms to the clock excited state. 3: The remaining ground state atoms can be detected (or blown away) using the 461 nm transition. 4: Using 679 nm and 707 nm repump lasers, the excited state atoms can be brought to the ground state and be detected.

optically pumping them to the $^3S_1$ state using 679 nm and 707 nm lasers and the fluorescence is detected using the 20 ms 461 nm MOT phase. Colliding atoms can absorb a photon and get lost from the trap by forming an electronically excited molecule. Such light assisted density dependent photo-associative losses from the repumping light [78] were avoided by switching off the lattice beam and allowing the cloud of excited state atoms to expand before repumping.

After loading the atoms into the lattice, a static magnetic field up to 3 mT is applied. The clock laser beam of $\sim$ 2.5 mW of power is used to excite the atoms to the $^3P_0$ state. In order to find the clock transition, the clock laser frequency is varied by scanning the master laser-cavity offset AOM.

Fig. 3.16 shows the spectrum of the clock transition in the Lamb-Dicke regime. The Rabi frequencies for the red and blue sidebands in the Lamb-Dicke regime are given as [79]

$$
\begin{aligned}
\Omega_{n,n-1} &= \Omega\sqrt{n}\,\eta \\
\Omega_{n,n+1} &= \Omega\sqrt{n+1}\,\eta
\end{aligned}
\tag{3.2}
$$

where Ω is the Rabi frequency of the carrier transition. We see that the Rabi frequencies of the sidebands are suppressed with respect to Ω. Therefore, in order to observe the sidebands, one has to saturate the carrier (clock) transition. The incoming beam power of the trapping laser was $\sim$ 120 mW. For the given power (120 mW) and waist radius (32 ± 2 μm) of the lattice beam, the position of axial sidebands ν_z (see eq. 2.16) are expected to be tens of kilohertz away from the carrier transition. Since the clock transition is narrow compared to the axial trap frequency we see three resolved absorptions, one carrier and two sidebands. Eqs. 2.4 and 2.6, are used to explain the observed spectrum.
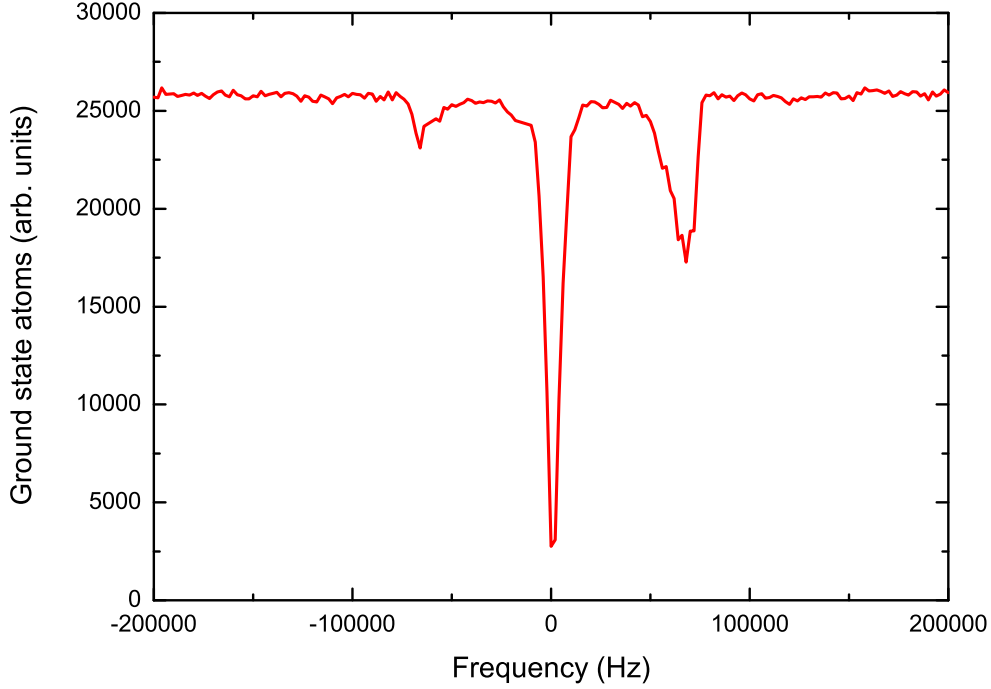
Figure 3.16: Spectroscopy on the $^1S_0 \to {}^3P_0$ transition showing the carrier (clock transition) and the 1$^{\text{st}}$ order sideband transitions. The duration of the clock laser pulse is 500 ms.

The carrier absorption occurs when the change in the motional quantum number is zero ($n_f = n_i$) , in this case, the atoms absorb light at frequency $\nu = \nu_0$ where ν_0 is the clock transition frequency. The sideband at higher frequency occurs when the change in the motional quantum number is 1 ($n_f = n_i + 1$), the atoms absorb light at frequency $\nu = \nu_0 + \nu_z$ where ν_z is the axial trap frequency. Finally, a change of -1 in the motional quantum number results in the occurrence of red sideband at frequency $\nu = \nu_0 - \nu_z$. The ratio between blue and red sidebands is $(n_i + 1)/n_i$. The sidebands are at ~ 72 kHz. Using eq. 2.16 for axial frequency we obtain a waist radius of ~ 34 μm. The recoil frequency for $^1S_0 \to {}^3P_0$ clock transition is ~ 4.7 kHz giving for this spectrum, a Lamb-Dicke parameter $\eta = 0.26$.

In a harmonic potential with $E_n = \hbar\omega(n + \frac{1}{2})$, one can calculate the rms width atom distribution along z direction where w_{rms} is

$$(w_{\text{rms}})_z = z_0 \sqrt{2 \langle n_z \rangle + 1} \tag{3.3}$$

with $z_0 = \sqrt{\hbar/2m(2\pi\nu_z)}$ and n_z being the motional quantum number in the z direction. Since atoms are distributed among different levels of the harmonic trap, the average

value $\langle n_z \rangle$ is determined using the Boltzmann distribution

$$\langle n_z \rangle = \sum_{n_z} P(n_z)n_z = \frac{\sum_{n_z=0}^{\infty} n_z e^{\frac{-n_z h\nu_z}{k_B T}}}{\sum_{n_z=0}^{\infty} e^{\frac{-n_z h\nu_z}{k_B T}}} = \frac{e^{\frac{-h\nu_z}{k_B T}}}{1 - e^{\frac{-h\nu_z}{k_B T}}}. \tag{3.4}$$

By knowing the temperature and the sidebands, one can calculate the rms width. Treatment of rms width and average n can be extended along the radial direction to determine the radial rms width $(w_{\rm rms})_r$ by calculating ν_r from eq. 2.16. The value of $\langle n_z \rangle$ can also be determined from the observed sidebands using the fact that the the blue and red sidebands are suppressed by a factor of $\eta^2(\langle n_z \rangle_i + 1)$ and $\eta^2(\langle n_z \rangle_i)$ with respect to the carrier transition. $\langle n_z \rangle_i$ is the average value of the initial motional quantum number. The ratio of axial blue and red sidebands in the axial direction is then given as

$$\frac{S_B}{S_R} = \frac{\langle n_z \rangle_i + 1}{\langle n_z \rangle_i} \tag{3.5}$$

where S_B (S_R) is the blue (red) sideband absorption signal. By taking the ratio of blue and red sideband absorption signals in fig. 3.16 we get $\langle n_z \rangle_i = 0.45$ which agrees with the calculated value from eq. 3.4 for a cloud temperature of ~ 3 μK. Also using eqs. 3.4 and 3.5, we can relate the temperature and sidebands as

$$T = \frac{h\nu_z}{k_B \ln(\frac{S_B}{S_R})}. \tag{3.6}$$

Knowing the ratio of the sideband signals and the axial frequency, one can calculate the temperature of the atomic sample in the lattice. From fig. 3.16 and eq. 3.6 the temperature is calculated to be ~ 3 μK which agrees with the temperature measured using expansion images. The asymmetric broadened sidebands are the result of radial motion of the atoms. As the atoms move out radially from the trap center (maximum intensity), the axial frequency ν_z decreases due to decrease in intensity. This leads broadening at frequencies $\nu = \nu_0 \pm \nu_z$ and hence the sidebands are asymmetrically broadened towards the carrier transition.

A strongly saturated transition for a two-level atom should eventually lead to a 50% population in ground and excited states. Fig. 3.16 shows a near zero depletion of ground state atoms after a 500 ms clock pulse giving us strong indications for inelastic loss mechanism. For 2.5 mW of clock laser power and 3 mT homogeneous magnetic field, the Rabi frequency is calculated to be $\Omega/2\pi \sim 30$ Hz and π pulse length is 16 ms. Fig. 3.17 shows the decay of ground state atoms with respect to clock pulse length for two different atom numbers 2×10^6 and 1×10^5. For high atom number the population decayed to near zero value but for low atom number, the population reached an equilibrium although no Rabi oscillation were observed. This gives us evidence for density dependent inelastic losses and strong damping due to decoherence. Collisional broadening was also observed, fig 3.18 shows a preliminary result of the dependence of linewidth of the atomic transition on the atom number showing evidence of density dependent broadening taking place. These effects must be studied and understood in order to find how they affect a ^{88}Sr based optical lattice clock in terms of accuracy and stability which is the focus of next chapter.
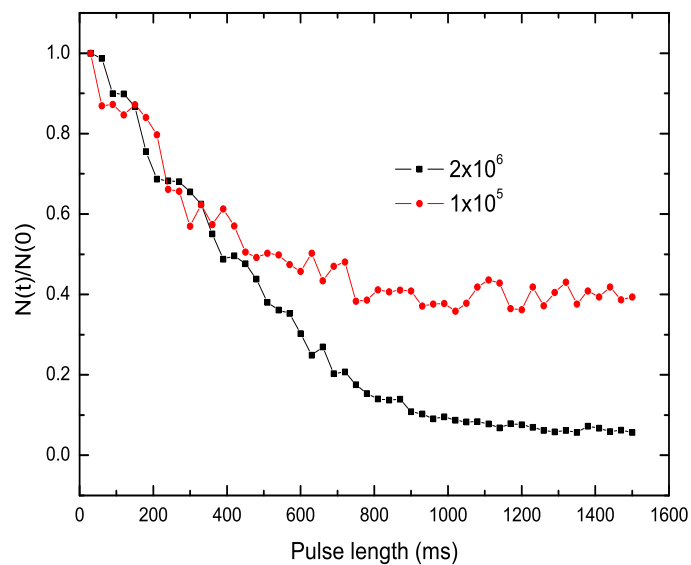
Figure 3.17: Decay of ground state atoms with respect to clock laser pulse length for two different initial atom numbers
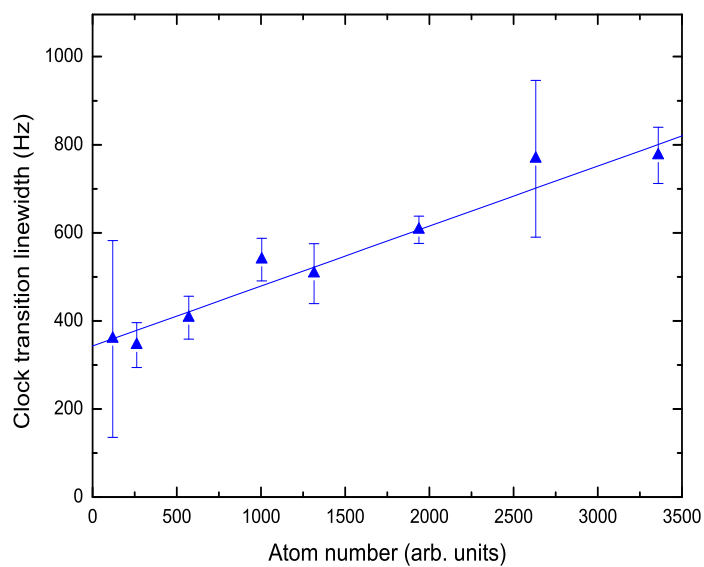
Figure 3.18: Clock transition linewidth vs ground state atom number given in arbitrary units. The straight line is a linear fit to the measured data.

Chapter 4

Inelastic collisions and decoherence effects in a 1-D ^{88}Sr lattice clock

In this chapter, results of the investigation of the losses due to $^1S_0+^3P_0$ and $^3P_0+^3P_0$ inelastic collisions, density-dependent broadening and decoherence effects are presented. Section 4.1 describes the study of collisional losses by observing temporal variation of the atoms in the lattice. Since $^3P_0+^3P_0$ collisions also occur in an ensemble of $^3P_0$ and $^1S_0$ atoms, $^3P_0+^3P_0$ collisions are observed first and the loss rate is determined. This loss rate is then used to fit the decay and determine the loss rate due to $^1S_0+^3P_0$ collisions. The observations reveal that the dominating loss mechanism are the $^3P_0+^3P_0$ collisions. Section 4.2 presents the study of broadening and decoherence effects for different atom numbers in which an additional dephasing mechanism is identified.

4.1 Inelastic collisional losses in the optical lattice

Collision between two particles, depending on the outcome, can be classified into two main categories namely elastic and inelastic.

- In an elastic collision, the kinetic energy of relative motion of the two bodies does not change, though their velocities and individual kinetic energies may change.

- In an inelastic collision, the energy is transferred between internal and relative kinetic energy.

At very low energies, scattering is mainly dominated by s-waves and the scattering cross-section can be expressed in terms of a parameter called the scattering length. In case of atoms which have several internal states such as L (orbital angular momentum), J (total angular momentum), S (spin angular momentum), several collision channels are possible. The atoms can be initially prepared in one of the several possible quantum states and the collision channels can be specified by a set of quantum numbers representing the state of each atom and the partial wave. For a single channel scattering where only elastic scattering is possible, the scattering cross-section in the s-wave

limit is given as $\sigma = 4\pi a^2$ where a is the scattering length. For multichannel scattering, the scattering length is a complex number $a = \alpha - i\beta$. In case of multichannel scattering, the elastic scattering cross section contribution from s-wave collision is

$$\sigma = 4g\pi(\alpha^2 + \beta^2). \tag{4.1}$$

For s-wave inelastic collisions that remove atoms from a channel, the loss rate coefficient γ_{loss} is

$$\gamma_{\text{loss}} = 2g\frac{h}{m_\mu}\beta. \tag{4.2}$$

The factor g (two particle correlation function) is equal to 1 when the atoms are bosons or fermions that are not in identical states, g = 2 or 1 for two bosons in identical states in a normal thermal gas or a Bose-Einstein condensate and g = 0 for two identical fermions.

In order to study and characterize the collisional properties between ground ($^1S_0$) and excited state atoms ($^3P_0$) of the clock transition, we load the atoms in the optical lattice using a 150 ms blue MOT loading time followed by a 30 ms broadband cooling and a 50 ms single frequency cooling. The optical lattice with 300 mW of power is overlapped throughout the cooling process so that atoms are simultaneously loaded into the optical lattice while they are cooled. Before applying the clock laser pulse, a 150 ms wait time ensures that the untrapped atoms fall away. A 3 mT Helmholtz field and a clock laser intensity of 125 W/cm^2 ($\Omega_R/2\pi \sim 33$ Hz) are applied to excite the atoms to the $^3P_0$ state. The clock pulse length is 20 ms. After the excitation an ensemble of ground and excited state atoms is present in the optical lattice. The rate at which the atoms are lost from the trap can determined by the time dependence of the number of atoms in the trap.

Possible collisions in the lattice include the inelastic $^1S_0+^3P_0$ and $^3P_0+^3P_0$ and the elastic $^1S_0+^1S_0$ collisions. The atoms are held in the trap for variable amount of time (trapping time) before they are detected. In order to differentiate between $^1S_0+^3P_0$ and $^3P_0+^3P_0$ collisional processes, we conduct two separate measurements. To study the $^3P_0+^3P_0$ collisional process, ground state atoms are blown away by using 461 nm blow beam for 20 ms immediately after we excite the atoms, leaving only the excited state atoms in the lattice. After a variable trapping time, the atoms in the lattice are allowed to expand for 10 ms by switching off the lattice in order to avoid repumping light assisted photo-associative losses [78]. The 679 nm and 707 nm repumping lasers are switched on for 10 ms to bring the excited state atoms back to the ground state. Finally, a short 20 ms long blue MOT phase is used to detect the their fluorescence. To study the $^1S_0+^3P_0$ collisional process, after the clock pulse, we hold the atoms for variable trapping time in the lattice. After the hold time, the fluorescence of the ground state atoms is detected using a 20 ms long blue MOT phase and the remaining excited state atoms are detected using the same procedure as in $^3P_0+^3P_0$ collisional study. The timing diagram (150 ms wait time for untrapped atoms to fall away is not shown) for the experiments to study both $^1S_0+^3P_0$ and $^3P_0+^3P_0$ collisional processes is shown in figs. 4.1 and 4.2.
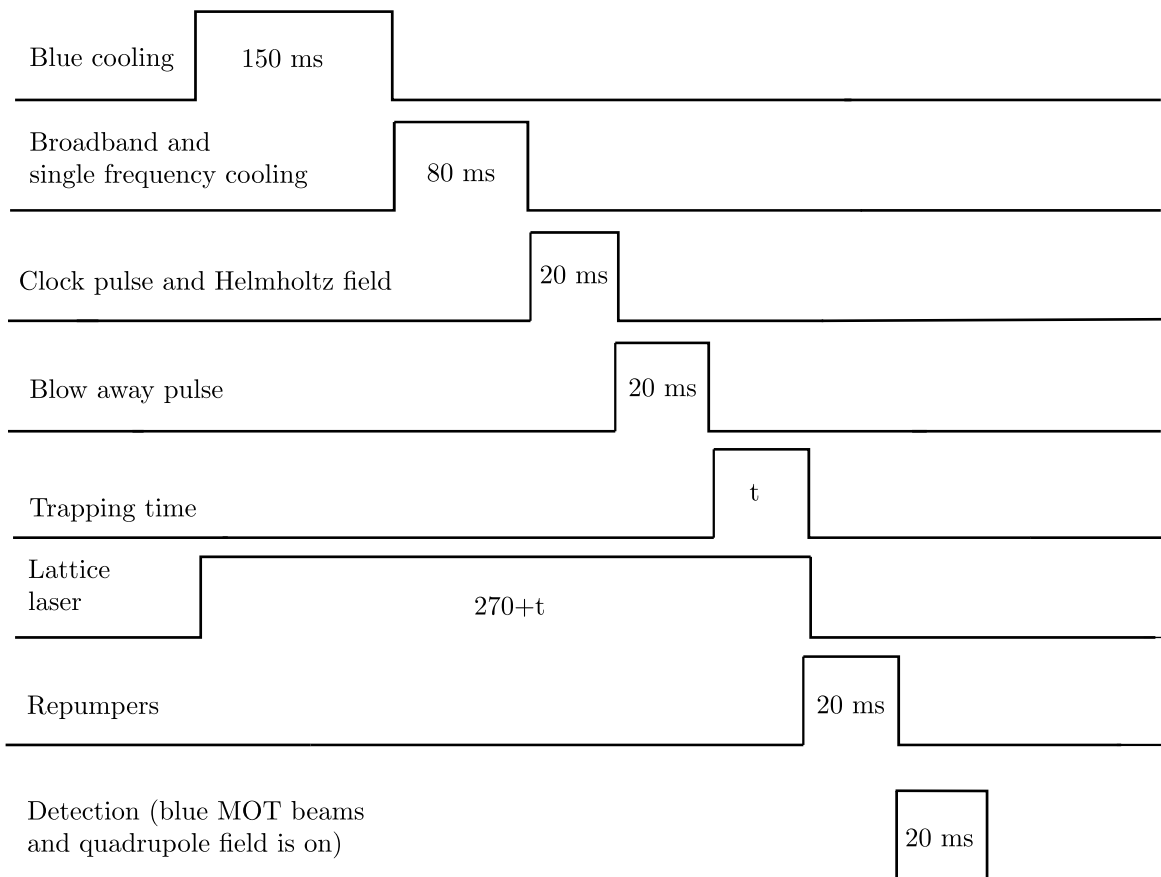
Figure 4.1: Timing diagram to study $^3P_0+^3P_0$ collisions.
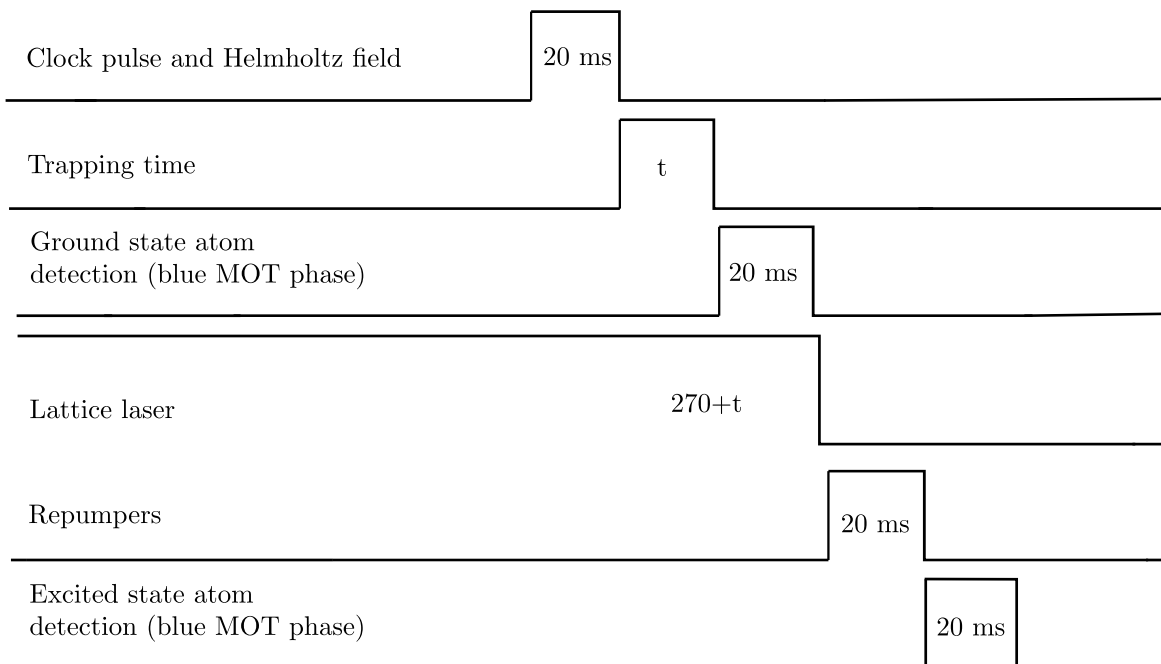
Figure 4.2: Timing diagram to study $^1S_0+^3P_0$ collisions. The cooling and loading sequence is same as that shown in fig. 4.1

In order to model the decay rate of the number of atoms in the trap, we use coupled differential equations

$$\dot{\rho}_g = -\Gamma\rho_g - \gamma_{ge}\rho_e\rho_g \qquad (4.3\text{a})$$

$$\dot{\rho}_e = -\Gamma\rho_e - \gamma_{ge}\rho_e\rho_g - \gamma_{ee}\rho_e^2 \qquad (4.3\text{b})$$

where $\rho_g(\rho_e)$ represents the local atomic density of the ground (excited) state atoms in the optical lattice. Γ is the inverse trap lifetime due to background gas collisions which is 7.5 s. $\gamma_{ee}(\gamma_{ge})$ is the loss coefficient of $^3P_0+^3P_0$ ($^1S_0+^3P_0$) collisions. For, $^3P_0+^3P_0$ collisional losses in which we get rid of ground state atoms immediately after clock pulse, eq. 4.3b reduces to

$$\dot{\rho}_e = -\Gamma\rho_e - \gamma_{ee}\rho_e^2. \qquad (4.4)$$

The rate equation for the $^3P_0+^3P_0$ collisions is given by

$$\dot{N}_e = -\Gamma N_e - \gamma_{ee}\int dr^3\,\rho_e^2$$
$$= -\Gamma N_e - \frac{\gamma_{ee}}{V}N_e^2. \qquad (4.5)$$

In eq. 4.5, N_e is the number of excited state atoms and V is the effective volume of a single lattice site. Solving eq. 4.5 for a single lattice site gives

$$N_e(t) = N_e(0)\frac{e^{-\Gamma t}}{1 + \frac{N_e(0)\gamma_{ee}}{\Gamma\pi^{\frac{3}{2}}w_r^2 w_z}(1 - e^{-\Gamma t})} \qquad (4.6)$$

where $\pi^{\frac{3}{2}}w_r^2 w_z$ is the effective volume of a single lattice site and $N_e(0)$ is the initial atom number. w_r and w_z are the $1/e^2$ radii of the atomic cloud along the radial and axial direction and are related to rms widths as $w_i = 2(w_{\text{rms}})_i$ (see eq. 3.3). Different lattice sites are occupied by different atom numbers and the distribution of atoms along the lattice is a Gaussian distribution with a $1/e^2$ radius w' which is determined from the absorption images. Due to this distribution of atom number, eq. 4.6 is numerically summed over all the lattice sites.

Fig. 4.3 shows the decay of the excited state atom number due to $^3P_0+^3P_0$ collisions for three different initial atom numbers. The solid lines are the fits to the experimental data shown, the fits were obtained by numerical summation of eq. 4.6. From the fits we obtained the loss coefficient $\gamma_{ee} = (4.0 \pm 2.5) \times 10^{-18}\text{m}^3/\text{s}$. The uncertainty in the loss coefficient is due to the uncertainty in the calculation of the radii w_i, w' and the scatter of the fit parameters. Traverso .et al [78] reported the value of γ_{ee} to be an order of magnitude higher that our value by performing measurements in a dipole trap. In the trap, we have $T \sim \hbar\omega_0$ where T is the temperature of the atoms and ω_0 is the axial frequency. In this regime, axial confinement of the particle motion has effect on the scattering rate [80]. Therefore, this difference can be due to the temperature and the dimensionality of the trap potential.
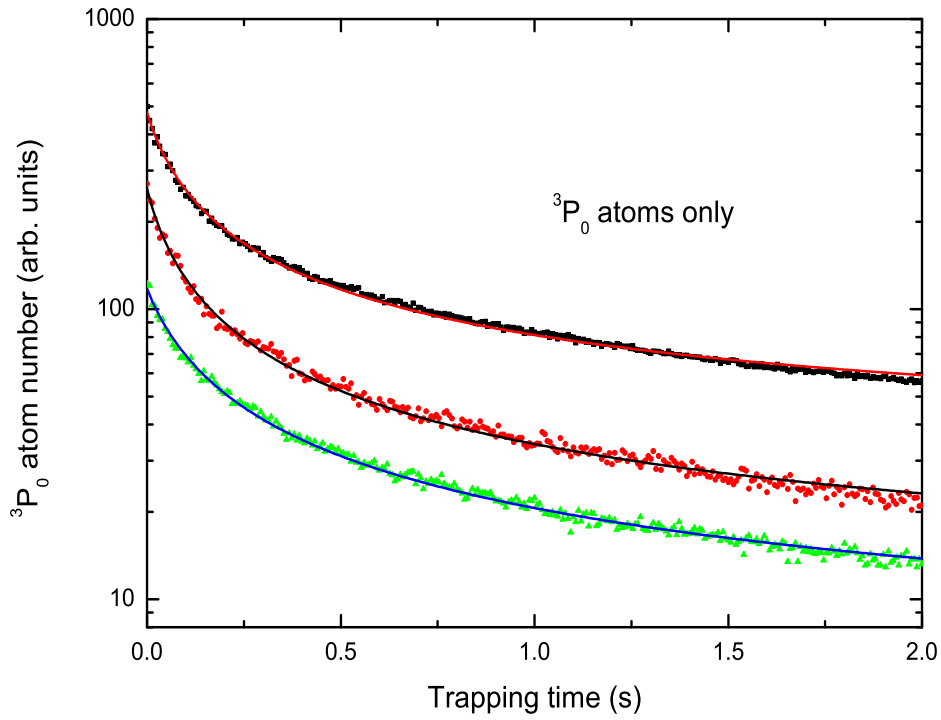
Figure 4.3: Decay of $^3P_0$ atom number due to $^3P_0+^3P_0$ inelastic collisions. The solid lines are fit of summation of eq. 4.6 to the observed decay.
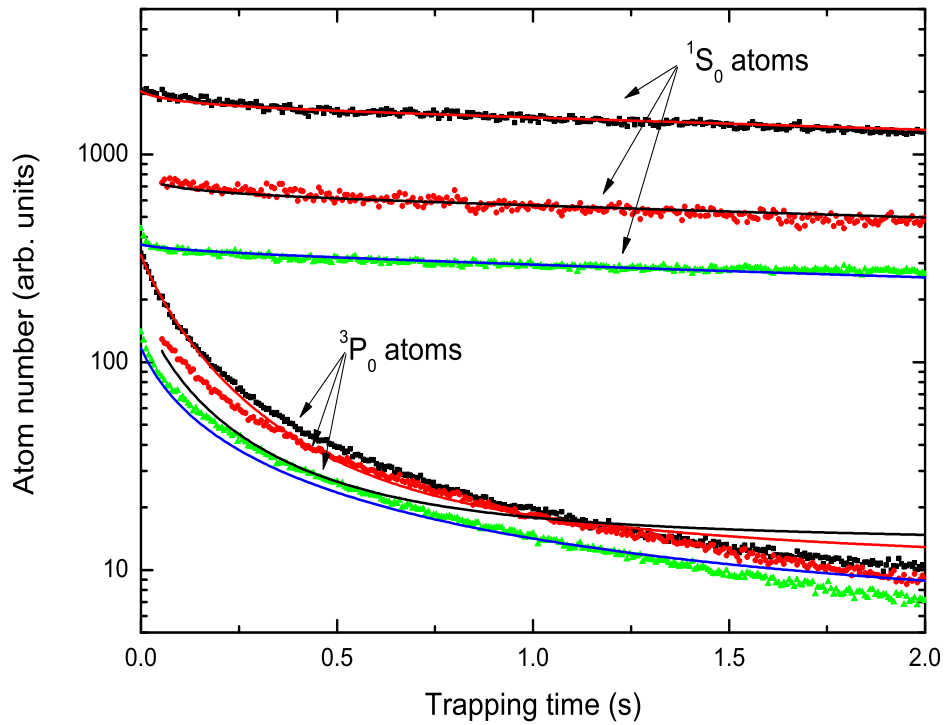
Figure 4.4: Decay of $^3P_0$ and $^1S_0$ atom numbers due to $^1S_0+^3P_0$ inelastic collisions. Fitting is done for ground state atoms.

44
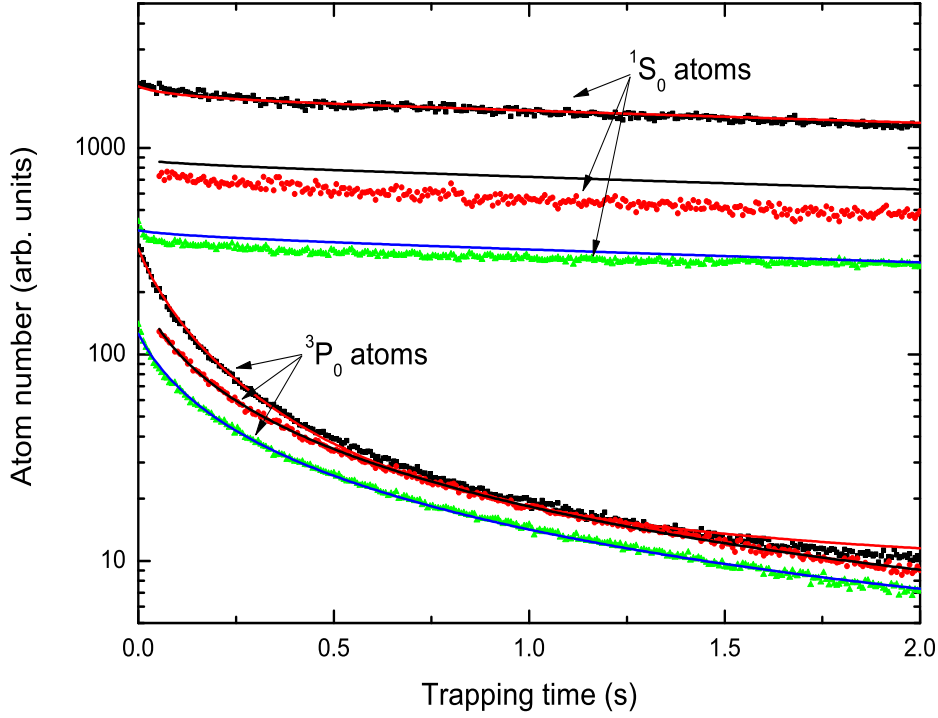
Figure 4.5: Same decay as fig. 4.4 but fitting is done for excited state atoms.

The collisional $^1S_0 + ^3P_0$ losses curves for different initial ground state atoms along with the fits given by the solid lines are shown in figs. 4.4 and 4.5. The simultaneous fitting of eqs. 4.3a and 4.3b to the ground and excited state atoms is made using γ_{ee} obtained from $^3P_0 + ^3P_0$ collisional studies. The fits and the observed decay of atoms show discrepancy depending on whether ground or excited state atoms are fitted.

This discrepancy is attributed to inelastic collisions that reduce the excited state atom number during the ground state atom detection. During the ground state atom detection, the $^1S_0$ atoms are detected using a short blue MOT stage, the atoms which undergo $^1S_0 \rightarrow ^1P_1$ detection are trapped due to the quadrupole field. The scenario is different in case of $^3P_0 + ^3P_0$ collisional study where the atoms are just blown away. Due to the $^1D_2$ leak channel (see fig. 2.1), atoms end up in $^3P_1$ and $^3P_2$ and collision of these atoms with $^3P_0$ atoms could diminish the excited state atom number. However, since the losses are dominated by $^3P_0 + ^3P_0$ collisions, we ignore other types of collisions and correct the excited state population for collisions with $^3P_0$ atoms by calculating the time taken for the ground state atom detection and calculate back the number of $^3P_0$ atoms lost during this detection stage. Fig. 4.6 shows the decay of $^3P_0$ atoms due to both $^3P_0 + ^3P_0$ and $^1S_0 + ^3P_0$ collisions with the corrected fits. The value of $^1S_0 + ^3P_0$ collision loss coefficient $\gamma_{ge} = (5.3 \pm 1.9) \times 10^{-19} \mathrm{m^3/s}$. The uncertainly contributions are same is that for γ_{ee}.

Having determined the loss coefficients γ_{ee} and γ_{eg} we can calculate the inelastic scattering lengths given by eq. 4.2 and they are $\mathrm{Im}(a_{ee}) = (2 \pm 1.2)a_0$ and $\mathrm{Im}(a_{eg}) = (0.26 \pm 0.09)a_0$ where a_0 is the Bohr radius. Using the electronic potential energy curves of Sr_2 given in references [81, 82] an order of magnitude difference between γ_{ee} and γ_{eg}

45
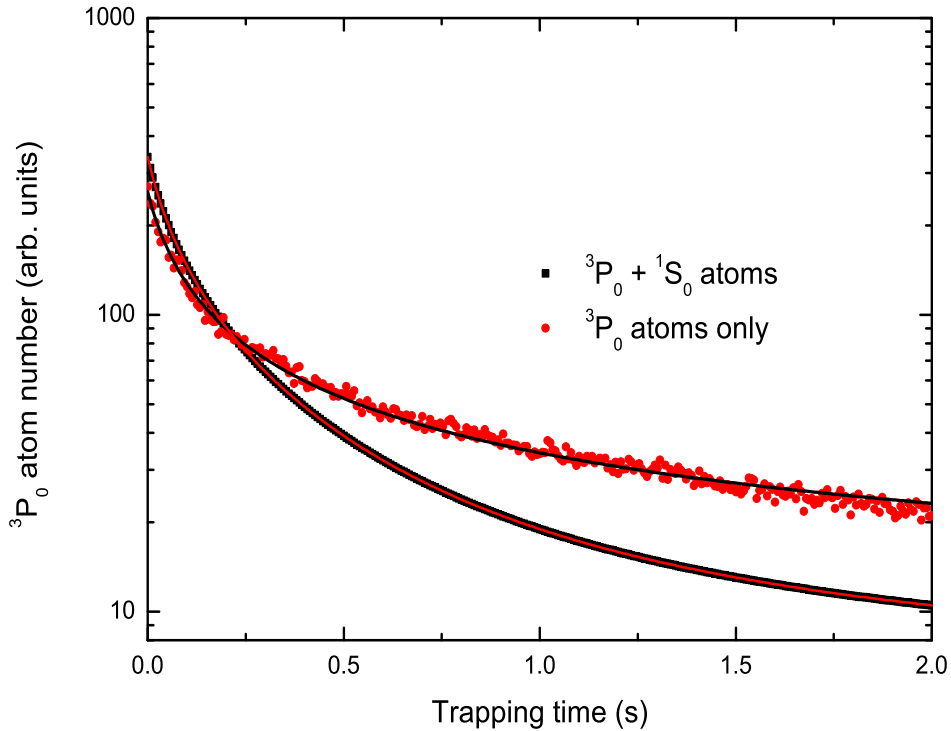
Figure 4.6: Decay of $^3P_0$ atom number due to $^3P_0+^3P_0$ collisions shown by the red circles. The decay due to $^1S_0+^3P_0$ collisions is shown by the black squares.The solid lines are fit obtained by summation of eq. 4.3a and eq. 4.3b.

can be qualitatively explained. The $^3P_0+^3P_0$ asymptote correlates at short internuclear distances to a molecular $^1\Sigma_g^+$ state which can decay to lower states by fluorescence. However, a more likely source of losses are collision-induced nonadiabatic transitions to molecular potentials dissociating to lower asymptotes. For the case of $^1S_0+^3P_0$ collisions, only one potential dissociates to the lower $^1S_0+^1S_0$ asymptote and it is steep at the energy of $^1S_0+^3P_0$ asymptote. Due to selection rules, a direct spontaneous decay to that ground state potential is not allowed but complex coupling to molecular states exists at short internuclear distance that are subjected to spontaneous decay [83].

4.2 Density dependent broadening and decoherence effects of the clock transition

In addition to losses of the atoms from the optical lattice due to inelastic collisions, interactions between atoms also give rise to broadening of the clock transition and decoherence. In case of inelastic collisions, the lifetime of the atom in the excited state is reduced leading to broadening of the transition. In case of elastic collisions, the energy level of atom A is shifted as it approaches another atom. Due to this shift in energy level, the frequency ω of the emitted or absorbed radiation of atom A changes

by an amount $\Delta\omega$. This change $\Delta\omega$ usually depends on the interaction potential between atoms A and B. After the elastic collision, the emitted or absorbed radiation frequency returns to its initial value ω. Therefore, the effect of elastic collision is to induce a phase change, such collisions are also called as "dephasing collisions". In the spectrum of the radiation, these random phase changing collisions lead to a broadening of the transition.

Our case can be approximated by a two-level atom interacting with a classical field. Dynamics of such an atom is represented by the evolution of the density operator which is known as the Schrödinger-von Neumann equation. The equation in the rotating wave approximation is

$$\partial_t \rho = -\frac{i}{\hbar}[H, \rho] \tag{4.7}$$

where the interaction Hamiltonian H and the density matrix ρ are given in the rotating frame. The interaction Hamiltonian and the density matrix for the two-level atom interacting with classical light (the clock laser) are

$$\frac{H}{\hbar} = \begin{pmatrix} 0 & \Omega/2 \\ \Omega/2 & \Delta \end{pmatrix} \tag{4.8}$$

$$\rho = \begin{pmatrix} \rho_{11} & \rho_{12} \\ \rho_{21} & \rho_{12} \end{pmatrix}. \tag{4.9}$$

In eq. 4.8, Δ is the detuning of the clock laser from the clock transition, Ω is the Rabi frequency which is calculated from eq. 2.31. In order to incorporate the decay of populations and decoherences we have to add extra damping matrices to eq. 4.7. First, we write down the losses due to inelastic collisions and decoherences, they are

$$\partial_t \rho_{11} = -(\Gamma + \gamma_{ge}\rho_{22})\rho_{11} \tag{4.10}$$

$$\partial_t \rho_{12} = -\left[\gamma_{ge}\frac{(\rho_{11} + \rho_{22})}{2} + \frac{\gamma_{ee}\rho_{22}}{2} + \Gamma + L + \gamma_{\text{dep}}\rho_{11}\right]\rho_{12} \tag{4.11}$$

$$\partial_t \rho_{21} = -\left[\gamma_{ge}\frac{(\rho_{11} + \rho_{22})}{2} + \frac{\gamma_{ee}\rho_{22}}{2} + \Gamma + L + \gamma_{\text{dep}}\rho_{11}\right]\rho_{21} \tag{4.12}$$

$$\partial_t \rho_{22} = -(\Gamma + \gamma_{ge}\rho_{11} + \gamma_{ee}\rho_{22})\rho_{22}. \tag{4.13}$$

The above set of equations shows how the ground (ρ_{11}), excited state (ρ_{22}) and the coherences (ρ_{12}, ρ_{21}) evolve over time. The ground state atoms decay due to collisions with background atoms (given by Γ) and collisions with excited state atoms (given by $\gamma_{eg}\rho_{22}$). Collisions with background, ground state atoms and excited state atoms are responsible for excited state atom decay. The coherence terms namely ρ_{12} and ρ_{21} decay at a rate $(\Gamma_g + \Gamma_e)/2$ where $\Gamma_g(\Gamma_e)$ are the decay terms of the ground (excited) states. L represents the decoherence due to the linewidth of the clock laser. In order to explain our observed spectra, we had to include an additional dephasing term γ_{dep} which is proportional to the ground state population. Eqs. 4.8 and 4.13 can be combined together to get a master equation [84]

$$\partial_t \rho = -\frac{i}{\hbar}[H, \rho] + \frac{1}{2}\{\Re, \rho\} + \frac{1}{2}(L + \gamma_{\text{dep}}\rho_{11})\mathbf{L}[\sigma_z]\rho \tag{4.14}$$
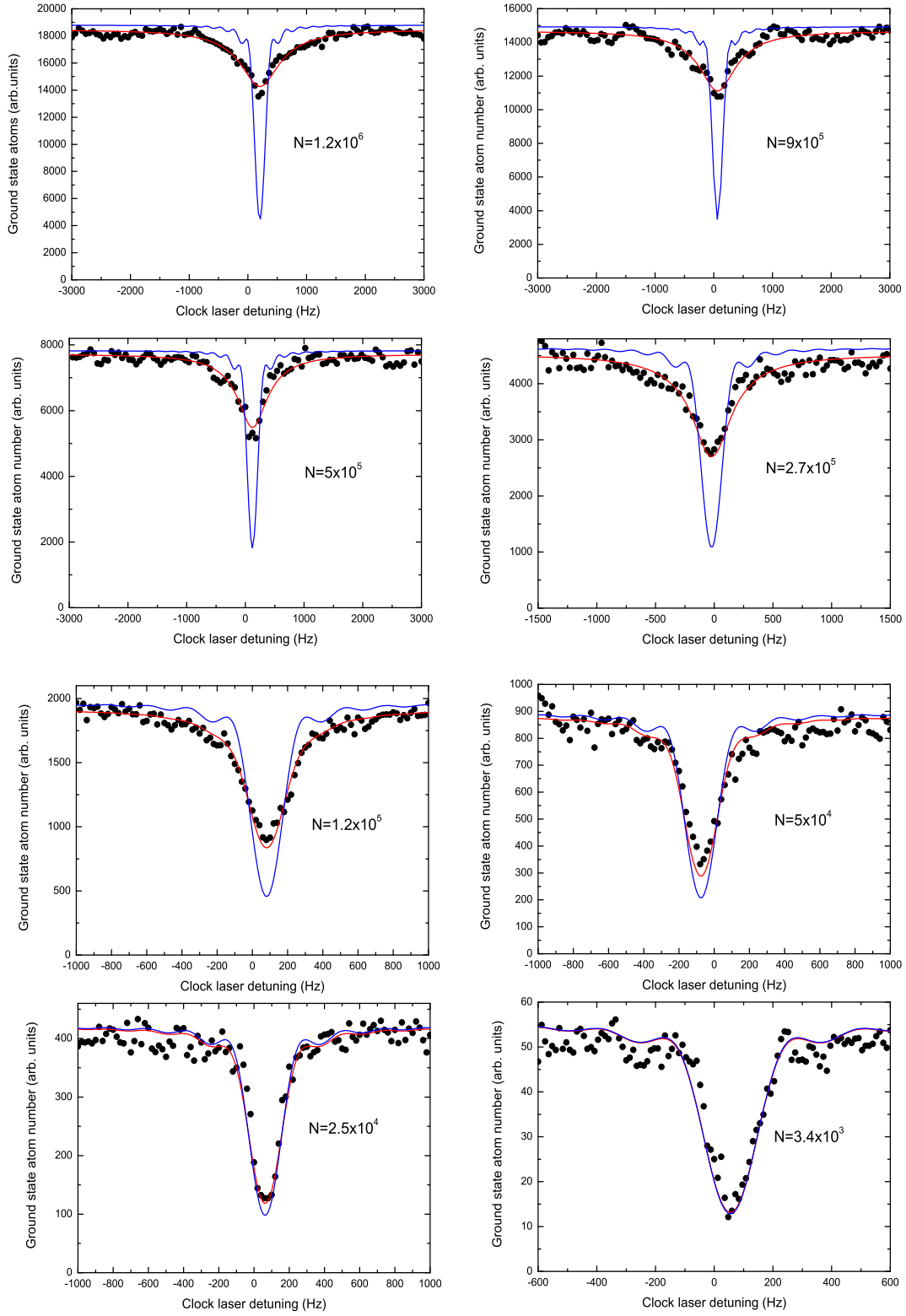
Figure 4.7: Spectra of the clock transition. The red line is the fit of eq. 4.14 with $\gamma_{\mathrm{dep}} = 0$ and the blue line is the fit with $\gamma_{\mathrm{dep}} = (3.2 \pm 1.0) \times 10^{-16}$ m^3/s. The frequency axis have arbitrary offsets.

where the relaxation matrix $\Re$, the Lindblad superoperator $\mathbf{L}[\sigma_z]\rho$ and the Pauli matrix σ_z are given as

$$\Re = \begin{pmatrix} -(\Gamma + \gamma_{ge}\rho_{22}) & 0 \\ 0 & -(\Gamma + \gamma_{ge}\rho_{11} + \gamma_{ee}\rho_{22}) \end{pmatrix} \tag{4.15a}$$

$$\mathbf{L}[\sigma_z]\rho = \sigma_z\rho\sigma_z^\dagger - \frac{1}{2}(\sigma_z^\dagger\sigma_z\rho + \rho\sigma_z^\dagger\sigma_z) \tag{4.15b}$$

$$\sigma_z = \begin{pmatrix} 1 & 0 \\ 0 & -1 \end{pmatrix}. \tag{4.15c}$$

To observe the broadening and dephasing effects due to elastic and inelastic collisions, the number of atoms that were loaded into the optical lattice was varied from 1.2×10^6 to 3.4×10^3. The clock laser intensity with 125 W/cm^2 and a magnetic field of 3 mT were used to excite the atoms from $^1S_0$ to $^3P_0$. The duration of the clock pulse was 5 ms, this value was determined by observing Rabi oscillations at low atom numbers and determining the π pulse time. Fig. 4.7 shows the excitation spectra of clock transition for different atom numbers.

We used eq. 4.14 to fit the observation, the effect of dephasing due to ground state atoms is shown in the figure. The blue line is the fit using eq. 4.14 with $\gamma_{\text{dep}} = 0$. The red line is the fit using the same equation with the γ_{dep} included. From the fits we obtain the value of $\gamma_{\text{dep}} = (3.2 \pm 1.0) \times 10^{-16}$ m^3/s. We can see that at high atom number, the dephasing due to elastic collisions is strong and at low atom number, this dephasing is negligible. The laser linewidth L was fitted to be about 36 Hz. This value is consistent with the clock transition linewidth that is shown in fig. 4.8. The linewidth of the laser was limited due to problems with vibration isolation of the cavity to which the clock laser is stabilized.
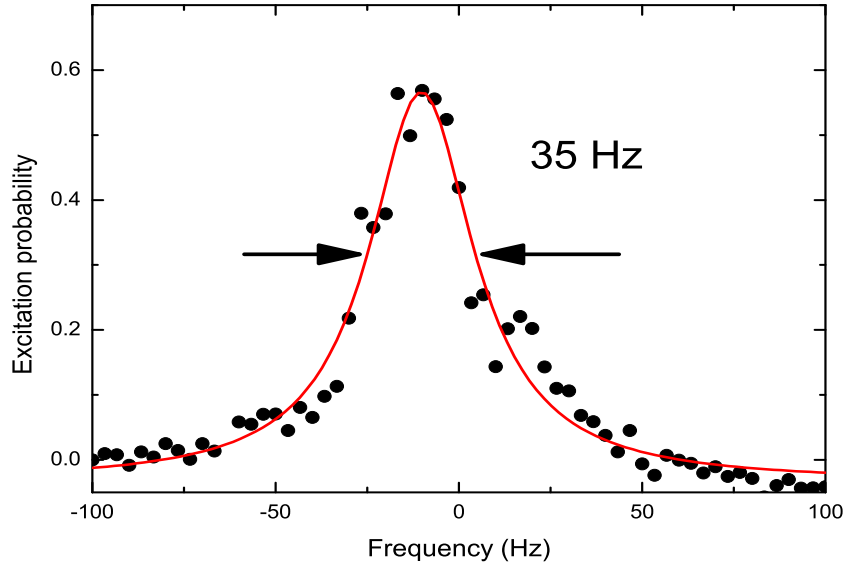
Figure 4.8: Clock transition for a clock pulse length of 35 ms. The Lorentzian fit gives a FWHM 35 Hz.

Fig. 4.9 shows the Rabi oscillations in the clock transition by varying the clock pulse length for two different atom numbers. Rabi oscillations at high atom numbers were not observed due to strong damping. The Rabi frequency calculated from by using eq. 2.31 is $\Omega/2\pi \sim 27$ Hz, the value got from the fit was around 17% smaller than the calculated which could be due to the finite value of the Lamb-Dicke parameter (0.26).
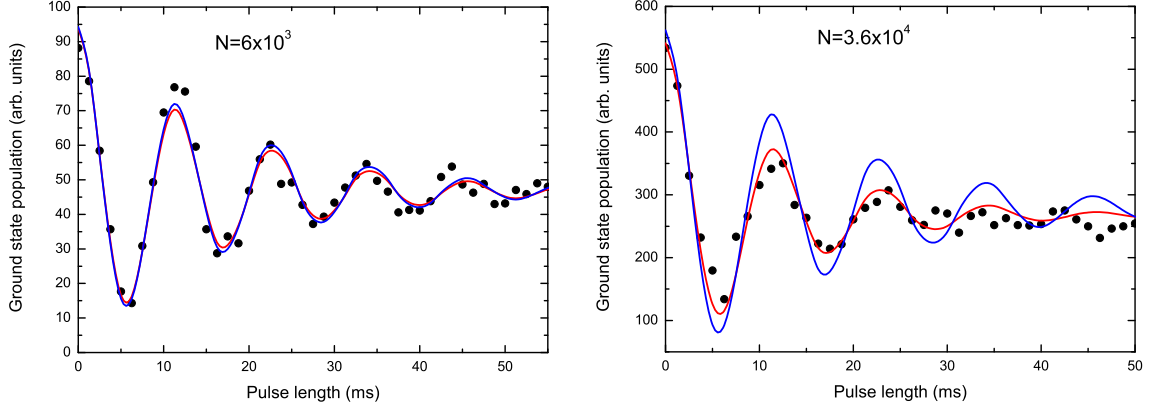
Figure 4.9: Rabi oscillation for two different atom numbers. The red line is the fit of eq. 4.14 with $\gamma_{\mathrm{dep}} = 0$ and the blue line is the fit with $\gamma_{\mathrm{dep}} = (3.2 \pm 1.0) \times 10^{-16}$ m^3/s.

In this chapter, we have quantified inelastic collisions between the clock states of the ^{88}Sr 1-D lattice clock. The observation of clock transition broadening and Rabi oscillations showed an additional dephasing mechanism. One more collision effect, namely the frequency shift of the clock transition will be discussed in the next chapter which describes the method of alternating stabilization that was used to measure the collision frequency shift.

Chapter 5

Measurement of frequency shift using interleaved scheme

This chapter explains the method of interleaved scheme and how it is used to measure the density-dependent frequency shift. Section 5.1 gives a detailed description of the method of locking the clock laser to the $^1S_0 \rightarrow ^3P_0$ transition and possible errors that could limit the accuracy of the measurement. Description of clock frequency shift using mean field interaction and the results are discussed in section 5.2. The chapter concludes with section 5.3 by discussing systematic effects affecting clock frequency and presenting a preliminary uncertainty budget for a 1-D ^{88}Sr lattice clock operating at an uncertainty level of 10^{-16}.

5.1 Locking the clock laser to $^1S_0 \rightarrow ^3P_0$ transition

Perturbations due to interaction with the external environment (e.g: black body radiation, collisions) lead to a shift in the clock transition. In order to improve the performance and accuracy of an optical lattice clock, different frequency shifts to the clock transition due to perturbations should be evaluated and corrected. This requires to systematically vary the perturbation parameter and measure the corresponding frequency shift in the clock transition and extrapolate it to zero shift. To evaluate frequency shifts due to perturbations, an additional frequency reference is needed which is stable over the time of experiment.

However, one can characterize the effects due to perturbations by making a measurement in which the parameter responsible for the perturbation is quickly varied relative to a fixed initial perturbation parameter within a few cycles. This results in interleaved cycles in which the frequency shifts due the two parameters are measured. Such an interleaved scheme offers the advantage of not requiring an external long-term stable frequency reference and can rely on the short term stability of the clock laser. The method was used before to measure the ac Stark shift of the $^1S_0 \rightarrow ^3P_1$ transition of Ca atoms for different wavelengths [85, 86]. In this section, a detailed analysis of this method is presented and it is used to determine the frequency shifts due to collisions.
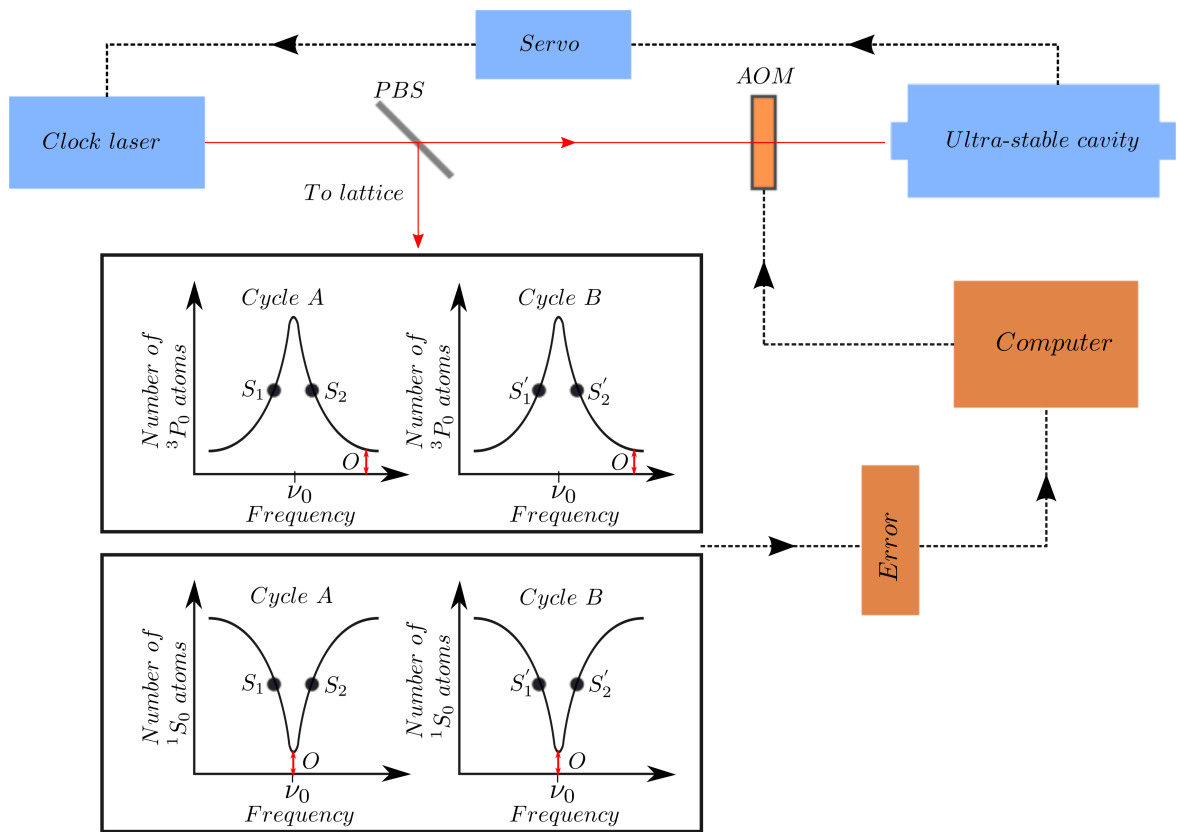
(a) Stabilization of the clock laser to the atoms either to ground state or excited state atoms, O is the offset signal counts. The dotted line is the electronic path.
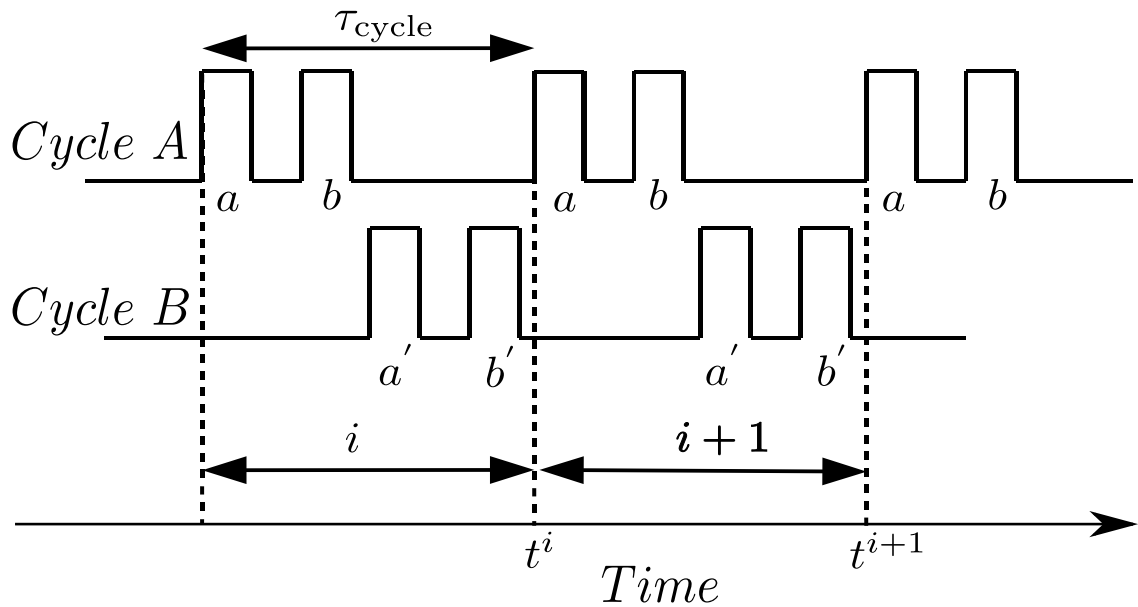
(b) Timing diagram for the interleaved scheme where the perturbation parameter is different in stabilization cycles A and B. Interrogation cycles a, b and a', b' are used to obtain the fluorescence signal counts S_1, S_2 and S_1', S_2' for cycles A and B.

Figure 5.1: Interleaved stabilization scheme.

To measure the density dependent frequency shift, we use interleaved cycles in which the atom number in one cycle is different from the other cycle. When the $^1S_0 \rightarrow {}^3P_0$ transition frequency is different in the two interleaved cycles due to different atom numbers, the frequency of the clock laser that is used to excite the atoms should be different. To observe this, the clock laser is stabilized to the $^1S_0 \rightarrow {}^3P_0$ transition. Fig. 5.1(b) shows the schematic in which the stabilization cycle A (B) has two interrogation cycles a, b (a', b'). Cooling, trapping and probing of the clock transition are done during the interrogation cycles and τ_{cycle} is the time taken for completion of a single (interleaved) cycle i. Fig. 5.1(a) shows the schematic of the clock laser stabilization. In order to lock the clock laser, its frequency is detuned from the $^1S_0 \rightarrow {}^3P_0$ transition frequency ν_0 by about $\pm\delta/2$ where usually $\delta \approx \Delta$ which is the transition linewidth (FWHM) of the $^1S_0 \rightarrow {}^3P_0$ transition. This detuning is done by changing the frequency of the offset AOM between clock laser and the cavity. The atoms are loaded into the lattice and excited to the $^3P_0$ state by applying a clock pulse with a frequency $\nu_0 + \delta/2$. After the excitation, we can detect both the ground and the excited state atoms. The cycle is repeated again with a frequency $\nu_0 - \delta/2$. A deviation ν_{error} of the mean clock laser frequency from ν_0 results in a non-zero difference between the excited state atom numbers probed at $\nu_0 \pm \delta/2$. To estimate ν_{error}, we assume that the clock transition has a Lorentzian profile. If the atom number at detunings $\nu_0 + \delta/2$ and $\nu_0 - \delta/2$ are given by the fluorescence signals S_1 and S_2 respectively, then relation between ν_{error} and the fluorescence signal is

$$\nu_{\mathrm{error}} = \pm\kappa\delta\frac{S_2 - S_1}{2(S_2 + S_1 - 2 \cdot O)}. \tag{5.1}$$

In eq. 5.1 the plus sign is used in the estimated frequency error when ground state atoms are detected and minus sign is used in the estimated frequency error when the excited state atoms are detected. In our experiment we only detect the excited state atoms in order to reduce the interrogation time. The offset signal O is determined as shown in fig. 5.1(a). We give the value of δ and the offset signal O as the input parameter in the measurement program for the correction. κ is a function of detuning and it is equal to 1 when the atoms are probed at FWHM points. Instead of probing atoms at FWHM points, one can probe at different detunings δ. For example, to probe different atom numbers with the same excitation probability, we use detunings δ different from Δ (FWHM) which would result in different values of κ for the cycles A and B. κ in this case is given as

$$\kappa = \frac{1}{4\mu}(\mu^2 + 1)^2 \tag{5.2}$$

where $\mu = \frac{\delta}{\Delta}$. The different values of κ was compensated by having different gain values G in cycles A and B.

The estimated frequency error ν_{error} is obtained independently for the two stabilization cycles and is fed back with an appropriate gain G smaller than one to the clock laser-cavity offset AOM ν^i_{offset}, via the measurement program in order to keep the laser locked at the clock transition frequency for the two cycles. This gain factor G introduces an effective time constant for the servo loop. The stabilization of the

clock laser to the $^1S_0 \to \, ^3P_0$ transition becomes slightly complicated due to the change in length of the ultra-stable cavity, resulting in a drift of the frequency of the clock laser. Since this frequency drift of the laser is roughly linear in time, an estimated correction for this drift D is sent as feed forward to the offset AOM between the clock laser and its reference cavity. To explain this drift correction more clearly, consider the stabilization cycle A in the cycle i (fig. 5.1(b)). The drift correction D^i is done at the start of the interrogation cycle a and b. At the end of cycle b, ν^i_{error} is estimated and ν^i_{offset} is corrected for the drift during a' and b' of stabilization cycle B. The drift rate is automatically updated to a new value D^{i+1} by adding to the previous drift rate D^i, a correction proportional to ν_{error}. The correction of the frequency offset between clock laser and its reference cavity and the update of the drift rate are given as

$$\nu^{i+1}_{\text{offset}} = \nu^i_{\text{offset}} - G \cdot \nu^i_{\text{error}} + \tau_{\text{cycle}} \cdot D^i \tag{5.3}$$

$$D^{i+1} = D^i + \frac{\beta \cdot \nu^i_{\text{error}}}{\tau_{\text{cycle}}}. \tag{5.4}$$

5.1.1 Time constants and locking errors in a single cycle

First, we assume zero drift of the reference cavity and noiseless detection. If t^i is the time in cycle i, the error signal ν^i_{error} is then reduced as

$$\nu^i_{\text{error}} = \nu^0_{\text{error}} \cdot (1 - G)^{\frac{t^i}{\tau_{\text{cycle}}}} \tag{5.5}$$

where the ν^0_{error} is the initial error at $t^0 = 0$. Comparing ν^i_{error} with $\nu^0_{\text{error}} \, e^{\frac{-t^i}{\tau_{\text{servo}}}}$, we get the time constant τ_{servo} of the servo loop as

$$\tau_{\text{servo}} = \frac{-\tau_{\text{cycle}}}{\ln(1 - G)}. \tag{5.6}$$

For our interleaved cycles to measure the density shift, the gain value was $G = 0.5$ and $\tau_{\text{cycle}} \sim 0.8$ s giving $\tau_{\text{servo}} \sim 1.2$ s.

In practice however, the cavity resonance drifts which leads to change in the clock laser frequency. If the resonance frequency of the cavity ν_{cavity} drifts at a constant rate $\dot{\nu}_{\text{cavity}}$ and no drift correction is applied, there will be a steady frequency offset error in the measurement cycle. For example, consider cycle i in the stabilization cycle A shown in fig. 5.1(b). The error ν^i_{error} is estimated at the end of b and after correction the remaining error is $\nu^i_{\text{error}} \cdot (1 - G)$. At the end of cycle B, the error corrected in cycle i for A would have increased by $\dot{\nu}_{\text{cavity}} \cdot \tau_{\text{cycle}}$. The error in the cycle $i + 1$ is related to the error in cycle i as

$$\nu^{i+1}_{\text{error}} = \nu^i_{\text{error}} \cdot (1 - G) + \dot{\nu}_{\text{cavity}} \cdot \tau_{\text{cycle}}. \tag{5.7}$$

The error after some time, in the absence of drift correction, can be found from the steady state solution of eq. 5.7 which is

$$\nu^{\text{drift}}_{\text{error}} = \frac{\dot{\nu}_{\text{cavity}} \cdot \tau_{\text{cycle}}}{G}. \tag{5.8}$$
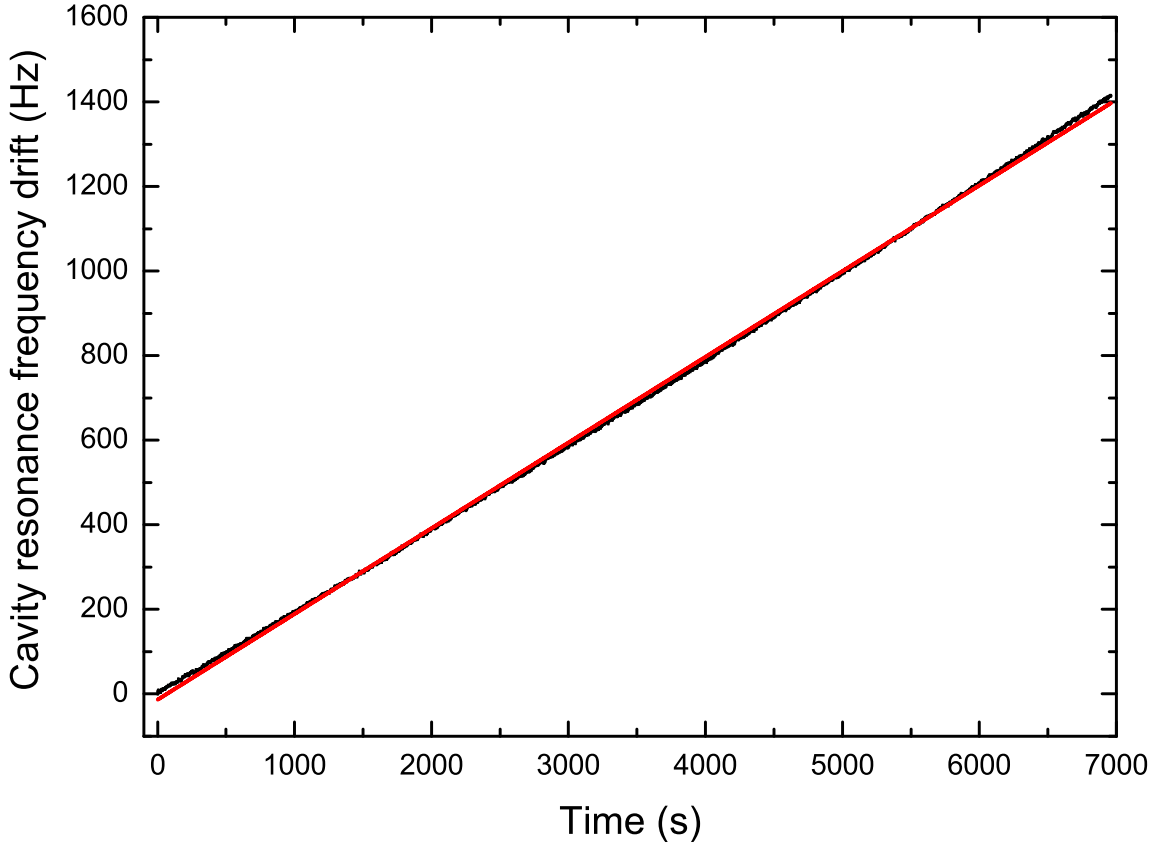
Figure 5.2: Variation of cavity resonance frequency with time. Red line is a linear fit to the drift of the cavity resonance frequency.

Fig. 5.2 shows the drift of the cavity resonance frequency over time, a linear fit to the drift gives us the drift rate D to be ~ 0.2 Hz/s. Using this drift rate in eq. 5.8, we get $\nu_{\text{error}}^{\text{drift}} \sim 0.3$ Hz. This error would limit the accuracy of a frequency measurement to 0.3 Hz/$\nu_0 \sim 7 \times 10^{-16}$ where ν_0 is the clock transition frequency. In practice, we give an estimate of the drift rate as an input parameter and correct the cavity drift rate through feed forward as shown in eq. 5.4 assuming the drift rate to be constant. However, during the course of the experiment, the drift rate changes to a new value due to some external disturbances. Assume that at $t^0 = 0$, the initial drift rate D^{initial} suddenly changes to $\dot{\nu}_{\text{cavity}}^{\text{new}}$. If we assume that the time taken for the drift rate to change to the new value is long compared to the time taken for the error signal to reach steady state value, we end up with a steady offset error $\nu_{\text{error}}^{\text{steady}} = \frac{a \cdot \tau_{\text{cycle}}}{G}$ where $a = \dot{\nu}_{\text{cavity}}^{\text{new}} - D^i$. Updated drift rate at time t^i is similar to the exponential approach of ν_{error}^i towards zero (eq. 5.5) and it is modelled with a time constant τ_{drift} as

$$D(t) = D^{\text{initial}} + a \cdot (1 - e^{\frac{-t^i}{\tau_{\text{drift}}}}). \tag{5.9}$$

Comparing eqs. 5.9 and 5.4 after one cycle ($t^i = \tau_{\text{cycle}}$) for the case of steady state error we get τ_{drift} as

$$\tau_{\text{drift}} = \frac{-\tau_{\text{cycle}}}{\ln(1 - \frac{\beta}{G})}. \tag{5.10}$$

In our case, for a drift rate gain $\beta = 0.005$, the final value $\dot{\nu}_{\text{cavity}}^{\text{new}}$ is approached with a time constant $\tau_{\text{drift}} \sim 80$ s.
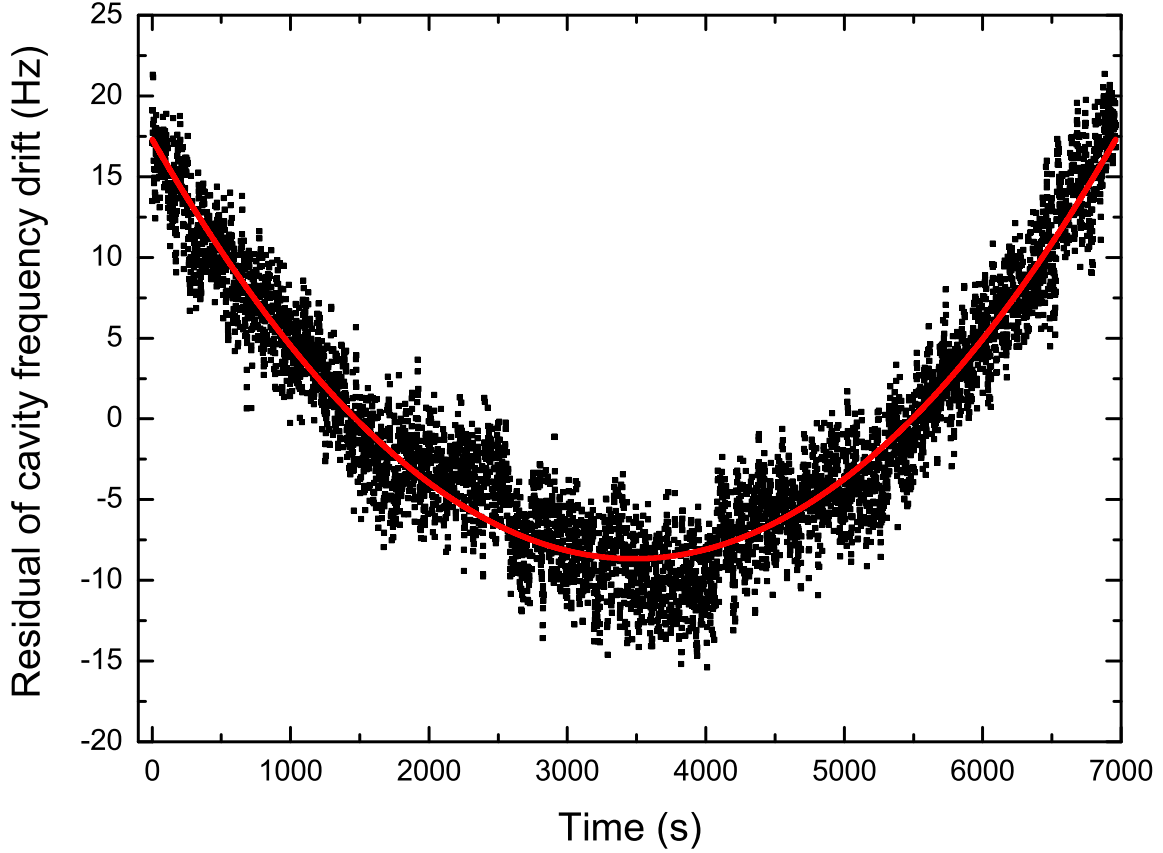
Figure 5.3: Residuals from the linear fit shown in fig. 5.2, red line shows a 2$^{\text{nd}}$ order polynomial fit. The rate of change of drift rate $\ddot{\nu}_{\text{cavity}}$ calculated from the fit is 2×10^{-6} Hz/s^2.

Eq. 5.10 assumes that the drift rate changes suddenly from an initial value to a final value. Over a long period of time, we observe deviation from the linear behavior of the drift that might lead to frequency errors. This deviation are the residuals from the linear fit in fig. 5.2 and is shown in fig. 5.3. This change in drift rate could be attributed to temperature changes in the cavity. A second order polynomial fit gives us the rate of change of the drift rate $\ddot{\nu}_{\text{cavity}} = 2 \times 10^{-6}$ Hz/s^2. This change in drift rate would introduce a constant offset error due to the finite time required to update the drift. If d^0 is the initial drift rate of the cavity, after cycle i, the drift rate is

$$d_i = d^0 + i \cdot \ddot{\nu}_{\text{cavity}} \tau_{\text{cycle}}. \tag{5.11}$$

Let the estimated drift rate at the measurement cycle i be D^i, then the error between actual drift rate and the updated drift rate is

$$\epsilon^i = d^0 + i \cdot \ddot{\nu}_{\text{cavity}} \tau_{\text{cycle}} - D^i. \tag{5.12}$$
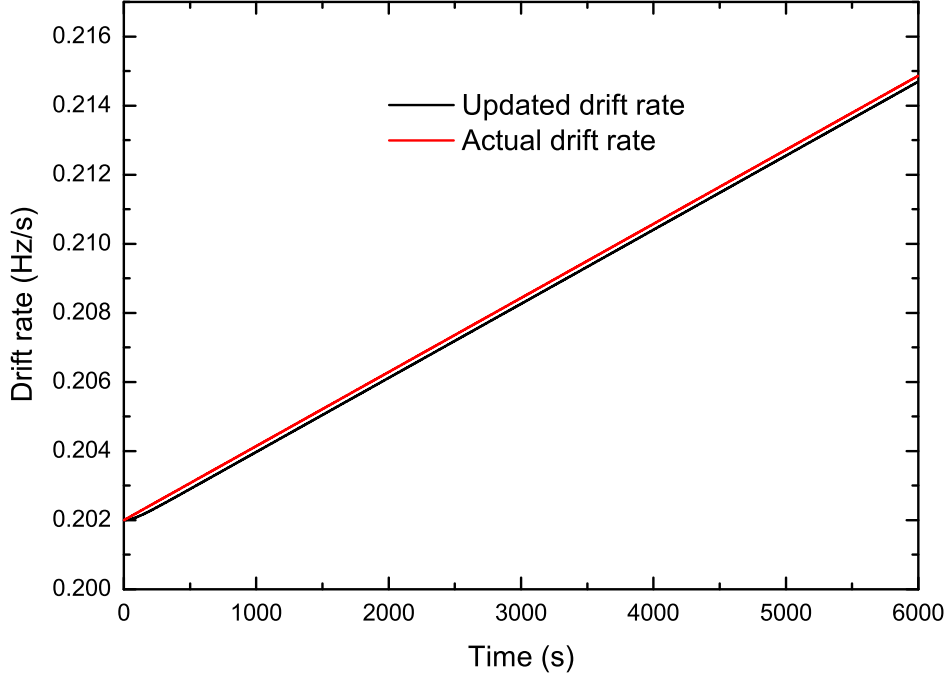
Figure 5.4: Simulation of eqs. 5.11 and 5.14. Due to finite time taken for the drift rate update, the actual drift rate is larger than the updated drift rate.

The steady state offset error, if the time taken for the drift rate to change is long compared to the time taken for the error signal to reach a steady state value and the drift update for the $i + 1$ measurement are

$$\nu_{\text{error}}^{\text{steady}} = \frac{\epsilon^i \cdot \tau_{\text{cycle}}}{G} \tag{5.13}$$

$$D^{i+1} = D^i + \frac{\beta}{G} \nu_{\text{error}}^{\text{steady}}. \tag{5.14}$$

Fig. 5.4 shows the simulation of eqs. 5.11 and 5.14. At long times, the difference between the updated and the actual drift rates settle to a constant value. This steady state drift rate error $\epsilon_{\text{error}}^{\text{steady}}$ which can be obtained by using $\epsilon^i = \epsilon^{i+1}$ is

$$\epsilon_{\text{error}}^{\text{steady}} = \ddot{\nu}_{\text{cavity}} \, \tau_{\text{cycle}} \left(\frac{G}{\beta} - 1 \right). \tag{5.15}$$

The steady state drift rate error is estimated to be ~ 0.15 mHz/s for our parameters. This drift rate error would result in $\nu_{\text{error}}^{\text{steady}} \sim 0.25$ mHz which would limit the relative accuracy of the clock transition to $\sim 5 \times 10^{-19}$.

5.1.2 Interleaved cycles

Fig. 5.1 shows the interleaving of the stabilization cycles A and B. We read out the frequency values of the the offset AOM between the clock laser and its reference cavity for A and B at the end of cycle i. The frequency shift due to collisions is obtained from the difference between the frequency values of the offset AOM of the two cycles A and B. Though the cavity drift is corrected in each individual cycle, due to reading the locked signal values of A and B at different times a constant frequency offset is present which can be estimated as $\frac{\dot{\nu}_{\text{cavity}} \cdot \tau_{\text{cycle}}}{2}$. This constant frequency offset is around few tens of milli-Hertz in our case. However, this offset can be can be eliminated by taking the average of the locked signal in i and $i + 1$ of one cycle and subtracting it with the locked signal taken in measurement cycle i of the other cycle.

Equal time for interrogation cycles a, b, a', b' ensures that any disturbances which are introduced by the cycle timing are equal and therefore cancel when the difference between the stabilization cycles are taken. Possible disturbances can be detected by differences in atom number or temperatures in cycles a (a') and b (b'). In our experiment, atom number and thus the density had to be different in measurement cycles A and B, this was done by having different blue MOT loading times in cycles A and B. However, in the cycle pairs (a,b) and (a',b') which is used to lock the clock laser to the atoms, the atom number should be same. Initially we observed that there was a difference between the atom numbers in cycles a (a') and b (b'). The problem was traced to the switching of quadrupole field gradient when the blue MOT cycle ended and the red MOT cycle started. Due to the change in the field gradient (change in the current flowing through the coils), vibrations were induced in the coils. The vibration induced by the previous cycle MOT switching displaced the zero point of the quadrupole field gradient and influenced the red MOT position and therefore the loading of the atoms from the red MOT to the optical lattice in the following interrogation cycle.
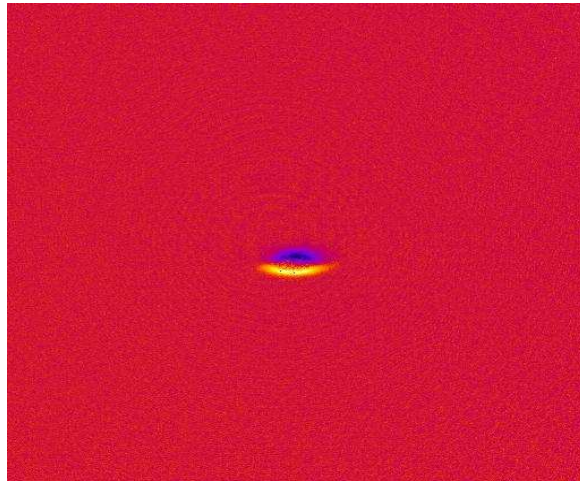
Figure 5.5: Difference of the red MOT absorption images taken in cycle a and b for same cycle time in both interrogation cycles.

Fig. 5.5 shows the difference of the red MOT absorption images taken in cycles a and b. The yellow region, which is the non-overlapping part between the red MOT of loading cycle a and b clearly indicates that the red MOT position is different in interrogation cycles. The vibrations continued from one cycle to another and damped. In order to overcome this problem, a darktime was added at the beginning of each loading cycle. We made the cycle times same for both stabilization cycles A and B so that the displacement of the atoms in the cycles a, b, a' and b' is the same. In our measurement program, we had $(darktime - blue\ MOT\ loading\ time) + blue\ MOT\ loading\ time$. This allowed to change our atom numbers in interleaved cycles by changing the blue MOT loading time while keeping the cycle times constant.

(a)

(b)
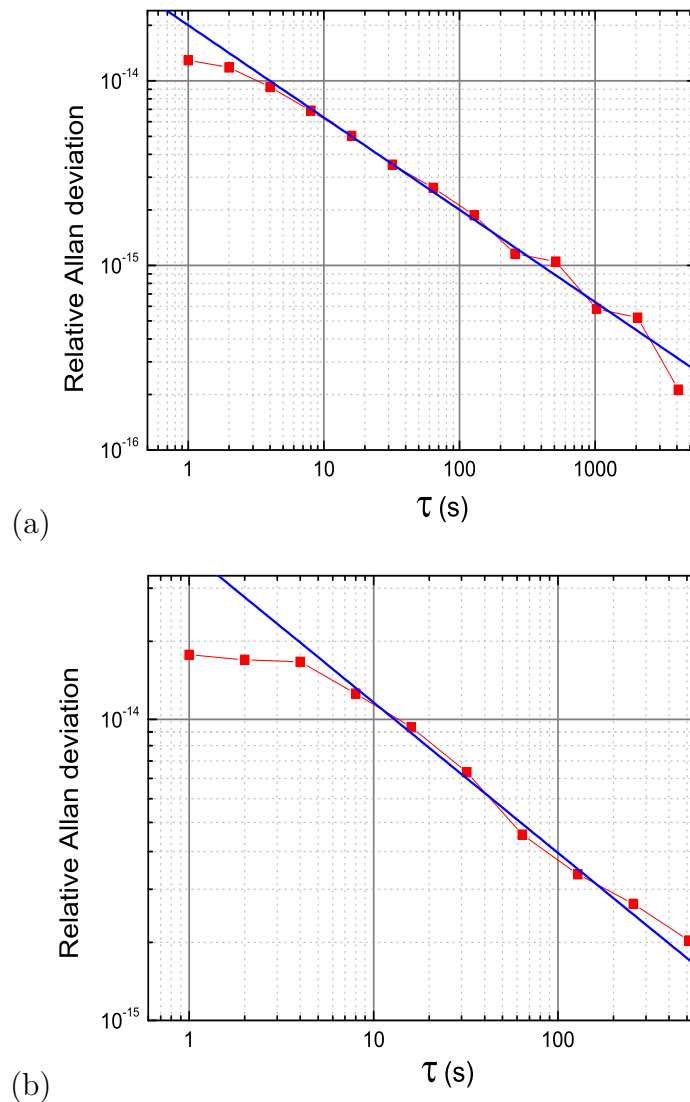
Figure 5.6: Squares show the Allan deviation (with respect to the clock transition frequency). (a) With identical parameters (atom number) for both cycles. (b) With different parameters (atom number).

To check if there is any systematic frequency offset present when the atom number is same in both cycles, around 2×10^4 atoms were loaded into the lattice for both stabilization cycles. Each of the interrogation cycles (a, b, a', b') were ~ 200 ms long. Fig. 5.6 (a) show the stability (given by the Allan deviation) of the difference between the clock laser frequencies of cycles A and B with respect to the clock transition frequency. After an averaging time of $\tau \sim 8$ s, the Allan deviation scaled down as $1/\sqrt{\tau}$ (white noise limited) which is shown by the blue line. We reached a fractional stability of 2×10^{-16} in $\tau = 4000$ s. This test revealed no systematic offset between the cycles. We loaded different number of atoms in the interleaved cycles by having different blue MOT loading times. For the density shift measurement, the atom number in cycle B was fixed to 9.7×10^3 and the atom number in cycle A was varied till 9×10^4. Fig. 5.6(b) shows the relative Allan deviation for one such measurement with atom number 5.6×10^4 in cycle A and 9.7×10^3 atoms in cycle B. We reached a stability of 2×10^{-15} after an averaging time of 500 s. The uncertainty of the measured frequency shift is got from the Allan deviation. The difference in the stability at a given averaging time for the two measurements shown in fig. 5.6 could be attributed to noise levels in the experiment since they were taken on different days.
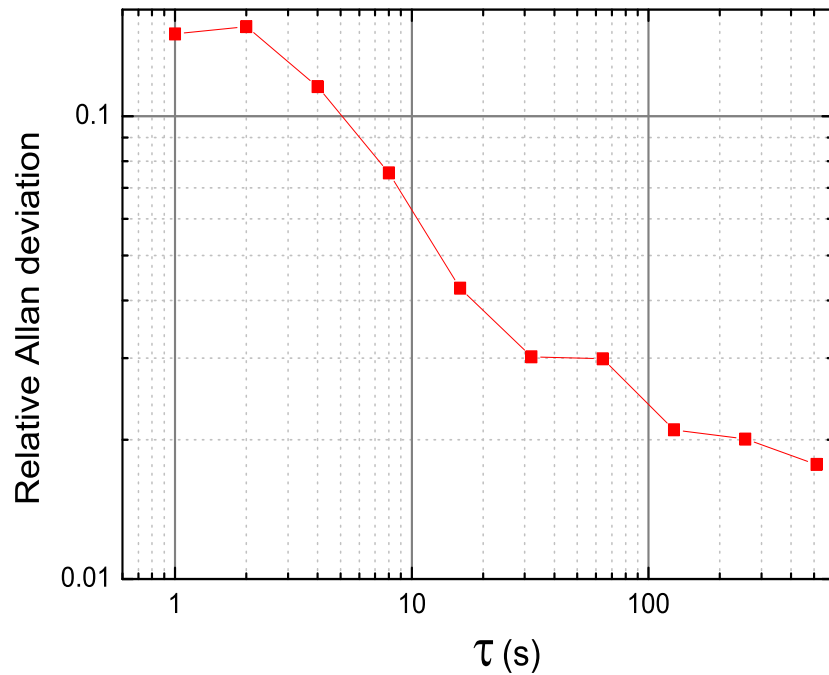
Figure 5.7: Relative Allan deviation of the atom number obtained from the fluorescence signal counts S.

Signal-to-noise problem caused by shot-to-shot atom number fluctuation will limit the stability of a clock operation (see eq. 1.1). In order to characterize the relative stability, we calculate the excited atom number at lock points $\nu_0 + \delta/2$ and $\nu_0 - \delta/2$ which are given by the fluorescence signals S_1, S_2, S_1', S_2' and find its relative Allan deviation. The stability shown in fig. 5.7 is with respect to the average excited state

atoms at lock points in a single cycle. The atom number can be determined better than 2% after an averaging time $\tau \sim 500$ s. We find that the atom number fluctuation in our experiment will limit the uncertainty of the measured density shift (explained in the next section) with respect to clock transition to $\sim 8 \times 10^{-16}$ for an averaging time of $\tau \sim 500$ s. The difference between the estimated stability due to atom number fluctuation and the stability shown in fig. 5.6(b) could be attributed to Dick effect which results from sequential probing of atoms [87, 88].

Consider a two level atom in a superposition state $|\psi\rangle = \alpha |g\rangle + \beta |e\rangle$. When a measurement is made, probability of finding the atom in the ground (excited) state is $|\alpha|^2 (|\beta|^2)$. This probabilistic outcome is the source of quantum projection noise and it sets the fundamental limit to the instability of the atomic frequency standard. If the number of atoms that are being probed is N and p is the excitation fraction, for Rabi spectroscopy and Lorentzian lineshape of the transition, the quantum projection noise limited instability for an averaging time τ is given as [63]

$$\sigma_y(\tau) = \frac{\Delta}{2\nu_0} \sqrt{\frac{2(1-p)}{pN} \frac{T_c}{\tau}} \qquad (5.16)$$

where Δ is the linewidth (FWHM) of the transition, ν_0 is the clock transition and T_c is the total time taken to probe the atoms at both half maxima points and the signal to noise (S/N) of the excited state population is given as $\sqrt{pN/(1-p)}$. Using this relation, we can estimate the quantum projection noise limited stability. The density shift measurements were carried out by having an excitation probability of 35% and typical linewidth of 200 Hz. For 5×10^4 atoms probed, the quantum projection noise limited instability at 1 s is $\sigma_y(1\,\text{s}) \sim 2 \times 10^{-15}$ (T_c being 0.4 s).

5.2 Density dependent frequency shift of clock transition

At ultra-cold temperatures where only s-wave collisions occur, the atoms, due to elastic collisions, undergo shift in their energy levels. In a uniform gas with atoms of mass being m, this shift can be calculated by considering the mean field interaction and it is $g(4\pi\hbar^2/m)a\,n$, where g is the two-particle correlation function at zero separation, a is the scattering length, n is the atom density. Let $|g\rangle$ and $|e\rangle$ be the ground and excited states of the clock transition. In a mixture of ground and excited state atoms, the shift in the energy are given as [89]

$$\delta E_g = \frac{4\pi\hbar^2}{m}(g_{gg}a_{gg}\rho_g + g_{ge}a_{ge}\rho_e) \qquad (5.17a)$$

$$\delta E_e = \frac{4\pi\hbar^2}{m}(g_{ee}a_{ee}\rho_e + g_{ge}a_{ge}\rho_g) \qquad (5.17b)$$

where $E_g(E_e)$ is the shift in the ground (excited) state energy, a_{ij} is the scattering length between atoms in the internal states i and j and $\rho_g(\rho_e)$ is the atom number density for ground (excited) state. The two-particle correlation function at zero separation

g_{ij} which measures the probability that two particles are simultaneously detected at the same position and time is given by the expectation value of field operators [90]

$$g_{ij} = \frac{\left\langle \hat{\Psi}_i^\dagger \hat{\Psi}_j^\dagger \hat{\Psi}_i \hat{\Psi}_j \right\rangle}{\left\langle \hat{\Psi}_i^\dagger \hat{\Psi}_i \right\rangle \left\langle \hat{\Psi}_j^\dagger \hat{\Psi}_j \right\rangle}. \tag{5.18}$$

The shift in the transition frequency $\delta\nu_{eg}$ between $|g\rangle$ and $|e\rangle$ is

$$\frac{\delta E_e - \delta E_g}{h} = \delta\nu = \frac{\hbar}{m} \rho \left[g_{ee}a_{ee} - g_{gg}a_{gg} + \zeta(2g_{ge}a_{ge} - g_{gg}a_{gg} - g_{ee}a_{ee}) \right] \tag{5.19}$$

where $\rho = \rho_g + \rho_e$ and $\zeta = (\rho_g - \rho_e)/\rho = 1 - 2P_e$, P_e being the excitation probability. For ultracold bosons (non-condensed), due to exchange symmetry, we have $g_{gg} = g_{ee} = 2$. Consider two atoms initially in ground state, for a coherent homogeneous excitation, the wavefunctions (expressed as coherent superposition of ground and excited states) of both atoms are identical (indistinguishable) and therefore maintain exchange symmetry, g_{ge} in this case is 2. However, depending on the temperature of the atoms or the alignment between the clock laser beam and the lattice, atoms evolve with different Rabi frequencies [91]. Thus the excitation is not homogeneous and the atoms are no longer indistinguishable. During the Rabi pulse, g_{ge} depends on the degree of inhomogeneity and varies with time, therefore we have have for bosons [92] $1 \leq g_{ge}(t) < 2$. In addition to variation of g_{ge}, ground and excited state population also evolve over time during Rabi pulse. The evolution of atoms in our case is described by eq. 4.13 but for simplicity, we assume the atomic evolution without damping which is a good approximation for time scales and densities considered here (see fig. 4.9). If the laser is detuned by an amount Δ from the clock transition, the excitation probability varies with time as

$$P_e(t) = K \frac{\Omega^2}{\overline{\Omega}^2} \sin^2\left(\frac{\overline{\Omega}\, t}{2}\right) \tag{5.20}$$

where Ω ($\overline{\Omega}$) is the Rabi (generalized Rabi) frequency. The relation between the two is given as $\overline{\Omega} = \sqrt{\Omega^2 + \Delta^2}$. The value K takes into account the decoherence effects (like atom temperature) that limits excitation probability when the atoms are probed at resonance ($\Omega = \overline{\Omega}$).

The value of the frequency shift over a Rabi pulse length t_R that is measured in the experiment can therefore be calculated as

$$\overline{\delta\nu} = \int_0^{t_R} g(t)\, \delta\nu(t)\, dt \tag{5.21}$$

where $g(t)$ is the normalized sensitivity function [93] that describes how the clock laser frequency fluctuations are weighted during the pulse length. For a constant pulse length $t_R = 5$ ms, the excitation probability depends on the detuning Δ. By making the approximation $g_{ge}(t) = 1$, eq. 5.21 can be written as

$$\overline{\delta\nu} = \frac{2\hbar}{m} \rho \left[a_{ee} - a_{gg} + C(a_{ge} - a_{gg} - a_{ee}) \right] \tag{5.22}$$

with

$$C = \int_0^{t_R} g(t) \left\{ 1 - 2 P_e(t) \right\} dt = \int_0^{t_R} g(t) \left\{ 1 - 2 K \frac{\Omega^2}{\overline{\Omega}^2} \sin^2 \left(\frac{\overline{\Omega} t}{2} \right) \right\} dt. \quad (5.23)$$

For given values of K and Ω, both determined by observing Rabi oscillations, C can be numerically calculated for a given detuning independent of the density. For a constant value of C, $\overline{\delta\nu}$ is proportional to the atom density. To determine the coefficient of the shift, interleaved scheme was used and the coefficient of the density shift was determined from the slope of the plot $(\overline{\delta\nu})_A - (\overline{\delta\nu})_B = \epsilon(\rho_A - \rho_B)$, where $\epsilon = \frac{2\hbar}{m} \left[a_{ee} - a_{gg} + C(a_{ge} - a_{gg} - a_{ee}) \right]$
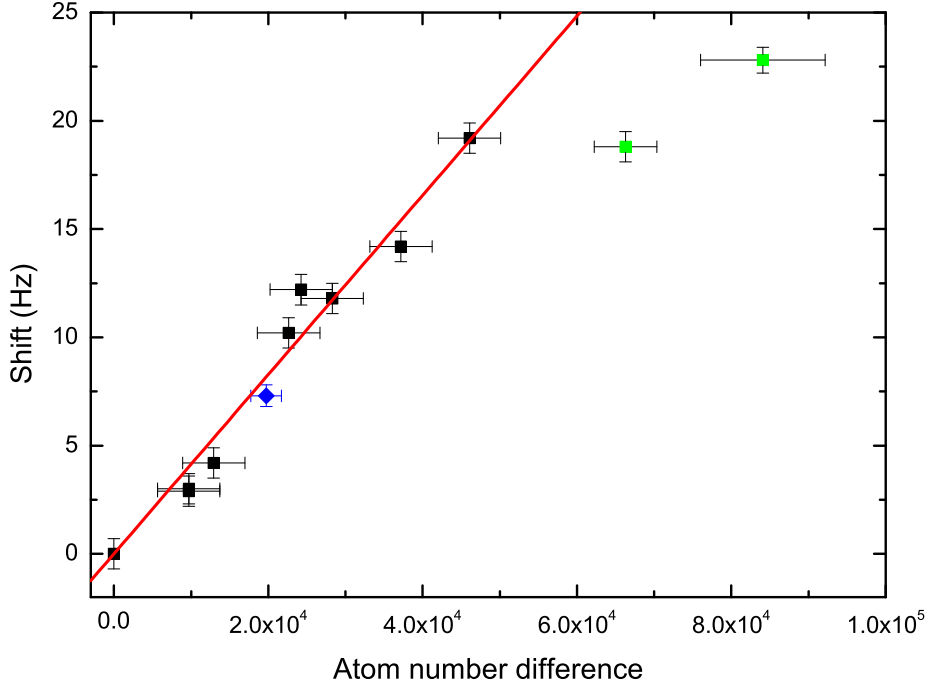
Figure 5.8: Atom number dependent frequency shift of the $^1S_0 \rightarrow {}^3P_0$ clock transition of ^{88}Sr obtained using the interleaved stabilization method. The blue data point (rhombus) indicates the atom number difference at which frequency shift versus excitation probability was measured.

Our observation of the clock frequency shift with respect to atom number is shown in fig. 5.8. The uncertainty of the difference between the measured frequency shift of atoms in cycles A and B is estimated from the Allan deviation plots similar to fig. 5.6(b). We reach an uncertainty of ~ 0.7 Hz at an averaging time $\tau \sim 500$ s. The atom number and its uncertainty were estimated from scans similar to fig. 4.7. Due to the collisional losses discussed in the previous chapter, the maximum excitation

probability varies with density, thus an excitation probability of 35% at lock points was chosen so that it could be reached for the range of atomic densities we measured. The slope $(\overline{\delta\nu}/N)$ of the frequency shift versus atom number which was obtained from the fit (excluding the data shown in green) is $(4.14 \times 10^{-4} \pm 1.5 \times 10^{-5})$ Hz per atom. At low atom number, a linear dependence was observed, but for high atom number a deviation from the linear behavior was seen. This deviation of frequency shift at high atom number could be explained by take into account changes in dynamics during the excitation of the atoms because of losses and dephasing in which case eq. 5.22 is no longer valid. The density shift coefficient ϵ in terms of average frequency shift $\overline{\delta\nu}$, number of atoms N and volume is given as

$$\epsilon = \frac{\overline{\delta\nu}}{N}\frac{2\pi^2 w' w_r^2 w_z}{\lambda}. \tag{5.24}$$

Using eq. 5.24 we calculate $\epsilon = (7.2 \pm 2.0) \times 10^{-17}$ Hz m^3. The uncertainty in the density shift value is due to uncertainties in the density determination.

In order to determine the different scattering lengths, we investigated the shift for different excitation probabilities. We observe a weak variation of density shift depending on the excitation probability at lock points. In this measurement, the atom numbers in cycle A (cycle B) were fixed to 3.2×10^4 $(9.7 \times 10^3)($ shown as blue rhombus in fig. 5.8). The excitation probability at the lock points of cycle B was fixed (35%) and that of cycle A was varied by applying the clock pulse ($t_R = 5$ ms) with different clock laser detuning. The different excitation probability resulted in different values of the coefficient C which were calculated numerically from eq. 5.23.
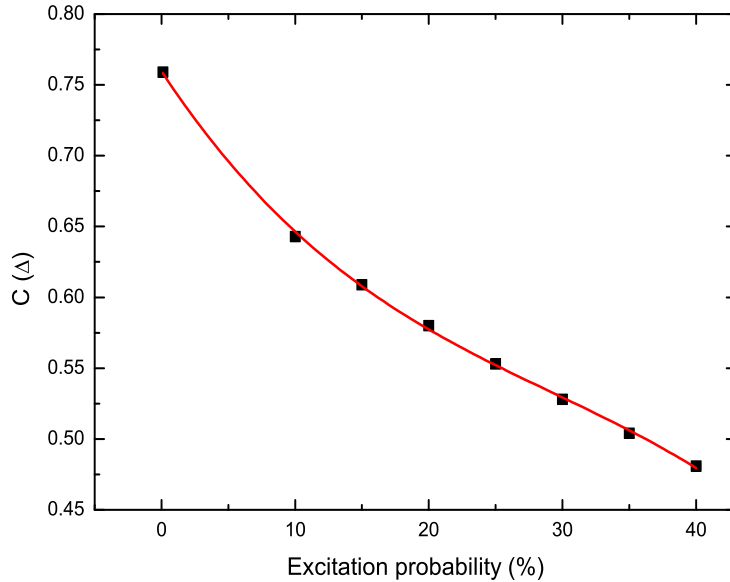
Figure 5.9: Variation of C with respect to excitation probability. The red line is the third order polynomial fit.

Fig. 5.9 shows the value of C for different final excitation probabilities. For the fit, this dependence was approximated by polynomial

$$C(P_e) = 0.7596 + 0.01428\,P_e + 3.3498 \cdot 10^{-4}P_e^2 - 3.824 \cdot 10^{-6}\,P_e^3. \qquad (5.25)$$

Fig. 5.10 shows the difference between the frequency shifts of atoms in cycles A and B with respect to excitation probability of atoms in cycle A. The red line is the fit of the equation

$$(\overline{\delta\nu})_A - (\overline{\delta\nu})_B = c + d\,C(P_e) \qquad (5.26)$$

with

$$
\begin{aligned}
c &= \frac{2\hbar}{m}\left[(a_{ee} - a_{gg})(\rho_A - \rho_B) - 0.504\,\rho_B(a_{ge} - a_{gg} - a_{ee})\right] \\
d &= \frac{2\hbar}{m}\rho_A(a_{ge} - a_{gg} - a_{ee}).
\end{aligned}
\qquad (5.27)
$$
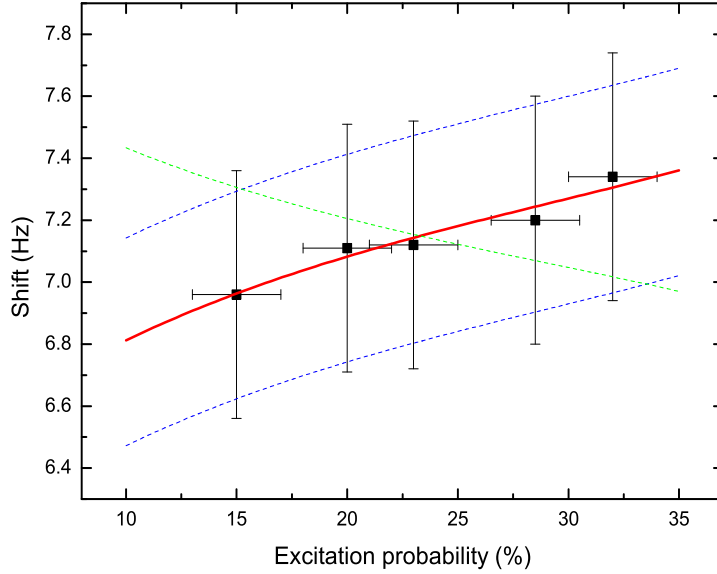
Figure 5.10: Frequency shift vs excitation probability of cycle A. The red line is a fit using eqs. 5.25 and 5.22

For cycle B ($P_e = 0.35$) the value of C was calculated to be 0.504. Using the well known ground state ($^1S_0$) scattering length $a_{gg} = -1.4a_0$ [94], the fit gives the values of $a_{ee} = (985 \pm 40)a_0$ and $a_{ge} = (655 \pm 40)a_0$. The maximum (minimum) value of a_{ee} and a_{ge} correspond to the upper (lower) bound shown as the blue dashed line in fig. 5.10. However, due to the uncertainty in the measured measured frequency shift, it is

difficult to determine whether the slope is positive or negative. The green dashed line in fig. 5.10 which has a negative slope is got by varying the parameters c and d. For the negative slope, we estimate the value of a_{ee} (a_{ge}) to be $678a_0$ ($952a_0$). Traverso .et al [78] reported the value of $a_{ee} = (100 \pm 50)a_0$. This discrepancy, as discussed in the previous chapter, can be attributed to effects of the dimensionality of the trap potential where a strong axial confinement of the particle motion has influence on the elastic scattering [80], further investigations are necessary to experimentally study the role of axial confinement on scattering lengths.

For the operation of the clock, it is desirable to work with a narrow transition. We loaded 3×10^3 atoms in the lattice, for this atom number, we do not expect significant dephasing collisions that would lead to collisional broadening of the transition. The vibration isolation of the clock laser stabilization cavity was improved resulting in a few Hz laser linewidth. Fig. 5.11 shows a narrow line with (10 ± 1) Hz linewidth obtained with an intensity of 12 W/cm^2 and a magnetic field of 500 μT ($\Omega/2\pi \sim 11$ Hz). The uncertainty in the measured linewidth is due to bad signal-to-noise ratio. The clock pulse length was 100 ms giving a Fourier limited linewidth $(0.89/t_R) \sim 9$ Hz. Measurement for longer pulse length did not produce narrower lines indicating some broadening mechanism being present. These mechanisms may include residual laser drift which could influence the linewidth depending on the scan direction and relative drift or mechanical vibrations which can make the probe laser move relative to the atoms in the lattice that will lead to Doppler broadening. To our knowledge, this is the narrowest linewidth achieved in a 1-D ^{88}Sr lattice clock.
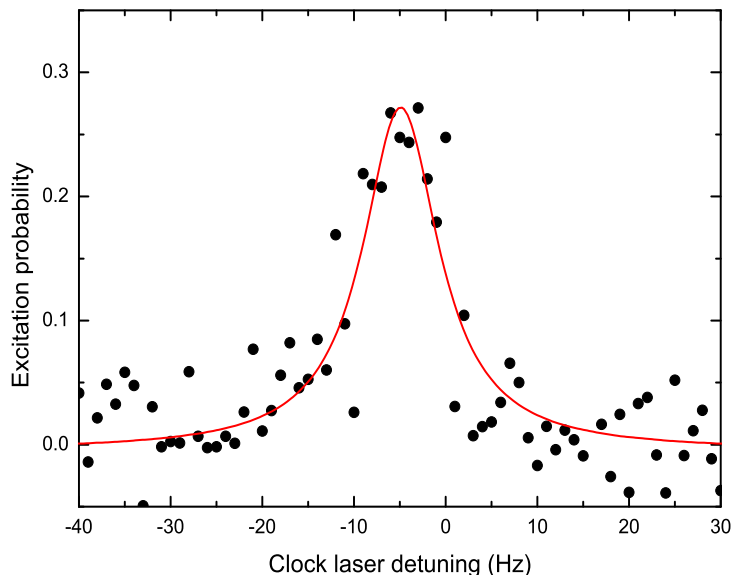

Figure 5.11: Narrow clock transition with 3×10^3 atoms in the lattice. The Lorentzian fit gives a linewidth of 10 Hz.

Having quantified the density shift between clock states of ^{88}Sr atoms, we are in a position to give a guideline for an operational 1-D lattice clock based on ^{88}Sr atoms in which the collisions contribute to the fractional uncertainty (with respect to clock transition) at a level of 10^{-16} which is also the current uncertainty in the frequency shift due to black body radiation [14]. At this level, the uncertainty in the collisional shift should be 0.043 Hz. The slope of the line in fig. 5.8 has an uncertainty of 3.6%, giving us collisional frequency shift to be $0.043/0.036 = 1.2$ Hz. This frequency shift limits the density to 1.7×10^{16} m^{-3}, to optimize the atom number for this density, we calculate a set of lattice parameters. For a 300 mW of power in a single beam and 75 μm waist radius, we get a potential depth of 10 μK for a lattice operating at 813 nm. For an ensemble of atoms distributed along the lattice with $w' = 280$ μm and with 3 μK temperature, eq. 3.3 yields $w_z = 106$ nm and $w_r = 42$ μm along the axial and radial direction. Substituting these values in eq. 5.24 gives us 2×10^4 number of atoms in the lattice. This atom number is comparable or larger than the current lattice clocks based on ^{87}Sr [14, 95] and the collisional broadening found from simulation of eq. 4.14 is about 1.3 Hz. Finally, for these conditions, we estimate from eq. 5.16 quantum projection noise limited stability $\sigma_y(1\,\text{s}) = 2 \times 10^{-17}$ for optimized $T_c = 0.2$ s, to achieve this limit however, the atom number should be controlled to about 0.07%. Thus, the feasible lattice parameters and an atom number demonstrates the possibility of using 1-D lattice clock based on ^{88}Sr without collisional degradation at the level of 10^{-16}.

5.3   Evaluation of systematic effects

Based on the design parameters of the 1-D lattice ^{88}Sr clock, we can evaluate the systematic effects and present a preliminary uncertainty budget. We assume a state-of-the-art clock laser with a 1 Hz linewidth and waist radius of 100 μm. For a Fourier limited linewidth of 2 Hz, we have $t_R \sim 445$ ms and $\Omega/2\pi \sim 1.1$ Hz. This Rabi frequency can be obtained with an intensity $I = 636$ mW/cm^2 and a magnetic field $B = 1.4$ mT. The effects which are described below are shifts due to clock laser light, magnetic field, blackbody radiation and lattice laser.

- **ac Stark shift due to Clock laser**
  Clock laser light induces frequency shift in the clock transition by the ac Stark effect. This shift is proportional to the intensity of the clock laser and it is given as $\Delta_L = \kappa I$ where Δ_L is the frequency shift and I is the clock laser intensity. The value of κ is given in table 2.3. For the given laser intensity, the resulting shift is $\Delta_L = -11.5$ Hz. Fluctuations of laser intensity can be controlled within 0.5% [96], giving us the uncertainty $\delta\Delta_L = 0.05$ Hz.

- **Second order Zeeman shift**
  In the presence of magnetic field the excited state is shifted in energy, this second order Zeeman shift is given as $\Delta_B = \beta|B|^2$. By using the value of β from table 2.3 we have $\Delta_B = -45.7$ Hz. The uncertainty in the magnetic field determination leads to shift uncertainty $\delta\Delta_B = 2\delta B \beta |B|$. With proper shielding, fluctuations

can be controlled better than 1 μT. For a magnetic field of 1.4 mT with 0.1% uncertainty in its determination we have $\delta\Delta_B = 0.09$ Hz.

- **Shift due to blackbody radiation**

  Due to the different static polarizabilities (α_{dc}) of the two clock states, the black body radiation shifts clock frequency. This shift, for a given temperature T is given as

$$\Delta_R = -\frac{k_B^4}{60\epsilon_0\hbar^4 c^3}\Delta\alpha_{dc}T^4 = -2.354(32)\left(\frac{T}{300K}\right)^4 \text{ Hz.} \qquad (5.28)$$

  The uncertainty in the constant is the result from the calculation of polarizabilities [48]. For a temperature of the chamber of (294 ± 1) K, we get a blackbody radiation shift of $\Delta_R = 2.2$ Hz and $\delta\Delta_R = 0.042$ Hz.

- **Shift due to lattice laser**

  The clock transition frequency ν_0 gets modified in the presence of lattice laser, this shifted frequency can be expressed as [39]

$$\nu = \nu_0 + \nu_1\frac{U_0}{E_r} + \nu_2\frac{U_0^2}{E_r^2} + O\left(\frac{U_0^3}{E_r^3}\right) \qquad (5.29)$$

  where E_r is the lattice photon recoil energy. ν_1 is proportional to the ac polarizabilities of the clock states which is canceled by operating the lattice at magic wavelength. No scheme till now exist that would cancel second term which is to due to the hyperpolarizability difference between the clock states. The measurement of shift due to hyperpolarizability gives a value [39] $\nu_1 = 7(6)$ μHz. Using this value, we estimate the shift due to the hyperpolarizability effect for the lattice power of 300 mW ($U_0 = 60E_r$) with a 0.5% intensity fluctuation to be $\Delta_H = 0.025$ Hz and an uncertainty $\delta\Delta_H = 0.002$ Hz which is below 10^{-17} level.

Systematic effects	Shift (Hz)	Fractional uncertainty (10^{-16})
ac Stark (clock laser)	-11.5	1.3
2nd order Zeeman effect	-45.7	2
BBR shift	2.2	0.97
Hyperpolarizability	0.54	0.04
Collisional shift	1.2	1
Total	-53.26	2.8

Table 5.1: Shift and uncertainty budget for 1-D lattice based ^{88}Sr clock. Uncertainty is given with respect to clock transition $\nu_0 = 429 \cdot 10^{12}$ Hz

Table 5.1 shows the uncertainty budget calculated from measured perturbation parameters. From table 5.1, we find that the shift due to the ac Stark effect and quadratic Zeeman shift is significant compared to other shifts. Further control over the intensity and magnetic field is necessary to lower the uncertainty to 10^{-17} level [96]. The uncertainty contribution from the black body radiation can be reduced by accurate

experimental determination of blackbody shift coefficient and operating the MOT in a temperature controlled environment [14]. Finally, a new density shift measurement with the proposed lattice parameters should give us an improved correction in the collisional shift.

In this chapter, the technique of interleaved stabilization which was used to measure the density shift was described in detail. This method can also be used to measure the effects of other perturbations that influences an optical frequency standard (eg: second order Zeeman effect, light shift of probe laser etc.). The limitation of this method is set by the frequency noise of the clock laser, atom number fluctuations and non-linearity of the cavity drift. Based on our measurement of the density shift coefficient, we were able to propose optical lattice parameters and an atom number under which the collisions do not degrade the fractional uncertainty at the level of 10^{-16} and evaluate a preliminary uncertainty budget.

Chapter 6

Conclusion and outlook

In this thesis inelastic collisions, decoherence effects and density dependent frequency shift in a 1-D ^{88}Sr lattice clock were investigated. To study these effects, strontium atoms were laser-cooled using a two-stage cooling process. In the first stage, the atoms are cooled down to 2.5 mK and a temperature of 3 μK is reached with the second stage cooling. The atoms are simultaneously loaded into the optical lattice operating at magic wavelength of 813 nm while they are being cooled in the intercombination line. The lifetime of the atoms in the lattice is 7.5 s which is limited by background collisions. The forbidden $^1S_0 \rightarrow ^3P_0$ clock transition is enabled by applying a static homogeneous magnetic field that admixes the $^3P_1$ to the $^3P_0$ state.

In order to study inelastic losses, experiment was conducted with only $^3P_0$ atoms in the lattice to study $^3P_0 + ^3P_0$ collisions. By measuring the decay of $^3P_0$ atoms, the loss rate γ_{ee} was obtained. Similarly, the loss rate γ_{ge} due $^1S_0 + ^3P_0$ collisions was obtained by observing the decay of $^1S_0$ and $^3P_0$ atoms. From the loss rates the inelastic scattering lengths $\text{Im}(a_{ee})$ and $\text{Im}(a_{eg})$ were calculated. Study of collisional broadening of the clock transition showed a new dephasing mechanism proportional to the ground state atoms. A master equation was developed to fit the observed clock transitions and Rabi oscillations. By observing the excitation dynamics for different atom numbers, the dephasing coefficient γ_{dep} was determined. Our observations show that this dephasing effect does not affect the excitation dynamics for low atom numbers. In our experimental setup, we have shown that a Q factor of 4×10^{13} can be achieved by having few thousand atoms in the lattice. This is the highest Q factor achieved in a 1-D ^{88}Sr lattice clock to our knowledge.

Third collision effect being important for an neutral atom based optical clock is the frequency shift due to collisions. This shift ϵ was measured using interleaved stabilization method. The uncertainty in the shift is mainly due to to density determination. At low atom number, a linear dependence was observed but for high atom number a deviation from the linear behavior was seen. This deviation of frequency shift at high atom number could be explained by take into account changes in dynamics during the excitation of the atoms because of losses and dephasing. A weak dependence of the density shift on the excitation probability of atoms was observed and from this measurement, upper and lower bounds of $^1S_0 + ^3P_0$ and $^3P_0 + ^3P_0$ elastic scattering lengths were estimated.

Because of the small frequency shifts due to density, it was crucial to study the interleaved stabilization scheme in detail and optimize. Our method of estimation of the error signal and its correction was presented in this thesis. Time constants resulting from fractional error correction in each measurement cycle and errors due to non-linear drift of the clock laser reference cavity were estimated for our set up. We conclude that different uncertainties that arise in our experiment while using this method does not limit the uncertainty of our measurement at 10^{-16} level. Possible experiments using interleaved scheme to measure frequency shifts, for example, shifts due to quadratic Zeeman effect and ac Stark shift of the probe laser whose values have been only determined theoretically, will find the expressions for time constants and estimated errors useful.

With the loss and the shift coefficients determined in this thesis, it was shown that a 1-D lattice clock based on ^{88}Sr shows no degradation due to collisions at the level of 10^{-16}. This guideline for the design of a 1D-lattice clock with bosonic ^{88}Sr will be of help in designing portable setups. Such portable optical clocks operated in space can be used to make precise measurement of gravitational redshift, mapping of earth's gravitational field or improved in space navigation. Possible experiments which can be limited by coherence time, for example using ^{88}Sr atoms as quantum registers [97] or to use them in producing millihertz linewidth lasers will benefit from the results of this thesis work. The scattering lengths calculated in this work can be used to estimate scattering lengths of other strontium isotopes using mass scaling laws.

Active development of optical lattice clocks has lead to explore other elements such as Ytterbium and Mercury. Each element offers some kind of advantage over the other elements. For example, the natural line-width of fermionic ^{87}Sr isotope is 1 mHz, compared to this the natural line-width of fermionic ^{171}Yb isotope is 10 mHz, however, the nuclear spin of ^{171}Yb ($I = 1/2$) offers a simple spin system [98, 99]. Neutral mercury atoms for example have BBR (Black body radiation) shift which is an order of magnitude smaller [100] than that of Strontium and Ytterbium and work is underway to construct an optical lattice clock based on neutral mercury atoms [101, 102]. This thesis concludes by highlighting that advances in various fields spearheaded by the improvement in accuracy and stability of measurement of time is the driving force that pushes the limit of timekeeping to this day.

Appendix A

Expression for density dependent frequency shift

In a 1-D optical lattice, different potential wells (lattice sites) are occupied by different number of atoms. Let N_n be the number of atoms in a potential well labeled n and N be the total number of atoms trapped in all the lattice sites ($N = \sum_n N_n$). The frequency shift ($\delta\nu$) of the atoms inside a potential well with density distribution $\rho(r)$ is given as $\delta\nu = \epsilon\rho(r)$ where ϵ is the coefficient of density shift. Average density shift of the atoms inside a single potential well is given as

$$\overline{\delta\nu_n} = \frac{\int dr^3 \delta\nu\rho(r)}{N_n} = \frac{\int dr^3 \epsilon\rho^2(r)}{N_n}. \tag{A.1}$$

If w_z and w_r are the $1/e^2$ radii of the distribution of the atoms along the axial and the radial direction in each potential well, the Gaussian density distribution in a potential well i is expressed as

$$\rho(r) = \rho_0 e^{\frac{-2x^2}{w_r^2}} e^{\frac{-2y^2}{w_r^2}} e^{\frac{-2z^2}{w_z^2}} \tag{A.2}$$

where ρ_0 is the peak density inside the potential well. Atom number in each potential well can be expressed as $N_n = \int dV \rho(r)$, using the relation $\int_{-\infty}^{\infty} dx\ e^{\frac{-x^2}{A}} = \sqrt{A\pi}$ the atom number in each potential well is given by

$$N_n = \int dV \rho(r) = \rho_0 \frac{w_r^2 w_z \pi}{2} \sqrt{\frac{\pi}{2}}. \tag{A.3}$$

By using eqs. A.2 and A.3 the average frequency shift inside a potential well is expressed as

$$\overline{\delta\nu_n} = \frac{\epsilon N_n}{\pi^{\frac{3}{2}} w_r^2 w_z}. \tag{A.4}$$

Eq. A.4 gives the average frequency shift experienced by the atoms in a single potential well. In order to derive an expression for the average frequency shift experienced by total number of atoms N trapped in all optical lattice sites, we first note that absorption images of the atoms in the optical lattice show a Gaussian distribution of atoms along the axial direction of the lattice beam. Therefore different lattice sites

are occupied with different atom numbers given by a Gaussian distribution. If λ is the wavelength of the lattice beam and w' is the $1/e^2$ radius of the atom distribution along the axial direction of the lattice beam, then the atom number in each lattice site is given as

$$N_n = N_0 e^{\frac{-2(n\frac{\lambda}{2})^2}{(w')^2}} \tag{A.5}$$

where N_0 is the peak atom number along the axial direction of the lattice beam. Total number of atoms is given by summing over N_n over all lattice sites

$$\begin{aligned}
N &= \sum_{n=-\infty}^{\infty} N_0 e^{\frac{-2(n\frac{\lambda}{2})^2}{(w')^2}} \\
&\approx N_0 \int dn\, e^{\frac{-\lambda^2 n^2}{2(w')^2}} \\
&\approx \sqrt{2\pi} N_0 \frac{w'}{\lambda}.
\end{aligned} \tag{A.6}$$

Average frequency shift $\overline{\delta\nu}$ of the total number of atoms is given by summing the average frequency shifts experienced by atoms in each potential well and diving by total number of atoms.

$$\begin{aligned}
\overline{\delta\nu} &= \frac{\sum_{n=-\infty}^{\infty} \overline{\delta\nu_n} N_0 e^{\frac{-2(n\frac{\lambda}{2})^2}{(w')^2}}}{N} \\
&= \frac{N_0^2 \epsilon}{\pi^{\frac{3}{2}} w_r^2 w_z N} \int dn\, e^{\frac{-\lambda^2 n^2}{(w')^2}}.
\end{aligned} \tag{A.7}$$

Using Eq.A.6, the expression for average frequency shift $\overline{\delta\nu}$ simplifies to

$$\overline{\delta\nu} = \frac{\lambda \epsilon N}{2\pi^2 w' w_r^2 w_z}. \tag{A.8}$$

Appendix B

Expression for locking error signal
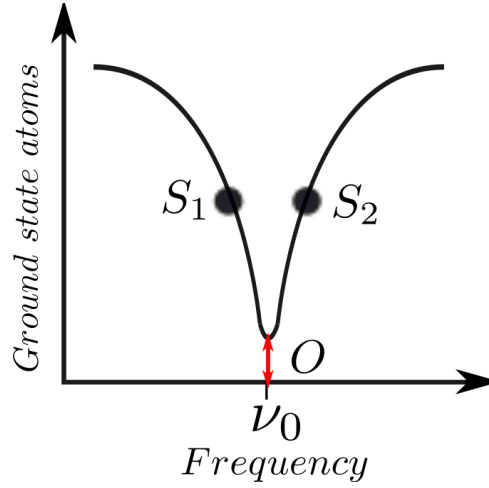

Figure B.1: Schematic of clock transition showing the lock points S_1, S_2 and offset O.

We derive the expression for the error signal that is used to stabilize the clock laser to the atoms. The basic assumption is that the transition line is Lorenztian in shape. Let ν_L and ν_0 be the laser and clock transition frequency. Then we have the difference $\pm\nu_{\text{error}} = \nu_L - \nu_0$ where the error signal is positive or negative depending on the laser frequency is greater or less than the clock transition frequency. The Lorentz model used is

$$S = a - \frac{a - O}{\frac{4(\nu_L - \nu_0^2)}{\Delta} + 1} \tag{B.1}$$

where Δ is FWHM of the transition, $a = S_1 + S_2 - 0$. FigureB.1 shows the schematic of the clock transition detected using ground state atoms. Let $\nu_L > \nu_0$ in this example, when the laser probes at $\pm\Delta/2$ we have $S2 - S_1 > 0$. S_1 and S_2 are given as

$$S_1 = a - \frac{a - O}{\frac{4[(\nu_L - \Delta/2) - (\nu_L - \nu_{\text{error}})]^2}{\Delta^2} + 1} \tag{B.2}$$

$$S_2 = a - \frac{a - O}{\dfrac{4[(\nu_L + \Delta/2) - (\nu_L - \nu_{\text{error}})]^2}{\Delta^2} + 1}. \tag{B.3}$$

Subtracting S_1 from S_2 and neglecting the terms ν_{error}^2 and $(\nu_{\text{error}}/\Delta)^2$ we get

$$\nu_{\text{error}} = \Delta \frac{S_2 - S_1}{2(S_2 + S_1 - 2 \cdot O)}. \tag{B.4}$$

If the transition is probed at width δ which is related to Δ as $\delta = \mu\Delta$ we have

$$S_1 - S_2 = \frac{a - O}{\dfrac{4(\nu_{\text{error}} - \gamma/2)^2}{\Delta^2} + 1} - \frac{a - O}{\dfrac{4(\nu_{\text{error}} + \gamma/2)^2}{\Delta^2} + 1}. \tag{B.5}$$

Ignoring again the terms ν_{error}^2 and $(\nu_{\text{error}}/\Delta)^2$ we end up with

$$\nu_{\text{error}} = \kappa\Delta \frac{S_2 - S_1}{2(S_2 + S_1 - 2 \cdot O)}. \tag{B.6}$$

with $\kappa = \frac{1}{4\mu}(\mu^2 + 1)^2$

Bibliography

[1] Zeb Barber. *Ytterbium Optical Lattice Clock*. PhD thesis, University of Colorado, 2007.

[2] Thomas Legero, Christian Lisdat, J. S. R. Vellore Winfred, Harald Schnatz, Gesine Grosche, Fritz Riehle, and Uwe Sterr. Interrogation laser for a strontium lattice clock. *IEEE Trans. Instrum. Meas.*, 58:1252–1257, 2009.

[3] W.F. Snyder. Lord Kelvin on atoms as fundamental natural standards. *IEEE Trans. Instrum. Meas.*, 22:99, 1973.

[4] D.B. Sullivan. Time and frequency measurement at NIST: The first 100 years. *Frequency Control Symposium and PDA Exhibition,2001.Proceedings of the 2001 IEEE International*, pages 4–17, 2001.

[5] I.I. Rabi, S. Milliman, P. Kush, and J.R. Zacharias. The molecular beam resonance method for measuring nuclear magnetic moments. *Phys. Rev.*, 55:526–535, 1939.

[6] N.F. Ramsey. The method of successive oscillatory fields. *Phys. Today*, 33:25–30, 1980.

[7] P. Giacomo. News from the BIPM. *Metrologia*, 20:25–30, 1984.

[8] Norman F. Ramsey. History of atomic clocks. *J. Res. NBS*, 88:301–320, 1983.

[9] SI brochure (8^{th}edition). Website. `http://www.bipm.org/en/si/si_brochure/chapter2/2-1/second.html`.

[10] D. W. Allan. Statistics of atomic frequency standards. *Proc. IEEE*, 54:221–230, 1966.

[11] Andreas Bauch. Caesium atomic clocks: Function, performance and applications. *Meas. Sci. Technol.*, 14:1159–1173, 2003.

[12] T. Udem, R. Holzwarth, and T.W. Hansch. Optical frequency metrology. *Nature*, 416:233–237, 2002.

[13] L. Lorini, N. Ashby, A. Brusch, S. Diddams, R. Drullinger, E. Eason1and T. Fortier, P. Hastings, T. Heavner, D. Hume, W. Itano, S. Jefferts, N. Newbury, T. Parker, T. Rosenband, J. Stalnaker, W. Swann, D. Wineland, and J. Bergquist. Recent atomic clock comparisons at NIST. *Eur. Phys. J. Special Topics*, 163:1935, 2008.

[14] A. D. Ludlow, T. Zelevinsky, G. K. Campbell, S. Blatt, M. M. Boyd, M. H. G. de Miranda, M. J. Martin, J. W. Thomsen, S. M. Foreman, Jun Ye, T. M. Fortier, J. E. Stalnaker, S. A. Diddams, Y. Le Coq, Z. W. Barber, N. Poli, N. D. Lemke, K. M. Beck, and C. W. Oates. Sr lattice clock at 1×10^{-16} fractional uncertainty by remote optical evaluation with a Ca clock. *Science*, 319:1805–1808, 2008.

[15] H. G. Dehmelt. Mono-ion oscillator as potential ultimate laser frequency standard. *IEEE Trans. Instrum. Meas.*, IM–31:83–87, 1982.

[16] H S Margolis. Frequency metrology and clocks. *J. Phys. B: At. Mol. Opt. Phys.*, 42:154017, 2009.

[17] T. Rosenband, D. B. Hume, P. O. Schmidt, C. W. Chou, A. Brusch, L. Lorini, W. H. Oskay, R. E. Drullinger, T. M. Fortier, J. E. Stalnaker, S. A. Diddams, W. C. Swann, N. R. Newbury, W. M. Itano, D. J. Wineland, and J. C. Bergquist. Frequency ratio of Al^+ and Hg^+ single-ion optical clocks; metrology at the 17th decimal place. *Science*, 319:1808–1812, 2008.

[18] R. H. Dicke. The effect of collisions upon the Doppler width of spectral lines. *Phys. Rev.*, 89:472–473, 1953.

[19] R. J. Rafac, B. C. Young, J. A. Beall, W. M. Itano, D. J. Wineland, and J. C. Bergquist. Sub-dekahertz ultraviolet spectroscopy of $^{199}Hg^+$. *Phys. Rev. Lett.*, 85:2462–2465, 2000.

[20] Th. Becker, J. v. Zanthier, A. Yu. Nevsky, Ch. Schwedes, M. N. Skvortsov, H. Walther, and E. Peik. High-resolution spectroscopy of a single In^+ ion: Progress towards an optical frequency standard. *Phys. Rev. A*, 63:051802–1–4, 2001.

[21] P. J. Blythe, S. A. Webster, H. S. Margolis, S. N. Lea, G. Huang, S.-K. Choi, W. R. C. Rowley, and P. Gill. Subkilohertz absolute-frequency measurement of the 467-nm electric octupole transition in $^{171}Yb^+$. *J. Phys. B: At. Mol. Phys.*, 36:981–989, 2003.

[22] H. S. Margolis, G. P. Barwood, G. Huang, H. A. Klein, S. N. Lea, K. Szymaniec, and P. Gill. Hertz-level measurement of the optical clock frequency in a single $^{88}Sr^+$ ion. *Science*, 306:1355–1358, 2004.

[23] T. Rosenband, P. O. Schmidt, D. B. Hume, W. M. Itano, T. M. Fortier, J. E. Stalnaker, K. Kim, S. A. Diddams, J. C. J. Koelemeij, J. C. Bergquist, and D. J. Wineland. Observation of the $^1S_0$ - $^3P_0$ clock transition in $^{27}Al^+$. *Phys. Rev. Lett.*, 98:220801–1–4, 2007.

[24] J. L. Hall, M. Zhu, and P. Buch. Prospects for using laser-prepared atomic fountains for optical frequency standards applications. *J. Opt. Soc. Am. B*, 6:2194–2205, 1989.

[25] W. Ertmer, R. Blatt, and J.L. Hall. Some candidate atoms and ions for frequency standards research using laser radiative cooling techniques. *Proc.Quant.Electr*, 8:249–255, 1984.

[26] C. Degenhardt, T. Nazarova, C. Lisdat, H. Stoehr, U. Sterr, and F. Riehle. Influence of chirped excitation pulses in an optical clock with ultracold calcium atoms. *IEEE Trans. Instrum. Meas.*, 54:771–775, 2005.

[27] P.S. Jessen and I.H. Deutsch. Optical lattices. In B. Bederson and H. Walther, editors, *Advances in Atomic, Molecular, and Optical Physics*, volume 37, page 95, Amsterdam, 1996. Elsevier.

[28] Hidetoshi Katori. Spectroscopy of strontium atoms in the Lamb-Dicke confinement. In P. Gill, editor, *Proceedings of the Sixth Symposium on Frequency Standards and Metrology, 9–14 September 2001, St. Andrews, Scotland*, pages 323–330, Singapore, 2002. World Scientific.

[29] Hidetoshi Katori, Masao Takamoto, V. G. Pal'chikov, and V. D. Ovsiannikov. Ultrastable optical clock with neutral atoms in an engineered light shift trap. *Phys. Rev. Lett.*, 91:173005–1–4, 2003.

[30] S. G. Karshenboim and E. Peik, editors. *Astrophysics, Clocks and Fundamental Constants*, volume 648 of *Lecture Notes in Physics*. Springer, Berlin, Heidelberg, New York, 2004.

[31] E. Peik, B. Lipphardt, H. Schnatz, T. Schneider, Chr. Tamm, and S. G. Karshenboim. Limit on the present temporal variation of the fine structure constant. *Phys. Rev. Lett.*, 93:170801–1–4, 2004.

[32] V. A. Dzuba, V. V. Flambaum, and J. K. Webb. Space-time variation of physical constants and relativistic corrections in atoms. *Phys. Rev. Lett.*, 82:888–891, 1999.

[33] A. D. Ludlow, S. Blatt, T. Zelevinsky, G.K. Campbell, M.J. Martin, J.W. Thomsen, M.M. Boyd, and J. Ye. Ultracold strontium clock: applications to the measurement of fundamental constant variations. *Eur. Phys. J. Special Topics*, 163:9–18, 2008.

[34] V.V. Flambaum. Variation of fundamental constants: theory and observations. arXiv:physics/0705.3704v1, 2007.

[35] Masao Takamoto and Hidetoshi Katori. Spectroscopy of the $^1S_0 \rightarrow {}^3P_0$ clock transition of ^{87}Sr in an optical lattice. *Phys. Rev. Lett.*, 91:223001–1–4, 2003.

[36] Masao Takamoto, Feng-Lei Hong, Ryoichi Higashi, and Hidetoshi Katori. An optical lattice clock. *Nature*, 435:321–324, 2005.

[37] Andrew D Ludlow, Martin M Boyd, T Zelevinsky, Seth M Foreman, Sebastian Blatt, Mark Notcutt, Tetsuya Ido, and Jun Ye. Systematic study of the ^{87}Sr clock transition in an optical lattice. *Phys. Rev. Lett.*, 96:033003, 2006.

[38] Rudolphe Le Targat, Xavier Baillard, Mathilde Fouché, Anders Brusch, Olivier Tcherbakoff, Giovanni D. Rovera, and Pierre Lemonde. Accurate optical lattice clock with ^{87}Sr atoms. *Phys. Rev. Lett.*, 97:130801–1–4, 2006.

[39] Anders Brusch, Rodolphe Le Targat, Xavier Baillard, Mathilde Fouche, and Pierre Lemonde. Hyperpolarizability effects in a Sr optical lattice clock. *Phys. Rev. Lett.*, 96:103003, 2006.

[40] V. A. Davydkin and V. D. Ovsiannikov. The hyperpolarisability of an excited atom. *J. Phys. B: At. Mol. Phys.*, 19:2071–2083, 1986.

[41] V.D. Ovsiannikov, V.G. Pal'chikov, H. Katori, and M. Takamoto. Polarisation and dispersion properties of light shifts in ultrastable optical frequency standards. *Quantum Electronics*, 36:3–19, 2006.

[42] A. V. Taichenachev, V. I. Yudin, V. D. Ovsiannikov, and V. G. Pal'chikov. Optical lattice polarization effects on hyperpolarizability of atomic clock transitions. *Phys. Rev. Lett.*, 97:173601–1–4, 2006.

[43] Takashi Mukaiyama, Hidetoshi Katori, Tetsuya Ido, Ying Li, and Makoto Kuwata-Gonokami. Recoil-limited laser cooling of Sr atoms near the Fermi temperature. *Phys. Rev. Lett.*, 90(11):113002, 2003.

[44] Tao Hong, Claire Cramer, Warren Nagourney, and E. N. Fortson. Optical clocks based on ultranarrow three-photon resonances in alkaline earth atoms. *Phys. Rev. Lett.*, 94:050801, 2005.

[45] A. V. Taichenachev, V. I. Yudin, C. W. Oates, C. W. Hoyt, Z. W. Barber, and L. Hollberg. Magnetic field-induced spectroscopy of forbidden optical transitions with application to lattice-based optical atomic clocks. *Phys. Rev. Lett.*, 96:083001, 2006.

[46] Tomoya Akatsuka, Masao Takamoto, and Hidetoshi Katori. Optical lattice clocks with non-interacting bosons and fermions. *Nature Physics*, 4:954–959, 2008.

[47] S. Schiller, A. Goerlitz, A. Nevsky, J. C. J. Koelemeij, A. Wicht, P. Gill, H. A. Klein, H. S. Margolis, G. Mileti, U. Sterr, F. Riehle, E. Peik, Chr Tamm, W. Ertmer, E. Rasel, V. Klein, C. Salomon, G. M. Tino, P. Lemonde, R. Holzwarth, and T. W. Hänsch. Optical clocks in space. *Nuclear Physics B (Proc. Suppl.)*, 166:300302, 2006. Proc. III International Conference on Particle and Fundamental Physics in Space (SpacePart06), Beijing 19 - 21 April 2006, to appear in Nucl. Phys. B.

[48] Sergey G. Porsev and Andrei Derevianko. Multipolar theory of blackbody radiation shift of atomic energy levels and its implications for optical lattice clocks. *Phys. Rev. A*, 74:020502, 2006.

[49] Xinye Xu, Thomas H. Loftus, John L. Hall, Allan Gallagher, and Jun Ye. Cooling and trapping of atomic strontium. *J. Opt. Soc. Am. B*, 20:968–976, 2003.

[50] E. U. Condon and G. H. Shortley. *The Theory of Atomic Spectra.* Cambridge University Press, 1953.

[51] Kwang-Hoon Ko, You-Kyoung Lim, Do-Young Jeong, Hyunmin Park, Taek-Soo Kim, Gwon Lim, and Hyung Ki Cha. Measurement of the isotope selectivity of the strontium magneto-optical trap by a time-of-flight mass spectrometer. *J. Opt. Soc. Am. B*, 23:2465–2469, 2006.

[52] D. J. Wineland and Wayne M. Itano. Laser cooling of atoms. *Phys. Rev. A*, 20:1521–1540, 1979.

[53] P. T. H. Fisk. Trapped-ion and trapped-atom microwave frequency standards. *Rep. Prog. Phys.*, 60:761–817, 1997.

[54] Fritz Riehle. *Frequency Standards: Basics and Applications.* Wiley-VCH, Weinheim, 2004.

[55] Martin M. Boyd. *High Precision Spectroscopy of Strontium in an Optical Lattice: Towards a New Standard for Frequency and Time.* PhD thesis, Graduate School of the University of Colorado, 2007.

[56] D. J. Wineland, W. M. Itano, J. C. Bergquist, and R. G. Hulet. Laser-cooling limits and single-ion spectroscopy. *Phys. Rev. A*, 36:2220–2232, 1987.

[57] R. Jáuregui, N. Poli, G. Roati, and G. Modugno. Anharmonic parametric excitation in optical lattices. *Phys. Rev. A*, 64(3):033403, 2001.

[58] Jinwei Wu, Raymond Newell, Marc Hausmann, David J. Vieira, and Xinxin Zhao. Loading dymanics of optical trap and parametric excitation resonances of trapped atoms. *J. Appl. Phys.*, 100:054903, 2006.

[59] Pierre Lemonde and Peter Wolf. Optical lattice clock with atoms confined in a shallow trap. *Phys. Rev. A*, 72:033409–1–6, 2005.

[60] Rudolf Grimm, Matthias Weidemüller, and Yurii B. Ovchinnikov. Optical dipole traps for neutral atoms. *Adv. At. Mol. Opt. Phys.*, 42:95–170, 2000.

[61] S. Friebel, C. DAndrea, J. Walz, M. Weitz, and T. W. Hänsch. Co2-laser optical lattice with cold rubidium atoms. *Phys. Rev. A*, 57:R20, 1998.

[62] B. H. Bransden and C. J. Joachain. *Physics of Atoms and Molecules.* Prentice Hall, Harlow, England, 2003.

[63] Andrew D. Ludlow. *The Strontium Optical Lattice Clock: Optical Spectroscopy with Sub-Hertz Accuracy.* PhD thesis, University of Colorado, Boulder, 2008.

[64] Robin Santra, Ennio Arimondo, Tetsuya Ido, Chris H. Greene, and Jun Ye. High-accuracy optical clock via three-level coherence in neutral bosonic ^{88}Sr. *Phys. Rev. Lett.*, 94:173002–1–4, 2005.

[65] J.V. Prodan, W.D. Phillips, and H. Metcalf. Laser production of a very slow monoenergetic atomic beam. *Phys. Rev. Lett.*, 49:1149–1153, 1982.

[66] P. D. Lett, W. D. Phillips, S. L. Rolston, C. E. Tanner, R. N. Watts, and C. I. Westbrook. Optical molasses. *J. Opt. Soc. Am. B*, 6:2084–2107, 1989.

[67] Rodolphe Le Targat, Jean-Jacques Zondy, and Pierre Lemonde. 75%-Efficiency blue generation from an intracavity PPKTP frequency doubler. *Opt. Commun.*, 247:471–481, 2005.

[68] Thierry Chanelière, Jean-Louis Meunier, Robin Kaiser, Christian Miniatura, and David Wilkowski. Extra-heating mechanism in Doppler cooling experiments. *J. Opt. Soc. Am. B*, 22:1819–1828, 2005.

[69] K. Liu and M. G. Littman. Novel geometry for single-mode scanning of tunable lasers. *Opt. Lett.*, 6:117–118, 1981.

[70] R. W. P. Drever, J. L. Hall, F. V. Kowalski, J. Hough, G. M. Ford, A. J. Munley, and H. Ward. Laser phase and frequency stabilization using an optical resonator. *Appl. Phys. B*, 31:97–105, 1983.

[71] Eric D. Black. An introduction to Pound-Drever-Hall laser frequency stabilization. *Am. J. Phys.*, 69:79–87, 2001.

[72] Hidetoshi Katori, Tetsuya Ido, Yoshitomo Isoya, and Makoto Kuwata-Gonokami. Magneto-optical trapping and cooling of strontium atoms down to the photon recoil temperature. *Phys. Rev. Lett.*, 82:1116–1119, 1999.

[73] Thomas H. Loftus, Tetsuya Ido, Martin M. Boyd, Andrew D. Ludlow, and Jun Ye. Narrow line cooling and momentum-space crystals. *Phys. Rev. A*, 70:063413, 2004.

[74] Thomas H. Loftus, Tetsuya Ido, Andrew D. Ludlow, Martin M. Boyd, and Jun Ye. Narrow line cooling: Finite photon recoil dynamics. *Phys. Rev. Lett.*, 93:073003, 2004.

[75] Ch. Grain, T. Nazarova, C. Degenhardt, F. Vogt, Ch. Lisdat, E. Tiemann, U. Sterr, and F. Riehle. Feasibility of narrow-line cooling in optical dipole traps. *Eur. Phys. J. D*, 42:317–324, 2007.

[76] S.P. Singh and N. Singh. Nonlinear effects in optical fibers: orgin, management and applications. *Progress In Electromagnetics Research, PIER*, 732:249–275, 2007.

[77] S.P. Singh, R. Gangwar, and N. Singh. Nonlinear scattering effects in optical fibers. *Progress In Electromagnetics Research, PIER*, 74:379–405, 2007.

[78] A. Traverso, R. Chakraborty, Y. N. Martinez de Escobar, P. G. Mickelson, S. B. Nagel, M. Yan, and T. C. Killian. Inelastic and elastic collision rates for triplet states of ultracold strontium. *Phys. Rev. A*, 79:060702(R)–1–4, 2009.

[79] D. Leibfried, R. Blatt, C. Monroe, and D. Wineland. Quantum dynamics of single trapped ions. *Rev. Mod. Phys.*, 75:281–324, 2003.

[80] A. Peters, K. Y. Chung, and S. Chu. High-precision gravity measurements using atom interferometry. *Metrologia*, 38:25–61, 2001.

[81] N. Boutassetta, A. R. Allouche, and M. Aubert-Frécon. Theoretical study of the electronic structure of the Sr_2 molecule. *Phys. Rev. A*, 53(6):3845–3852, 1996.

[82] E. Czuchaj, M. Krośnicki, and H. Stoll. Valence ab initio calculation of the potential energy curve for the Sr_2 dimer. *Chem. Phys. Lett.*, 371:401–409, 2003.

[83] O. Allard, St. Falke, A. Pashov, O. Dulieu, H. Knöckel, and E. Tiemann. Study of coupled states for the $(4s^2)^1S + (4s4p)^3P$ asymptote of Ca_2^*. *Eur. Phys. J. D*, 35:483–497, 2005.

[84] Claude Cohen Tannoudji, Jacques Dupont-Roc, and Gilbert Grynberg. *Atom-Photon Inteactions. Basic processes and applications*. WILEY-VCH, 2004.

[85] Carsten Degenhardt, Hardo Stoehr, Uwe Sterr, Fritz Riehle, and Christian Lisdat. Wavelength dependent ac-Stark shift of the $^1S_0$-$^3P_1$ transition at 657 nm in Ca. *Phys. Rev. A*, 70:023414–1–6, 2004.

[86] Carsten Degenhardt, Hardo Stoehr, Christian Lisdat, Guido Wilpers, Harald Schnatz, Burghard Lipphardt, Tatiana Nazarova, Paul-Eric Pottie, Uwe Sterr, Jürgen Helmcke, and Fritz Riehle. Calcium optical frequency standard with ultracold atoms: Approaching 10^{-15} relative uncertainty. *Phys. Rev. A*, 72:062111–1–17, 2005.

[87] Audrey Quessada, Richard P Kovacich, Irène Courtillot, André Clairon, Giorgio Santarelli, and Pierre Lemonde. The Dick effect for an optical frequency standard. *J. Opt. B: Quantum Semiclass. Opt.*, 5:S150–S154, 2003.

[88] G. J. Dick, J. Prestage, C. Greenhall, and L. Maleki. Local oscillator induced degradation of medium-term stability in passive atomic frequency standards. In *Proceedings of the 22nd Annual Precise Time and Time Interval (PTTI) Applications and Planning Meeting, Vienna VA, USA*, pages 487–509, 1990.

[89] D. M. Harber, H. J. Lewandowski, J. M. McGuirk, and E. A. Cornell. Effect of cold collisions on spin coherence and resonance shifts in a magnetically trapped ultracold gas. *Phys. Rev. A*, 66:053616, 2002.

[90] M. Naraschewksi and R.J. Glauber. Spatial coherence and density correlations of trapped bose gases. *Phys. Rev. A*, 59:4595–4607, 1999.

[91] S. Blatt, J. W. Thomsen, G. K. Campbell, A. D. Ludlow, M. D. Swallows, M. J. Martin, M. M. Boyd, and J. Ye. Rabi spectroscopy and excitation inhomogeneity in a one-dimensional optical lattice clock. *Phys. Rev. A*, 80:052703, 2009.

[92] Martin W. Zwierlein, Zoran Hadzibabic, Subhadeep Gupta, and Wolfgang Ketterle. Spectroscopic insensitivity to cold collisions in a two-state mixture of fermions. *Phys. Rev. Lett.*, 91:250404, 2003.

[93] P. Lemonde, G. Santarelli, Ph. Laurent, F. Pereira Dos Santos, A. Clairon, and Ch. Salomon. The sensitivity function: A new tool for the evaluation of frequency shifts in atomic spectroscopy. In *Proceedings of the 1998 IEEE International Frequency Control Symposium*, pages 110–115, Piscataway, 1998. IEEE.

[94] Y. N. Martinez de Escobar, P. G. Mickelson, P. Pellegrini, S. B. Nagel, A. Traverso, M. Yan, R. Côté, and T. C. Killian. Two-photon photoassociative spectroscopy of ultracold ^{88}Sr. *Phys. Rev. A*, 78:062708, 2008.

[95] Gretchen K. Campbell, Andrew D. Ludlow, Sebastian Blatt, Jan W. Thomsen, Michael J. Martin, Marcio H. G. de Miranda, Tanya Zelevinsky, Martin M. Boyd, Jun Ye, Scott A. Diddams, Thomas P. Heavner, Thomas E. Parker, and Steven R. Jefferts. The absolute frequency of the ^{87}Sr optical clock transition. *Metrologia*, 45:539–548, 2008.

[96] Tomoya Akatsuka, Masao Takamoto, and Hidetoshi Katori. Three-dimensional optical lattice clock with bosonic ^{88}Sr atoms. *Phys. Rev. A*, 81:023402, 2010.

[97] A. V. Gorshkov, A. M. Rey, A. J. Daley, M. M. Boyd, J. Ye, P. Zoller, and M. D. Lukin. Alkaline-earth atoms as few-qubit quantum registers. *Phys. Rev. Lett.*, 102:110503–1–4, 2009.

[98] Sergey G. Porsev, Andrei Derevianko, and E. N. Fortson. Possibility of an optical clock using the $6\,^{1}S_0 \rightarrow 6\,^{3}P_0$ transition in ^{171,173}Yb atoms held in an optical lattice. *Phys. Rev. A*, 69(2):021403, 2004.

[99] C. W. Hoyt, Z. W. Barber, C. W. Oates, T. M. Fortier, S. A. Diddams, and L. Hollberg. Observation and absolute frequency measurements of the $^{1}S_0$-$^{3}P_0$ optical clock transition in neutral ytterbium. *Phys. Rev. Lett.*, 95:083003–1–4, 2005.

[100] H. Hachisu, K. Miyagishi, S.G. Porsev, A. Derevianko, V. D. Ovsiannikov, V. G. Pal'chikov, M. Takamoto, and H. Katori. Trapping of neutral mercury atoms and prospects for optical lattice clocks. *Phys. Rev. Lett.*, 100:053001–1–4, 2007.

[101] C. Mandache, M. Petersen, D.V. Magalhaes, O. Acef, A. Clairon, and S. Bize. Towards an optical lattice clock based on neutral mercury. *Romanian Reports in Physics*, 60:581–592, 2008.

[102] M. Petersen, R. Chicireanu, S. T. Dawkins, D. V. Magalhaes, C. Mandache, Y. Le Coq, A. Clairon, and S. Bize. Doppler-free spectroscopy of the $^1S_0 \rightarrow$ $^3P_0$ optical clock transition in laser-cooled fermionic isotopes of neutral mercury. *Phys. Rev. Lett.*, 101:183004, 2008.

Acknowledgments

Curriculum Vitae

Personal information

Date of birth   : 23 April 1978

Nationality   : Indian

Gender   : Male

Marital status : Married

Education

Jun 1982 - May 1997	All India Secondary School Examination, Central Board of Secondary Education, India.
Jul 1998 - May 2001	Bachelor's degree in Physics, Bharathidasan University, Tamil Nadu, India.
Aug 2001 - Jun 2003	Master's degree in Physics, Indian Institute of Technology Madras, Chennai, India.
Jul 2003 - Jul 2004	Physics tutor, Tutors Worlwide Pvt. Ltd, India.
Jul 2004 - Jun 2005	Scientific assistant, Raman Research Institute, India.
Jul 2005 - Jul 2006	Internship, Physikalisch-Technische Bundesanstalt, Braunschweig, Germany.
Jul 2006 - May 2010	Ph.D in Physics, Physikalisch-Technische Bundesanstalt, Braunschweig, Germany.